Modelling and control of PEM fuel cells

María Laura Sarmiento Carnevali

UNIVERSITAT POLITÈCNICA DE CATALUNYA

Programa de Doctorat:

AUTOMÀTICA, ROBÒTICA I VISIÓ

Tesi Doctoral

MODELLING AND CONTROL OF PEM FUEL CELLS

María Laura Sarmiento Carnevali

Directors: Dr. Carles Batlle-Arnau i Dra. Maria Serra-Prat

June 2017

To Rafael, Reina, Lorena and Milagros...
and Chris, who showed up just in time...

Abstract

In recent years, the PEM fuel cell technology has been incorporated to the R&D plans of many key companies in the automotive, stationary power and portable electronics sectors. However, despite current developments, the technology is not mature enough to be significantly introduced into the energy market. Performance, durability and cost are the key challenges.

The performance and durability of PEM fuel cells significantly depend on variations in the concentrations of hydrogen and oxygen in the gas channels, water activity in the catalyst layers and other backing layers, water content in the polymer electrolyte membrane, as well as temperature, among other variables. Such variables exhibit internal spatial dependence in the direction of the fuel and air streams of the anode and cathode. Highly non-uniform spatial distributions in PEM fuel cells result in local over-heating, cell flooding, accelerated ageing, and lower power output than expected.

Despite the importance of spatial variations of certain variables in PEM fuel cells, not many works available in the literature target the control of spatial profiles. Most control-oriented designs use lumped-parameter models because of their simplicity and convenience for controller performance. In contrast, this Doctoral Thesis targets the distributed parameter modelling and control of PEM fuel cells.

In the modelling part, the research addresses the detailed development of a non-linear distributed parameter model of a single PEM fuel cell, which incorporates the effects of spatial variations of variables that are relevant to its proper performance. The model is first used to analyse important cell internal spatial profiles, and it is later simplified in order to decrease its computational complexity and make it suitable for control purposes. In this task, two different model order reduction techniques are applied and compared.

The purpose of the control part is to tackle water management and supply of reactants, which are two major PEM fuel cell operation challenges with important degradation consequences. In this part of the Thesis, two decentralised control strategies based on distributed parameter model predictive controllers are designed, implemented and analysed via simulation environment. State observers are also designed to estimate internal unmeasurable spatial profiles necessary for the control action.

The aim of the first strategy is to monitor and control observed water activity spatial profiles on both sides of the membrane to appropriate levels. These target values are

carefully chosen to combine proper membrane, catalyst layer and gas diffusion layer humidification, whilst the rate of accumulation of excess liquid water is reduced. The key objective of this approach is to decrease the frequency of water removal actions that cause disruption in the power supplied by the cell, increased parasitic losses and reduction of cell efficiency.

The second strategy is a variation of the previous water activity control strategy, which includes the control of spatial distribution of gases in the fuel and air channels. This integrated solution aims to avoid starvation of reactants by controlling corresponding concentration spatial profiles. This approach is intended to prevent PEM fuel cell degradation due to corrosion mechanisms, and thermal stress caused by the consequences of reactant starvation.

The results show increased fuel cell performance considering the spatial control approaches proposed in this Thesis, in comparison to non-spatial control strategies. Moreover, the decentralised feature of the control scheme, combined with the use of order-reduced models within the model predictive controllers, has important impact on the overall control performance.

Key words: PEM fuel cells, distributed parameter modelling and simulation, model-based control, decentralised control, model predictive control, observers, water management, reactant starvation, performance enhancement

Resumen

A pesar de los avances actuales, la tecnología de celdas de hidrógeno tipo PEM no está suficientemente preparada para ser ampliamente introducida en el mercado energético. Rendimiento, durabilidad y costo son los mayores retos.

El rendimiento y la durabilidad de las celdas dependen significativamente de las variaciones en las concentraciones de hidrógeno y oxígeno en los canales de alimentación de gases, la humedad relativa en las capas catalizadoras, el contenido de agua de la membrana polimérica, así como la temperatura, entre otras variables. Dichas variables presentan dependencia espacial interna en la dirección del flujo de gases del ánodo y del cátodo. Distribuciones espaciales altamente no uniformes en algunas variables de la celda resultan en sobrecalentamiento local, inundación, degradación acelerada y menor potencia de la requerida.

Muy pocos trabajos disponibles en la literatura se ocupan del control de perfiles espaciales. La mayoría de los diseños orientados a control usan modelos de parámetros concentrados que ignoran la dependencia espacial de variables internas de la celda, debido a la complejidad que añaden al funcionamiento de controladores. En contraste, esta Tesis Doctoral trata la modelización y control de parámetros distribuidos en las celdas de hidrógeno tipo PEM.

En la parte de modelización, esta tesis presenta el desarrollo detallado de un modelo no lineal de parámetros distribuidos para una sola celda, el cual incorpora las variaciones espaciales de todas las variables que son relevantes para su correcto funcionamiento. El modelo se usa primero para analizar importantes perfiles espaciales internos, y luego se simplifica para reducir su complejidad computacional y adecuarlo a propósitos de control. En esta tarea se usan y se comparan dos técnicas de reducción de orden de modelos.

El propósito de la parte de control es abordar la gestión de agua y el suministro de reactantes, que son dos grandes retos en el funcionamiento de las celdas con importantes consecuencias para su vida útil. En esta parte de la tesis, dos estrategias de control descentralizadas, basadas en controladores predictivos de modelos de referencia con parámetros distribuidos, son diseñadas, implementadas y analizadas en un entorno de simulación. Estas tareas incluyen también el diseño de observadores de estado que estiman los perfiles espaciales internos necesarios para la acción de control.

El objetivo de la primera estrategia es monitorear y controlar perfiles espaciales ob-

servados de la humedad relativa en las capas catalizadoras para mantenerlos en niveles apropiados. Estos niveles son escogidos cuidadosamente para combinar la correcta humidificación de la membrana y las capas catalizadoras, reduciendo la velocidad de acumulación de agua líquida. El objetivo clave de este enfoque es disminuir la frecuencia de las acciones de remoción de agua dentro de la celda, ya que estas acciones causan interrupción en la potencia suministrada, aumento de las cargas parasitarias y disminución de la eficiencia.

La segunda estrategia es una variación de la estrategia anterior que considera adicionalmente el control de la distribución espacial de los gases en los canales del ánodo y cátodo. Esta solución integrada tiene como objetivo evitar la ausencia local de reactantes mediante el control de perfiles espaciales de concentración de gases. Este enfoque pretende prevenir la degradación de las celdas debido a mecanismos de corrosión.

Los resultados muestran un mayor rendimiento de la celda considerando los enfoques de control de perfiles espaciales propuestos en esta tesis, en comparación con técnicas de control que ignoran dichos perfiles. Además, la característica descentralizada de los esquemas de control, combinada con el uso de modelos reducidos dentro de los controladores predictivos, tiene un impacto positivo importante en el rendimiento general del control.

Palabras clave: celdas de hidrógeno tipo PEM, modelización y simulación de parámetros distribuidos, control basado en modelo, control descentralizado, control predictivo, observadores, gestión de agua, ausencia de reactantes, mejora de rendimiento

Acknowledgements

First, I would like to thank my advisors Dr. Carles Batlle Arnau and Dr. Maria Serra Prat for their support, constant guidance and friendship. The path we have followed, as a PhD student and advisors team, has been quite challenging. The PEM fuel cell technology offers a wide variety of opportunities for research. Therefore, addressing the current issues as part of a Doctoral Thesis requires a combination of (i) identifying, understanding and delimitating key problems with high impact on different aspects of the fuel cell lifecycle, and (ii) developing solutions that are feasible, implementable and cost-effective. Therefore, I believe Maria and Carles' excellent guidance and expertise have highly contributed to the successful achievement of this task, and the results from this work open a window for technology improvement.

I would also like to thank the former head of the Fuel Cell group of the Institut de Robòtica i Informàtica Industrial (CSIC-UPC), Dr. Jordi Riera i Colomer. Jordi not only offered his guidance during the development of this work, but he also supported, along with Maria and Carles, my application for Master's Degree and Doctoral Degree grants that had a positive outcome. Jordi is, and will always be, a mentor and a friend, who made my adaptation into the catalan culture smoother and quite enjoyable.

During my PhD studies, I did a couple of things differently in comparison to other PhD students. Far into my research path, I decided to explore the PEM fuel cell industry. I was then offered a research engineer position in the rotation scheme of the British company Intelligent Energy Holdings, plc. I spent almost two years in this company, where I had the opportinuty to analyse PEM fuel cells in automotive and stationary power applications. This experience opened a new range of possibilities for the work in my thesis. For this I would like to thank Dr. Christopher Gurney, Mrs. Joanne Kane, Dr. Pratap Rama, Dr. Ashley Fly, Mr. James Irvine, Dr. Samuel Cruz-Manzo and Dr. Paul Adcock.

Thanks to Dr. Robert Griñó, Dr. Enric Fossas and Dr. Ramon Costa from the Institut d'Organització i Control (IOC-UPC) for their support and guidance. Many thanks to the Institut de Robòtica i Informàtica Industrial (CSIC-UPC), in particular to Dr. Attila Husar and Mr. Miguel Allué. Thank you, as well, to the former Departament de Matemàtica Aplicada IV (UPC), especially to Dr. Imma Massana, Dr. Ester Simó and Dr. Marisa Zaragozá. Many thanks to Dr. Vicenç Puig, Dr. Bernardo Morcego and Dr. Gabriela Cembrano for their guidance and support during my Master's Degree studies.

Finally, on a personal note, I would like to give a huge thank you to my mother, father, two sisters and especially to my husband. Their support during this long path was key to finish off the thesis work. My British husband's cups of tea early in the morning and late at night during the last days of the thesis write-up kept me awake and happy!

Overall, this Thesis has been an amazing journey. I would not do it again, of that I am sure, but I am grateful for how it changed my life. This work made me a better professional, better colleague and, in the grand scheme of things, a better person. Thank you.

María Laura Sarmiento Carnevali

Systems Engineer, MSc.

Barcelona, Catalunya, June 2017.

Table of Contents

List of Figures

List of Tables

Nomenclature

Roman letters

A	Area, m^2
C	Volumetric capacitance, C V^{-1} m^{-3}
c	Concentration, mol m^{-3}
$D_{i,k}^{eff}$	Diffusion coefficient, m^2 s^{-1}
e	Specific total energy, J Kg^{-1}
f^V	Surface enlargement factor
h	Molar enthalpy, J mol^{-1}
I	Electrical current, A
i	Current density, A m^{-2}
L	Length, m
$\dot{n}$	Molar flux density, mol m^{-2} s^{-1}
P	Electrical power, W
p	Pressure, Pa
r	Reaction rate, mol m^{-2} s^{-1}
t	Time, s
t_W	Transport number of water in the membrane
T	Temperature, K
U	Voltage, V
u	Specific internal energy, J Kg^{-1}
v	Flow velocity, m s^{-1}
x	Space coordinate, m
y	Space coordinate, m
z	Space coordinate, m

Greek letters

α	Heat transfer coefficient, W m^{-2} K^{-1}
δ	Thickness of layer in y-direction, m
κ	Electrical conductivity of the membrane, Ω^{-1} m^{-1}
λ	Heat conductivity, W K^{-1} m^{-2}
Λ	Water content
μ	Electrochemical potential, J mol^{-1}
ξ	Mole fraction
ρ	Density, Kg m^{-3}
Φ	Electrical potential, V

Superscripts

A	Anode
C	Cathode
M	Membrane
AM	Anode-membrane side
CM	Cathode-membrane side
S	MEA components

Subscripts

i	Gas species
in	Inlet flux
k	Mesh segment

Part I

Preliminaries

Chapter 1

Introduction

There is no doubt that the current energy system based on high energy density fuels extracted from fossil reserves will evolve to a new stage. There are two main reasons for this statement: (i) fossil fuel reserves are not sufficient to meet the growing global energy demand [3, 6], and (ii) the negative impact of this type of fuels is already a matter of international concern [4].

Currently, fuels like coal, oil and gas supply the global energy demand by more than 80 percent [4]. The demand has been continually rising since the 1970s and this rise is expected to continue due to the rapid world technological advance [4, 5]. If this fuel source composition number does not change an irreversible climatic damage, driven by the emission of carbon dioxide in the combustion of fossil fuels, will occur causing serious environmental effects [3]. In order to cope with both the increasing energy demand and the climatic change there is a need for efficient and carbon-free energy sources. In this future scenario, hydrogen energy and fuel cells are being considered a key element [3, 4, 47].

1.1 PEM fuel cells

Fuel cells are electrochemical (chemical to electric) devices that convert chemical energy of fuel directly into DC electricity without the intermediate combustion process. Since fuel cells produce electrical energy directly from chemical energy, they are often far more efficient than combustion engines [73, 57]. A fuel cell requires a constant supply of fuel and oxidant to keep the electrochemical reactions proceeding.

The reactants for fuel cells, normally hydrogen and oxygen, are fed into two electrodes, the anode and the cathode, separated by an electrolyte [57]. Hydrogen can be in its pure form, or it can be in a mixture with other gasses (such as CO_2, N_2, CO), or in hydrocarbons such as natural gas (CH_4), or in liquid hydrocarbons such as methanol (CH_3OH) [13]. The essential principle of the hydrogen fuel cell is electrolysis reversed, i.e. hydrogen and oxygen recombined to produce electricity [57].

There are different types of fuel cells, characterised primarily by the fuel, type of elec-

trolyte, operating temperature, the size and the application. This work is focused on low temperature Polymer Electrolyte Membrane (PEM) fuel cells, which will be introduced in detail in the following chapters. Throughout the document, *PEM fuel cell*, *fuel cell* or *cell* will have the same meaning. Extended information on other types of fuel cells can be found in [73, 13, 71]. Particularly, it is recommended to see Figure 1-9 in Chapter 1 of reference [13].

In a PEM fuel cell, the electrolyte is a thin polymeric membrane permeable to protons. The temperature of PEM cells is low, around 80°C. At this temperature, the presence of a catalyst, typically platinum, is essential to facilitate the hydrogen oxidation reaction (HOR) on the anode side of the membrane, and oxygen reduction reaction (ORR) on the cathode side of the membrane (Figure 1.1). A gas diffusion layer, typically made of carbon cloth, ensures proper gas distribution on each side of the membrane. The only fuel cell by-products are heat and water, making them ideal zero-emission power sources.
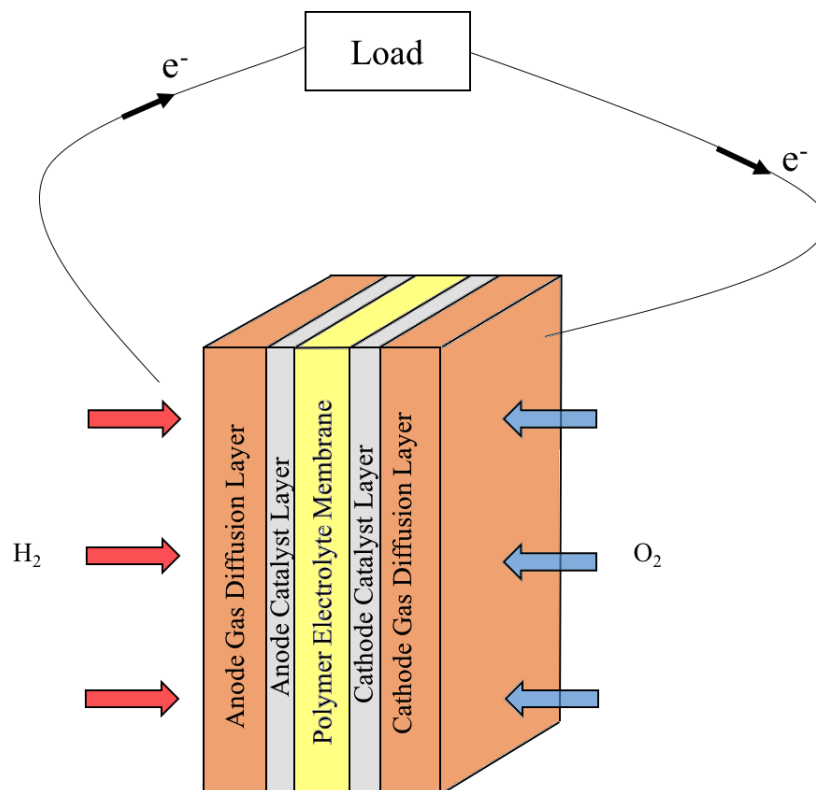
Figure 1.1: Basic anode-electrolyte-cathode construction of a fuel cell

Compared with batteries, PEM fuel cells have high energy density, low weight and low volume. This makes them one of the most promising technology for widespread use. Moreover, PEM fuel cells are not affected by spatial orientation or vibration, making them particularly adequate for motor vehicles [73]. Therefore, PEM technology is suitable for a wide range of applications including portable consumer electronics, automotive and stationary

power, raging from small power densities up to 100kW or even higher [47]. A comparative study between fuel cell electric vehicles (FCEV) and battery electric vehicles (BEV) is presented in [95]. This study offers a comprehensive review of fuel cells and batteries within the scope of an automotive application.

1.2 PEM fuel cell technology challenges

In recent years, PEM fuel cell technology has been incorporated to the R&D plans of many key companies in the automotive sector such as Damler-Chrysler, Ford, Toyota, Suzuki, Volvo, General Motors, BMW, Hyundai and Nissan [73, 51]. In the stationary power applications sector, companies like AT&T, Apple Inc., Walmart, Iberdrola and Luxfer-GTM Technologies are using PEM fuel cells as distributed back-up power sources [48, 75, 71]. The portable electronics industry is also researching on fuel cells as alternative power sources for products like mobile phones and laptops. However, despite recent developments, the technology is not mature enough to be massively introduced into the energy market. Performance, durability and cost are the key challenges for PEM fuel cells. High cost makes PEM fuel cells very difficult to sell, but it is also necessary to achieve reliable, high performance and long-lasting products.

Depending on the power demand, more than one fuel cell is necessary. For automotive and stationary applications an arrangement of fuel cells in series known as a fuel cell "stack" is used (Figure 1.2). The cost of a PEM fuel cell stack is the sum of the individual costs of the components and the cost of assembly. The total cost for a prototype average stack is currently around 1800-2000 $/kW and it is dominated by certain components like the platinum catalyst [2]. It is expected that through mass-scale production, the usage of new materials and better performance control strategies, the costs for a PEM fuel cell stack can be reduced below 100 $/kW [1, 2].

Currently, PEM fuel cells are less durable than combustion engines. Under operating conditions occurring in automotive applications like cyclic loads and frequent starts and stops, the typical lifetime of a PEM fuel cell stack is around 2000 hours. This corresponds to about 100000 km. In stationary applications, the lifetimes range from 6500 hours up to 30000 hours. The goal for stationary applications is an operating life of 40000-60000 hours or 5-8 years of operation, while in motive applications a life of 3000-5000 hours for cars and up to 20000 hours for buses is required [1, 2].

In order to overcome PEM fuel cell obstacles, many research centres are studying the introduction of new materials for components like the catalyst or the membrane, new structures and different configurations. One of the most important research efforts corresponds to the incorporation of advanced control strategies to ensure, according to the power required, a proper dynamic response and operating conditions of the fuel cell that maximises efficiency and durability.
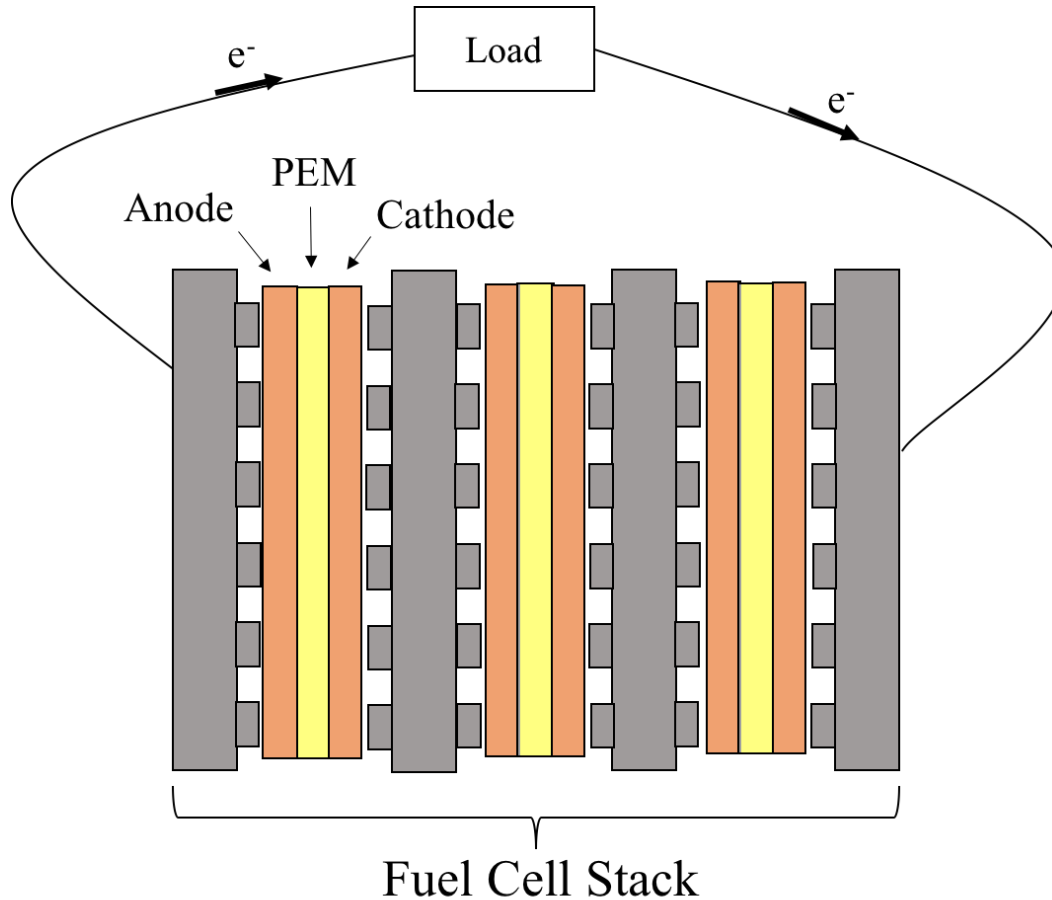
Figure 1.2: PEM fuel cell stack layout

Responding to changing demands of power with high efficiency and reliability requires to properly resolve the temperature control, hydrogen stoichiometry control, oxygen stoichiometry control, water management and many other issues faced by PEM fuel cells. Chapter 3 presents a detailed description of challenges in this technology.

Furthermore, in medium and large systems, fuel cells are accompanied by components to condition the electrical power generated, and usually there is some type of energy storage, which results in hybrid generation systems. In these systems, the control of power flows plays a key role in optimising the process [93].

It is also necessary to tackle external challenges that reduce the life of PEM fuel cells, such as temperature variations that occur outside the range recommended by manufacturers (extreme thermal cycles). These thermal cycles, caused by cold starts or high power demands, abruptly affect the characteristics of strength, conductivity and waterproofing of the membranes. Impurities in the air and fuel streams of the anode and cathode have a major impact on cell durability. Some of the most important degradation mechanisms will be described in the following chapters.

1.3   Spatial variations of PEM fuel cell variables

Fuel cell behaviour has been analysed through experimental testing and first principles or empirical modelling and simulations [30, 42, 26, 101, 52, 36]. In some cases it is almost impossible to measure some of the internal profiles of certain variables inside PEM fuel cells, making modelling and simulation along with observers [61, 25] suitable tools for PEM fuel cell online monitoring. There are important techniques like electrochemical impedance spectroscopy (EIS) or neutron imaging that can be used to understand internal behaviour of some components in a fuel cell research test rig [110, 62, 23]. However, online implementation of those techniques increases the level of complexity and cost of the fuel cell control system. Currently, these techniques are more typically used for diagnosis at a development level.

Several authors have demonstrated that variations in the concentrations of hydrogen, oxygen and water, as well as temperature and many other variables, have significant effects on the performance and durability of PEM fuel cells. All of these variables exhibit internal spatial dependence in the direction of the fuel and oxygen streams of the anode and cathode. Highly non-uniform spatial distributions in PEM fuel cells result in local over-heating, cell flooding, accelerated ageing, and lower power output than expected [30, 42, 26, 101, 52, 36]. A distributed parameter model is necessary to model and simulate these spatial variations.

First principles models are built-up from ordinary differential equations (lumped parameter models) or partial differential equations and corresponding algebraic conditions (distributed parameter models) that allow the detailed study of fundamental phenomena. A distributed parameter system is one in which all dependent variables are functions of time and one or more spatial variables. In this case, solving partial differential equations (PDEs) is required.

In order to perform numerical simulations it is necessary to discretise the set of PDE and corresponding algebraic constraints. However, the number of ordinary differential equations (ODEs) and algebraic relations obtained from the discretisation of a distributed parameter model is very high; this not only slows down the numerical simulations, but also makes the application impractical for most control strategies. Therefore, it is necessary to apply model order reduction (MOR) techniques [88].

In general, MOR techniques attempt to preserve the relationship between certain input and output variables, as determined from the control objectives. Once these input-output variables have been set, it is possible to use efficient and robust well known linear reduction methods [88]. These techniques have also been extended to the order reduction of nonlinear systems and systems with algebraic constraints (DAEs) [88]. Obtaining accurate reduced models of PEM fuel cells facilitates the development of efficient controllers for them.

1.4   Thesis objectives and content outline

Despite several authors have demonstrated the importance of spatial variations of certain variables in PEM fuel cells, not many works available in the literature target the control of spatial profiles. Most control-oriented designs use lumped-parameter models because of their simplicity and convenience for controller performance [97, 7, 11, 37, 112, 78, 104, 100]. Therefore, this thesis targets the distributed parameter modelling and control of PEM fuel cells. The main objectives of the work are:

(1) To develop a non-linear distributed parameter model that incorporates the effects of spatial variations of variables that are relevant to the proper performance of PEM fuel cells.

(2) To simplify the distributed parameter model in order to make it suitable for control purposes and efficient numerical simulations. In this task, model order reduction techniques will be applied.

(3) To design distributed parameter model-based controllers and control strategies, in order to tackle some of the most important PEM fuel cell challenges.

The thesis is organised as follows:

- **Chapter 2** presents a detailed review of the theory of PEM fuel cells. Fuel cell structure, functionality, electrochemistry, ideal and actual performance and water processes are analysed in this chapter.

- **Chapter 3** covers a detailed review of the current challenges of PEM fuel cell technology, regarding the optimal operation of the cell and most important reversible and irreversible degradation mechanisms.

- **Chapter 4** delimitates the problem of interest within the PEM fuel cell challenges analysed in Chapter 3, and defines the modelling and control objectives for this thesis.

- **Chapter 5** presents the non-linear distributed parameter PEM fuel cell model developed for this thesis. This chapter includes first principles and empirical equations of the phenomena occurring within the PEM fuel cell model, corresponding discretisation of the equations and the description of considered fuel cell components. In addition, model validation approaches are explained in this chapter. Literature review on the variety of PEM fuel cell models is covered in the first sections.

- **Chapter 6** covers a series of analyses of the variation of spatial profiles for certain variables in the cell using the model developed in Chapter 5. The variables of interest are associated to major challenges in water transport management and starvation of reactants. The definition of control targets is part of the conclusions of this chapter.

- **Chapter 7** presents the model order reduction of the distributed parameter PEM fuel cell model developed in chapter 5, according to previously identified control targets. In this chapter, control-oriented models that still consider spatial variations are derived and their accuracy analysed, in order to be control reference models in Chapter 8. In addition, the theory of the different reduction techniques used in this work is explained in the first sections of the chapter.

- **Chapter 8** covers the development of different model-based control approaches designed to enhance fuel cell performance and improve durability, considering spatial variation control targets. These targets are mainly related to cell water management, maintaining other important objectives such as reactants feed control and optimal temperature. Model predictive control is introduced in this chapter as the chosen model-based control technique. The dynamics and performance of the designed controllers are evaluated and analysed by computer simulations. State observers are also introduced in this chapter. Literature review on PEM fuel cell control approaches is covered in the first sections.

- **Chapter 9** finally presents general concluding remarks and the scope of opportunities for future research.

1.5   Thesis publications

The contributions resulting from this thesis are:

Journal papers

- M.L. Sarmiento-Carnevali, M. Serra, C. Batlle, Decentralised distributed parameter model predictive control of water activity for performance and durability enhancement of a PEM fuel cell, submitted to the Journal of Power Sources, May 2017.

- M.L. Sarmiento-Carnevali, M. Serra, C. Batlle, Distributed parameter model simulation tool for PEM fuel cells, International Journal of Hydrogen Energy 39, 4044-4052 (2014).

National and international conference papers

- M.L. Sarmiento-Carnevali, A. Fly, C. Batlle, M. Serra, R.H. Thring, Model predictive control for water balance in an evaporatively cooled PEM fuel cell system, presented at 21st World Hydrogen Energy Conference (WHEC 2016), June 13-16th, 2016, Zaragoza, Spain.

- M.L. Sarmiento-Carnevali, C. Batlle, M. Serra, I. Massana, Distributed parameter PEMFC model order reduction, Libro de Comunicaciones del Congreso Iberoamericano de Hidrogeno y Pilas de Combustible (Iberconappice 2014), October 15-17th, 2014, Bellaterra, Catalonia.

- M.L. Sarmiento-Carnevali, C. Batlle, I. Massana, M. Serra, Order reduction of a distributed parameter PEM fuel cell anode gas channel model, Proceedings of the European Hydrogen Energy Conference (EHEC 2014), March 12-14th, 2014, Seville, Spain.

- M.L. Sarmiento-Carnevali, M. Serra, C. Batlle, Analysis of conventionally controlled PEMFC based on a distributed parameter model, IV Iberian Symposium on Hydrogen, Fuel Cells and Advanced Batteries (HYCELTEC 2013), June 26-28th, 2013, Estoril, Portugal.

- M.L. Sarmiento-Carnevali, M. Serra, C. Batlle, Distributed parameter model simulation tool for PEM fuel cells, presented at V Congreso Nacional de Pilas de Combustible (CONAPPICE 2012), November 21-23th, 2012, Madrid, Spain.

Chapter 2

PEM fuel cells basics

2.1   Fuel cell functionality

In a Polymer electrolyte membrane (PEM) fuel cell, the anode and the cathode are separated by a hydrophilc polymer functionalised by acidic side chains known as proton exchange membrane, which acts as the electrolyte. The PEM has some unique capabilities: it conducts protons and is impermeable to gases [57]. Figure 2.1 illustrates the different components and the operation of a PEM fuel cell.

Due to catalyst materials, partial electrochemical reactions take place within each electrode. Electrons are released at the anode and consumed at the cathode. The electrons produced at the anode flow through an external circuit to the cathode. The partial reactions also produce H^+ ions (or protons) that pass through the electrolyte, which should ideally block transport of the other species, specially electrons so they actually go round the external circuit [13]. Electrochemical reactions involve both a transfer of electrical charge and a change in Gibbs free energy.

2.2   Fuel cell structure

As seen in Figure 2.1, on both sides of the membrane of the PEM fuel cell there are two porous electrically conductive electrodes made usually out of carbon cloth or carbon fiber paper [76]. At the interfaces of the electrodes and the polymer membrane there is a layer with catalyst particles called the catalyst layer (CL). This layer is made of platinum particles supported on carbon [13].

The electrodes must be porous so the reactant gases, fed from the back, reach the catalyst layers where the electrochemical reactions take place (catalyst surface). Reactants diffuse from gas channels to catalyst layers through the so-called gas diffusion layers (GDLs). The multilayer assembly formed by the gas diffusion layers, the catalyst layers (electrodes surface) and the polymer membrane is called the membrane electrode assembly (MEA) [13]. The MEA is between the bipolar plates (BPPs), which collect and conduct electrical
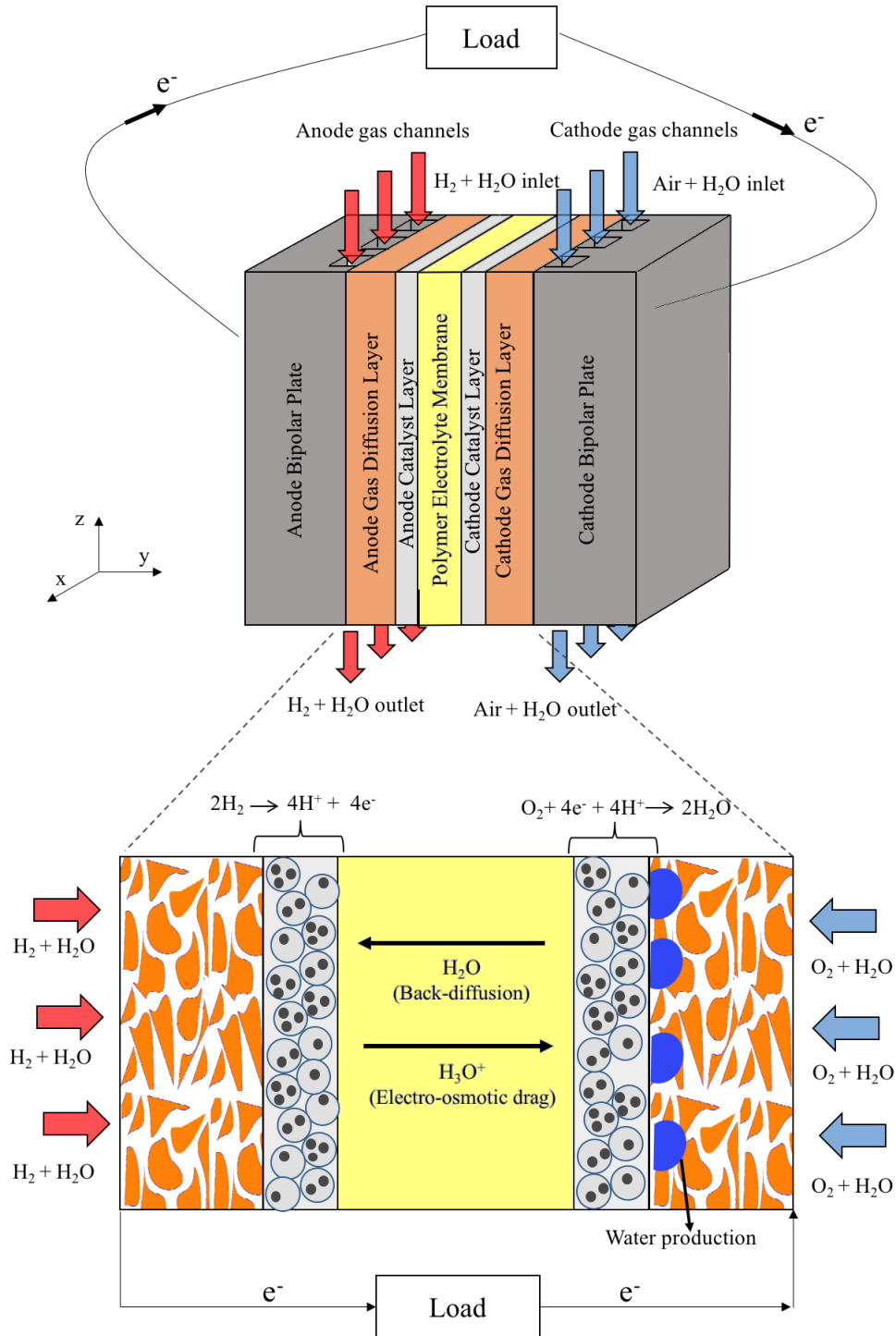
Figure 2.1: PEM fuel cell structure and operation scheme

current, and separate the gases in adjacent cells for a multicell configuration. In addition, the bipolar plates provide pathways for flow of reactant gases, also known as gas channels (GCs) or flow fields, as well as channels for liquid coolant. These plates are called bipolar

plates because they connect the cathode of one cell to the anode of the adjacent cell, and they also provide the cell structural rigidity [57].

2.3   Electrochemical reactions

The electrochemical reactions take place simultaneously at the catalyst layers on both sides of the membrane. In general, an electrochemical reaction involves either oxidation or reduction of the species. In the hydrogen/oxygen fuel cell the anode reaction is oxidation of hydrogen (HOR). Hydrogen flows into the PEM fuel cell and diffuses through the gas diffusion layer to the catalyst layer, where catalyst particles facilitate fuel oxidation. Hydrogen gas ionises, releasing electrons and creating H^+ ions (or protons) [20]:

$$2H_2 \rightarrow 4H^+ + 4e^- \tag{2.1}$$

Protons hitch onto water molecules inside a sufficiently hydrated membrane forming hydronium complexes H_3O^+ that move through the membrane from the anode to the cathode. This process is called electro-osmotic drag and it will be explained in more detail in Chapter 5.

Electrons reach the cathode side over the bipolar plates and over an external circuit (load) where power can be drawn. On the cathode side, oxygen diffuses to the catalyst layer and is electrochemically combined with protons and electrons to form water (oxygen reduction - ORR) [20]:

$$O_2 + 4e^- + 4H^+ \rightarrow 2H_2O \tag{2.2}$$

It should be noticed that electrodes must also be porous so that water leaves the reaction site. The excess flow of oxygen pushes water out of the cell. The net result of these simultaneous reactions is current of electrons through an external circuit (direct electrical current) (Figure 2.1). As will be shown subsequently, the resulting voltage of a single cell is on the order of 1V. This means more cells are needed in series to generate practical voltages depending on the application. A collection of fuel cells in series is known as a "stack". Figure 2.2 shows an example of a stack with 3 cells.

2.4   Ideal performance

This section describes the thermodynamics that characterise ideal performance of a PEM fuel cell. Once the ideal performance is determined, voltage losses will be calculated and deducted from ideal performance in Section 2.5.

The ideal performance of a PEM fuel cell depends on the electrochemical reactions that occur with hydrogen and oxygen. The overall reaction of a PEM fuel cell is the same as the
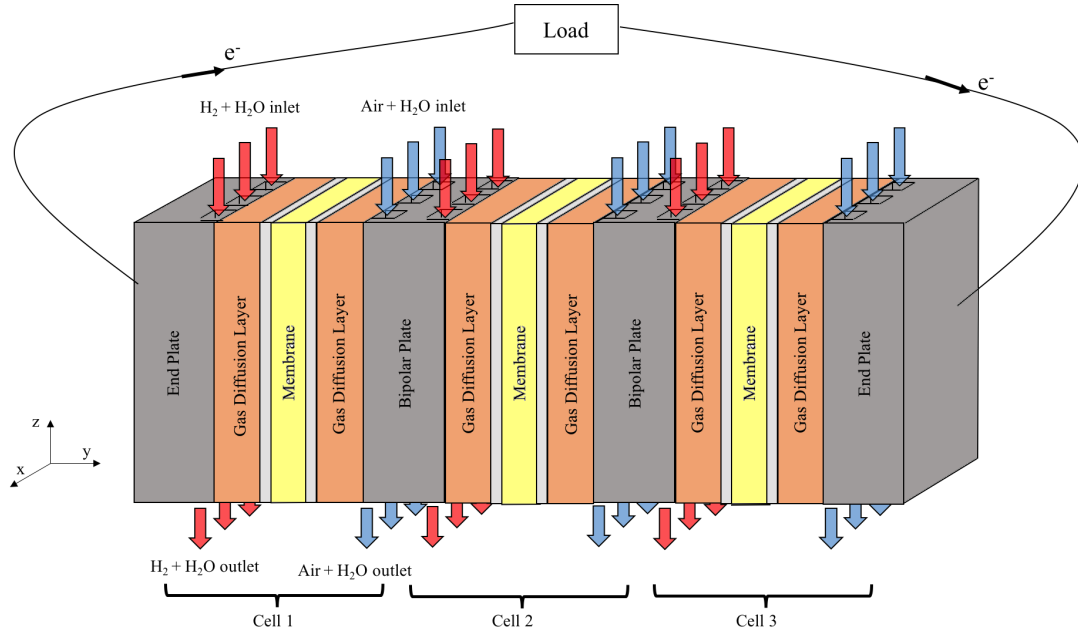
Figure 2.2: PEM fuel cell stack layout

reaction of hydrogen combustion, which is an exothermic process (releases energy) [13].

$$H_2 + \frac{1}{2}O_2 \rightarrow H_2O + heat \tag{2.3}$$

In order to determine the amount of useful (thermal) energy that can be extracted from hydrogen, the enthalpy of hydrogen combustion reaction is calculated [73]. This value is also called the hydrogen heating value, which is the amount of heat that may be generated by a complete combustion of 1 mol of hydrogen. The enthalpy of a chemical reaction is the difference between the heats of formation of products and reactants. For equation 2.3, this is:

$$\Delta H = (h_f)_{H2O} - (h_f)_{H2} - \frac{1}{2}(h_f)_{O2} \tag{2.4}$$

The heat of formation of liquid water is -286 kJ/mol at 298.15 K (25°C) and heat of formation of elements is by definition equal to zero [13]. At 25°C and atmospheric pressure water is in liquid form (assuming there is no excess of oxygen or additional gases such as nitrogen). It is necessary to point out that there is a hydrogen's higher heating value and lower heating value, and the difference relies on whether hydrogen is reacted with an excess of oxygen (or nitrogen present) or not, and therefore whether the product water forms as vapour or liquid. For the purpose of this section, hydrogen higher heating value has been considered. This is:

$$\Delta H = (h_f)_{\text{H2O}} - (h_f)_{\text{H2}} - \frac{1}{2}(h_f)_{\text{O2}} = -286\text{kJ/mol} - 0 - 0 = -286\text{kJ/mol} \quad (2.5)$$

The negative sign means energy is being released. Thus, equation (2.3) can be rewritten as:

$$\text{H}_2 + \frac{1}{2}\text{O}_2 \rightarrow \text{H}_2\text{O(l)} + 286\text{kJ/mol} \quad (2.6)$$
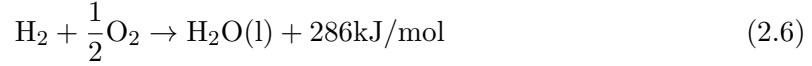
Hydrogen heating value is used as a measure of energy input in a fuel cell, although there is no combustion in it. This is the maximum amount of thermal energy than can be extracted from hydrogen. However, because of entropy produced in every chemical reaction, a portion of hydrogen's heating value cannot be converted into useful work. It is the Gibbs free energy, ΔG, of the reaction that is the available energy at the temperature of the conversion. Gibbs free energy is given by the following equation:

$$\Delta G = \Delta H - T\Delta S \quad (2.7)$$

The creation of entropy generates irreversible losses in energy conversion, ΔS, which is the difference between entropies of products and reactants, as follows:

$$\Delta S = (s_f)_{\text{H2O}} - (s_f)_{\text{H2}} - \frac{1}{2}(s_f)_{\text{O2}} \quad (2.8)$$

The values of enthalpies and entropies for fuel cell reactants and products are shown in Appendix A. These values are valid at 25°C and ambient pressure. Taking into account irreversible losses, at 25°C, out of the 286.02 kJ/mol of maximum amount of energy, 237.34 kJ/mol can be converted into electrical energy and the remaining 48.68 kJ/mol is converted into heat.

2.4.1 Theoretical fuel cell potential

As stated in equation (2.7), the maximum electrical work (W_{el}) obtainable in a fuel cell operating at constant temperature and pressure is given by the change in Gibbs free energy (ΔG) of the electrochemical reaction. Electrical work is:

$$W_{\text{el}} = -n\text{FE} \quad (2.9)$$

where n is the number of electrons participating in the reaction, F is Faraday's constant (96,485 Coulombs/electron-mol), and E is the ideal potential of the cell. Therefore:

$$W_{\text{el}} = -(\Delta G) \quad (2.10)$$

The theoretical potential of fuel cells is then:

$$E = \frac{-\Delta G}{nF} = \frac{237.340 \text{ J mol}^{-1}}{2\text{x}96,485 \text{ Coulombs/electron-mol}} = 1.23 \text{Volts} \tag{2.11}$$

This means that at 25°C, theoretical hydrogen/oxygen fuel cell potential is 1.23 Volts [13].

2.4.2   Theoretical fuel cell efficiency

The thermal efficiency of an energy conversion device is defined as the amount of useful energy released when a fuel is reacted with an oxidant, relative to the change in stored chemical energy. In the case of a fuel cell, the useful energy output is the electrical energy produced (ΔG), and the change in stored chemical energy is hydrogen's heating value (ΔH) [13]. The maximum possible (theoretical) efficiency in a fuel cell is [73]:

$$\eta = \frac{\Delta G}{\Delta H} = \frac{237.34}{286.02} = 83\% \tag{2.12}$$

2.4.3   Effect of operating conditions

All the previous equations were valid at 25°C and atmospheric pressure. However, a fuel cell may operate, typically, from atmospheric up to 6-7 bar and higher than 25°C. The ideal performance of a fuel cell is defined by its Nernst potential, which is a function of temperature and pressure [13]:

$$E_{T,P} = - \left(\frac{\Delta H}{nF} - \frac{T\Delta S}{nF} \right) + \frac{RT}{nF} ln \left[\frac{P_{H_2} P_{O_2}^{0.5}}{P_{H2O}} \right] \tag{2.13}$$

Ideal efficiency decreases with temperature whereas higher reactant pressures cause a higher cell potential.

2.5   Actual performance

If the electrical circuit is not closed and the fuel cell is being supplied with reactant gases, the actual cell potential is decreased from its Nernst potential. This is usually less than 1V, and it is called the open circuit voltage (OCV), which suggests that there are losses in the fuel cell even when no external current is generated. However, useful work is obtained from a fuel cell only when a reasonable current is drawn. In this case, the actual cell potential is decreased from the Nernst potential because of irreversible losses. This is because at OCV, hydrogen crossover losses are important. However, when a considerable current is drawn these losses can be neglected.

To determine actual cell performance, three main losses must be deducted from the Nernst potential. These losses, often called polarisation, overpotential, or overvoltage are: activation polarisation, ohmic polarisation and concentration polarisation.

2.5.1 Activation polarisation

This type of loss is associated with sluggish electrode kinetics. Some voltage is needed to get the electrochemical reaction going [20]. These losses happen at both anode and cathode; however, oxygen reduction requires much higher overpotential, because it is a much slower reaction than hydrogen oxidation. A simple way to express the activation losses is through the Tafel equation:

$$\Delta V_{act} = \frac{RT}{\alpha F} ln\left(\frac{i}{i_0}\right) \tag{2.14}$$

where α is the electron transfer coefficient of the reaction at the electrode (anode or cathode) and i_0 is the exchange current density, as will be seen in equation (2.18).

2.5.2 Ohmic polarisation

Ohmic losses occur because of resistance to the flow of protons in the electrolyte and resistance to the flow of electrons through the electrode materials. Because both the electrolyte and fuel cell electrodes obey Ohm's law, the ohmic losses can be expressed by the equation:

$$\Delta V_{ohm} = i\Omega \tag{2.15}$$

where i is the current flowing through the cell, and Ω is the total cell resistance, which includes electronic, ionic and contact resistance [13].

2.5.3 Concentration polarisation

As a reactant is consumed at the electrode by the electrochemical reaction, there is a loss of potential due to the inability of the surrounding material to maintain the initial concentration of the bulk fluid, thus, a concentration gradient is formed. At practical current densities, slow transport of reactants/products to/from the electrochemical reaction site is a major contributor to concentration polarisation [13]:

$$\Delta V_{conc} = \frac{RT}{nF} ln\left(\frac{i_L}{i_L - i}\right) \tag{2.16}$$

where i_L is the limiting current, which is the current density reached when reactant is consumed faster than it can reach the surface. A fuel cell cannot produce more than the limiting current because there are no reactants at the catalyst surface.

2.6 Polarisation curve

Activation and concentration losses can occur at both anode and cathode. The actual cell voltage is therefore:
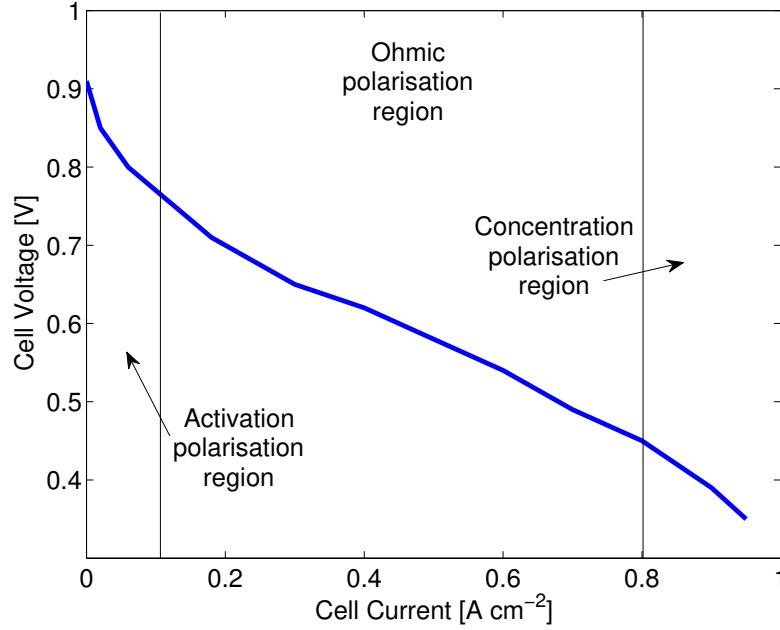
Figure 2.3: PEM fuel cell polarisation curve

$$V_{cell} = E_{T,P} - (\Delta V_{act} + \Delta V_{conc})_a - (\Delta V_{act} + \Delta V_{conc})_c - \Delta V_{ohm} \tag{2.17}$$

where E_r is the ideal performance voltage. By introducing equations (2.14), (2.15) and (2.16) into (2.17), a relationship between fuel cell potential and current density is obtained. This is the so-called fuel cell polarisation curve:

$$V_{cell} = E_{T,P} - \frac{RT}{\alpha_c F} ln \left(\frac{i}{i_{0,c}} \right) - \frac{RT}{\alpha_a F} ln \left(\frac{i}{i_{0,a}} \right) - \frac{RT}{nF} ln \left(\frac{i_{L,c}}{i_{L,c} - i} \right) - \frac{RT}{nF} ln \left(\frac{i_{L,a}}{i_{L,a} - i} \right) - i\Omega \tag{2.18}$$

Figure 2.3 shows the polarisation curve of a single PEM fuel cell with 5 cm^2 electrochemical surface area. Three regions can be identified. In the activation polarisation region voltage falls rapidly due to the activation energy barrier. In the ohmic polarisation region voltage fall is slower and approximately linear due to membrane and electrode ohmic resistance. In practice the ionic conductivity of the membrane is significantly less than the electronic conductivity of the external circuit, which means that the resistance through the membrane dominates [13]. Finally, the last section of the curve is the concentration polarisation region with voltage losses mainly due to mass transport limitations at high current densities.

2.7 Water transport processes

As illustrated in Figure 2.1, water is generated on the cathode side of the membrane as a result of the oxygen reduction reaction (ORR) and it is supplied to the cell by humidified reactants. Two modes of water transport through the membrane occur: electro-osmotic drag transport, which corresponds to water dragged from the anode to the cathode by protons in the form of hydronium complexes (H_3O^+), and back diffusion transport, which corresponds to water that travels from the cathode to the anode due to a large concentration gradient across the membrane. Details of these processes are presented in Chapter 5. In addition, a sufficient amount of water generated at the cathode must be removed from the catalyst layer by evaporation, water-vapour diffusion and capillary transport of liquid water throw the GDL into the flow channels of the flow field, and then exhausted at the outlet [80].

2.8 Balance of plant components

In order to operate, fuel cells are accompanied by the hydrogen supply system, the air supply system, the cooling system and the humidification system, as well as elements to condition the electrical power generated [13]. All the elements that support the fuel cell operations are known as the "balance of plant" (BoP). Together fuel cell/stack and the balance of plant form a "fuel cell system". Figure 2.4 shows a classic example of a fuel cell system for automotive applications.

This thesis focuses on improving the performance and lifetime of a single PEM fuel cell. The control actions to be designed in the following chapters would be executed by the different BoP components, however, specific analysis of these components is not considered, as the main target of this work is to assess the potential effect of proposed novel control actions.

2.9 Conclusions

In this chapter, theoretical aspects of the PEM fuel cell technology were presented in order to introduce the research field. Fuel cell structure, components and core functionality were described in detail. Ideal performance of a PEM fuel cell was calculated within a thermodynamics and electrochemistry framework. Actual performance of the cell was later introduced by taking into account voltage losses due to different operating aspects, resulting in the derivation of the fuel cell polarisation curve.

The following chapter covers the literature review of state-of-the-art challenges in the PEM fuel cell technology. Degradation mechanisms of the different cell components, which have major impact on cell durability, are also presented.
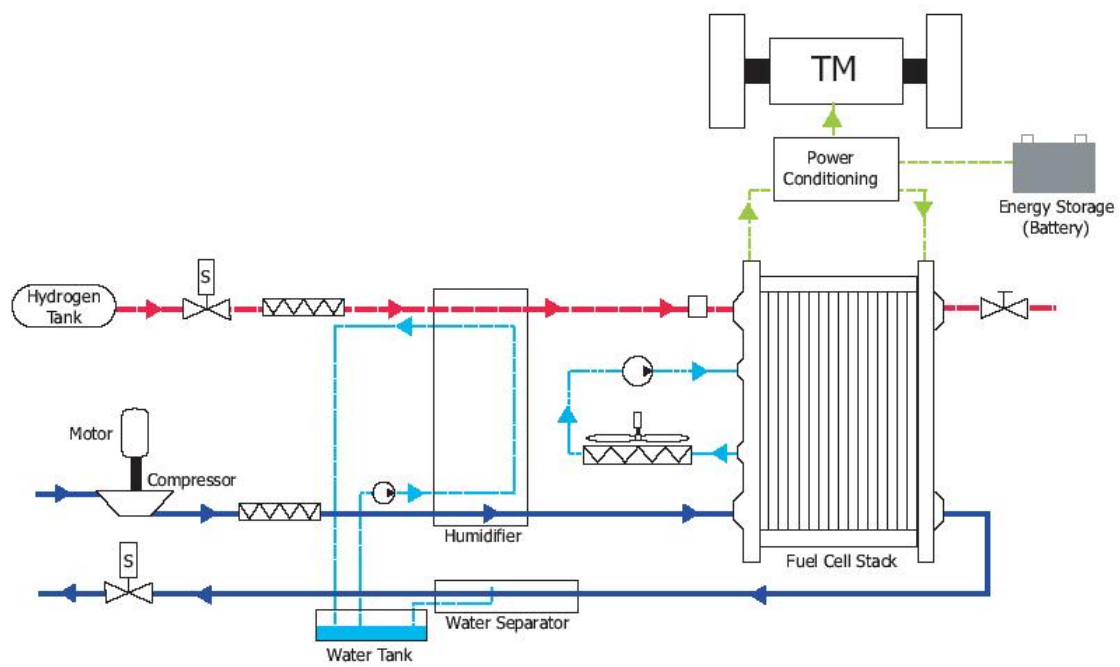
Figure 2.4: Automotive fuel cell system components [13]

Chapter 3

PEM fuel cells challenges

As stated in Chapter 1, performance, durability and cost are the most important challenges for PEM fuel cells in order to meet international benchmark efficiency targets [4], and be significantly introduced into the future energy scenario. Cost reduction efforts are active within important research fields that cover construction and assembly methods [60, 55], component materials [103] including new catalysts, novel types of membranes and electrodes, better sealing gaskets, improved fuel production, storage and transport [44], as well as overall cell efficiency; i.e, performance, reliability and durability.

Performance, meaning the power output, and durability of PEM fuel cells depend on the operating conditions and component materials. Active research on materials is also underway to increase performance by improving some operations within the cell and mitigate certain degradation mechanisms in specific components [50]. The operating environment of a fuel cell and conditions to which it might be exposed can also affect its performance and lifetime. There are several key factors affecting PEM fuel cells performance and durability.

Inadequate control strategies for the supply of reactant gases, thermal management and water management are some of the current issues affecting the performance, reliability and durability of PEM fuel cells. In addition, operating conditions like cyclic loads and frequent starts and stops considerably reduce cell lifetime. Degradation mechanisms due to contamination by impurities present in the fuel and air streams, as well as extreme thermal cycles, are also major causes of cell failure. In this chapter, a literature review of current PEM fuel cell challenges and most important degradation mechanisms is presented. In some cases, available mitigation strategies are included.

3.1   PEM fuel cell performance challenges

Operating conditions and operating strategies play an important role in a fuel cell lifecycle. The following sections describe some of these challenges in sufficient detail to understand the problems and current mitigation approaches proposed in the available literature.

3.1.1   Fuel or oxidant starvation

Poor distribution of fuel cell reactants can occur in the presence of high cell currents, liquid water, fuel impurities, ice, different flows of fuel, air and coolant resulting from imperfect manifolding or sudden changes in the power demand and overall different conditions between cell inlet and outlet. These situations may cause fuel or oxidant starvation, which refers to sub-stoichiometric reaction conditions. In a state of starvation, the performance of the fuel cell degrades and the cell voltage drops. Starvation at the anode side, i.e. hydrogen starvation, is also possible due to the presence of air inside the anode gas channel prior to the start-up of the fuel cell. Similarly, air starvation can also happen at a restart of the cell after a shutdown action and nitrogen purge.

Fuel or oxidant starvation can cause severe degradation. It has been observed that, in the case of gross fuel starvation, cell voltages can become negative, as the anode is elevated to positive potentials and the carbon is consumed given the lack of fuel. This means the anodic current will be provided by carbon corrosion to form carbon dioxide, which results in permanent damage to the anode catalyst layer. Moreover, oxygen or hydrogen starvation can result in generation of hydrogen in the cathode or oxygen in the anode [24, 114]. High anode potential, as a consequence of fuel starvation, may cause the water present in the anode to split into hydrogen and oxygen producing oxygen in the anode. Similarly during oxygen starvation the reaction at the cathode will produce hydrogen. The presence of fuel and oxidant of the wrong side of the membrane will also lead to reverse cell potential, carbon corrosion and subsequently to damaged components. Degradation mechanisms will be explained further down in this section.

In order to avoid this problem proper reactant distribution is critical. A good monitoring system controlling sensors and indicators is necessary. Such an extensive monitoring system will add considerable cost and complexity to the fuel cell and control strategy. Comprehensive reviews of research in this topic are presented in [84, 34].

3.1.2   Thermal management

Changes associated with transitions between low and high power affect the performance of the fuel cell in the short term and its durability in the long term [21]. The membrane swells when exposed to high relative humidity (RH) conditions, which is usually the case at low cell currents with low cell temperatures, and its size reduces when drying during high currents, when the cell is normally hotter and dryer. These changes of size produce material stresses that are a significant contributor to mechanical failures of the membrane. Degradation mechanisms for different fuel cell components will be mentioned further ahead in this chapter.

Thermal management is particularly important when the fuel cell is exposed to extreme temperatures, specially when the stack is operated below 0°C or above 80°C. Several studies have shown that improper thermal management, which allows the cell to reach high

temperatures (80°C), leads to an increased membrane and catalyst degradation. Higher temperature promote the occurrence of radicals and the loss of electrochemical surface area (ECSA) affecting cell durability. There are different cooling techniques for PEM fuel cells. Fly [39] reviewed the variations among liquid-cooled, air-cooled and evaporatively-cooled fuel cells. In this thesis a liquid-cooled PEM fuel cell is considered, thus thermal management is performed by coolant channels on the bipolar plates [57].

Fuel cells cycling between sub- and above zero cell temperatures for an extended period of time show strong degradation. When operating in freezing conditions, the MEA and other cell components can be delaminated. The GDL deterioration comes from the probability of freezing water within the pores. Dilaminated components cause loss of thermal and electric interfacial contact [113]. A comprehensive review of thermal management can be found in [34].

3.1.3   Water management

The operation of a PEM fuel cell is fundamentally linked to the presence of water in the cell, therefore, water management is critical and one of the most widely studied issues in PEM fuel cell technology. Proper water management requires meeting two conflicting needs: adequate membrane hydration and avoidance of water flooding in the catalyst layers, GDLs and gas flow channels in the bipolar plates.

On one hand, it is important to keep the membrane and the catalyst layer humidified for high proton conductivity. Figure 3.1 illustrates expanded sections of the materials of the catalyst layers and gas diffusion layers. As previously explained, in the presence of water, protons form hydronium complexes (H_3O^+) on the boundaries of the catalyst layer and the membrane. These complexes transport the protons from the anode catalyst layer to the cathode catalyst layer in aqueous phase [57]. Therefore, the correct humidification of the membrane is also a key aspect of cell performance [111].

On the other hand, accumulation of too much water also impacts performance and lifetime. Humidification of the reactants before entering the fuel cell is one strategy to keep the membrane fully hydrated. The challenge arises under certain operating conditions, particularly at high load cycles, when the rate of water generation is considerable, or at low temperatures and high relative humidity. In these situations, the gases inside the fuel cell become oversaturated with water vapour, and condensation occurs on the anode and cathode sides reducing fuel cell performance [31].

Water flooding

Accumulation of condensed excess water inside the cell can impede and block the reaction sites, the pores of the GDL and the gas flow channels in the bipolar plates. This phenomenon, known as "flooding", is an important limiting factor of PEM fuel cell performance and durability. Excess water blockages can instantly lead to reactant starvation and
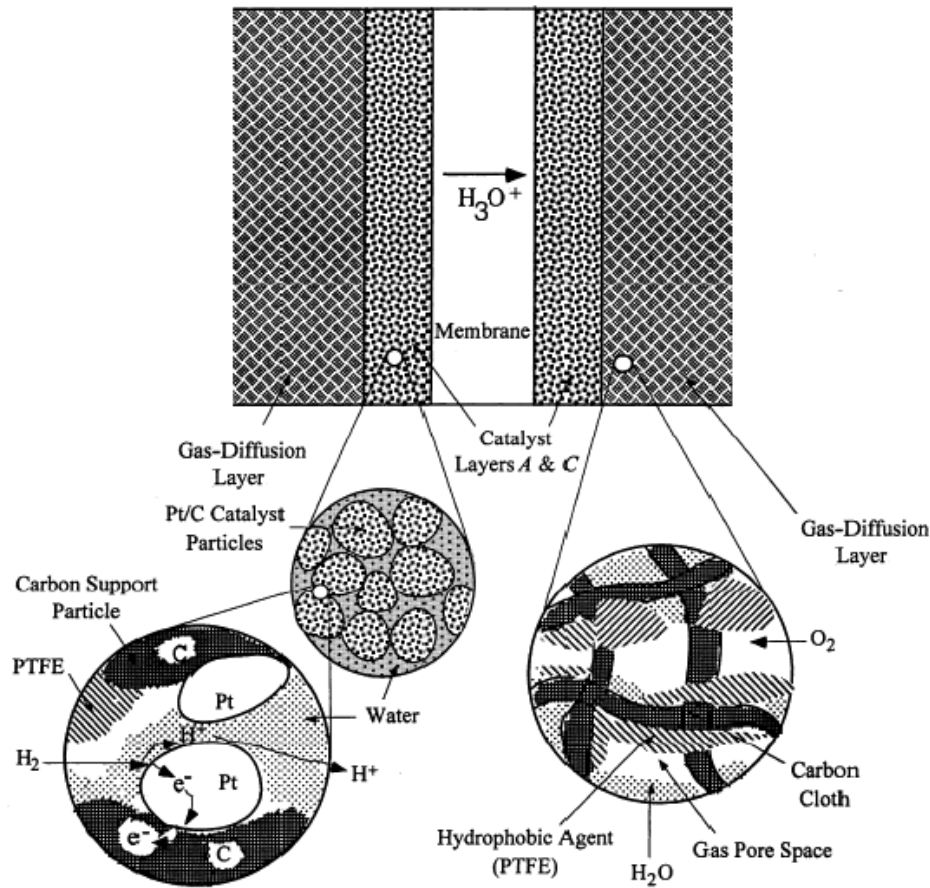
Figure 3.1: Expanded sections of the catalyst layer and gas diffusion layer [10]

immediate drop in cell potential. Long cell exposure to excess water causes degradation effects introduced in Section 3.1.1. In addition, due to the water layer on the GDL surface, its pore size may be reduced. Consequences are the dissolution and diffusion of the reactant gas into the liquid water. Moreover, the gas may also be forced to flow through alternative channels, which results in a partial pressure decrease across components [84].

The amount and effects of flooding depend on the interaction of the operating conditions and the MEA component properties. Flooding is generally linked to high current density operation that results in water production rate that is higher than the removal rate. However, this phenomenon can also occur at low current densities under certain operating conditions, such as low gas temperatures and low gas flow rates, where faster saturation of the gas phase by water-vapor can occur [31]. Therefore, proper water management is important and consists of maintaining the balance among: (i) the water carried inside and outside the cell by inlet and outlet gases, (ii) the water generated in the cathode side of the membrane by the electrochemical reaction, (iii) the water transported by electro-osmosis

and back diffusion through the membrane, (iv) the temperature of the fuel cell and (v) the gas pressure [16].

Cathode flooding Flooding can occur at both anode and cathode sides of the membrane, but it is typically seen at the cathode [84, 92]. Three mechanisms contribute to the flooding of the cathode, especially at its GDL and CL:

  (i) water generated in the cathode side of the membrane by the electrochemical reaction (ORR),

 (ii) electro-osmotic drag (the rate of transported water depends on the humidification level of the membrane and increases with increasing current density),

(iii) saturated or over-humidified reactant gases.

Anode flooding Since the cathode is the water generating electrode, it takes much longer to accumulate water at the anode. Flooding on the anode side of the membrane is less frequent, but it can also have serious consequences on the fuel cell operation, namely performance and degradation. Moreover, due to low fuel flow rates, liquid water is more difficult to remove from the anode. Some authors have reported that anode flooding is more likely to happen at low current densities (0.2 A cm^{-2}) due to a lower electro-osmotic force [43, 74], specially at low reactant flow rates and low temperatures. These works reported important spatial variations in water activity along the channels. At the inlet of the anode, where the proton flux is high, a strong electro-osmotic force drags the water molecules from the anode to the cathode resulting in low water content. At the exit, in contrast, current density is lower and hydrogen concentration has decreased due to consumption by the electrochemical reaction. Therefore, the partial pressure of water is higher and closer to total anode pressure resulting in higher water activity. The importance of spatial variations analysis in water management has been demonstrated in several works [30, 42, 26, 101, 52, 36]. This topic will be widely discussed in the next chapter. Anode flooding can also be produced by:

  (i) water back-diffusion from the cathode combined with low fuel gas humidification, specially under low current densities (in this case the water back-diffusion surpasses the electro-osmotic effect) [65],

 (ii) electro-osmotic drag of water by protons movement from anode to cathode (the rate of transported water depends on the humidification level of the membrane and increases with increasing current density [43, 74]),

(iii) saturated or over-humidified reactant gases, specially at low temperatures (lower evaporation) [43, 65]).

Different authors have proposed diagnosis and mitigation strategies for water management. He et al. [45] correlated partial pressure directly to the flooding level and considered it to be a good indicator for performance. They designed a tool to monitor the flooding level in PEM fuel cells with interdigitated flow fields. Diperno and Fronk [18] filed a US patent for a method and a device that monitors the pressure drop across the flow fields to detect flooding in PEM fuel cells. Experimental diagnosis has been widely explored. Imaging techniques and measurements of physical indicators are available in the open literature [82]. Several modelling approaches have been published to gain insight on water flooding behaviour [30, 42, 26, 101, 52, 36].

The fuel cell components design and material properties also have a significant impact in the water management task. Several authors have reported changes in the component materials of the catalyst layers and GDL to improve the action of water removal [40]. Work has also been done on the design of the bipolar plate gas channels [106].

Membrane dehydration

The main cause of membrane dehydration is poor water management leading to a shortage of water. This condition is more likely to occur at the anode side and is called "drying out", which causes higher membrane protonic resistances and consequently a drop in cell voltage and overall cell power. Long-term operation of the membrane in a dried state can also derive in increased generation of radicals and, therefore, to an enhanced membrane degradation [58, 89]. A few works have presented results of membrane exposure to dryness for short-term and long-term periods showing reversible and irreversible damage scenarios [89]. Membrane degradation mechanisms will be reviewed later in this chapter. Anode dehydration is expected to be more serious at the inlet of the cell. The water back-diffusion to the anode is higher at the gas channel outlet due to changes in gas partial pressure along the anode channel. Moreover, under dehydrating conditions, the membrane pores shrink, which leads to even lower back-diffusion rates [59]. Three main reasons for dehydration were found in the literature:

(i) insufficient humidification of the fuel stream on the anode side, particularly at high temperatures where back-diffusion alone is not able to compensate the lack of water,

(ii) evaporation of water under extremely high operating temperatures [28],

(iii) strong electro-osmotic force in the presence of high current densities, specially upon step increases in the load where water replenishment by reactant humidification or back-diffusion is not quick enough to cope with the lack of water [22].

3.1.4   Load cycling

Fuel cells in some applications like automotive are exposed to challenging scenarios of rapid changes in load during their operating life. Apart from previously mentioned thermal stresses in cell components, a few studies have shown that platinum may dissolve rapidly when transitioning from low to high potentials, even though it is fairly stable at both high and low potentials [86]. These results have indicated that the chemical stability of new catalysts must be analysed at both steady high and low potentials, as well as load transition periods.

3.1.5   Start-stop cycling

Starting and stopping the fuel cell can induce considerable damage to its components. Several authors have explored this issue, which arises when the anode gas channel is filled with air after a shutdown action. Upon start-up, there will be a transient condition in which fuel exists at the channel inlet but the exit is still fuel-starved. This situation, known as "air-fuel front", can induce local potentials on the cathode in excess of 1.8 V relative to a hydrogen reference electrode [29]. Potential control, namely voltage clipping, has proven to be the most effective technique to mitigate this effect [34].

3.1.6   Cell exposure to impurities

Impurities present in both the hydrogen fuel stream and the air intake have a significant effect in fuel cell performance and durability. Currently, many fuel cell applications use hydrogen-rich gas produced by reforming of hydrocarbon fuels (natural gas, methanol, propane, gasoline and diesel). The reformation processes leave impurities in the gas entering the fuel stream. In addition, air pollutants might also enter the air side of the fuel cell.

The degradation mechanisms due to impurities in the reactants vary according to the chemical conditions of these substances. Some impurities absorb onto the anode or cathode catalyst layer affecting the electrode charge-transfer processes, which results in interfacial overpotential losses. Other impurities such as ammonia can form cations that reduce the protonic conductivity of the membrane, resulting in increased ohmic losses.

Performance losses due to impurities can be reversible or irreversible. In some cases, actions as simple as stop-starting the fuel cell can recover the performance, which is the case of CO contamination in the fuel stream. Table 3.1 summarises the most common impurities in both the fuel and air stream, their sources and their consequences on the fuel cell components. The intention of this subsection is to briefly explain the problems caused by impurities in the gas streams. Comprehensive reviews on this topic are presented in [84, 34].

Table 3.1: Most common fuel cell impurities in both the fuel and air streams

Fuel impurities		
Impurity	Source	Consequences
Carbon monoxide (CO)	Traces generated from hydrocarbon reforming processes.	Effects on the fuel cell are known as CO poisoning. This condition blocks the absorption of hydrogen onto active platinum (Pt) sites causing performance losses as a result of electrode overpotentials [34]. CO poisoning is reversible through different mechanisms. Stop-starting the fuel cell or introducing traces of oxygen into the fuel stream (air-bleed) are used as strategies to recover lost performance, althought both approaches have negative consequences to the cell [33].
Ammonia (NH_3)	Traces generated in the process of re-forming natural gas and other hydrocarbons for H_2 production.	The presence of ammonia levels as low as 13 ppm in the fuel stream has rapid negative effects on performance. Short-term exposure (less than 1 h) to NH_3 shows reversible effects. Long-term exposure effects are irreversible [35].
Hydrogen Sulphide (H_2S)	Traces generated in the process of reforming natural gas and other fuels from fossil origin.	This impurity affects Pt by blocking active sites. Poisoning by H_2S causes irreversible damage to the fuel cell.
Hydrocarbon contaminants	Reforming processes.	Effects on performance and durability on the fuel cell are not clear as some stationary systems operate in the presence of these impurities [34].
Anions, Cations	Water electrolysis.	Decreased protonic conductivity of the membrane [34].
Air impurities		
Sulfur dioxide (SO_2)	Results from fossil fuel combustion. It can be found in high concentrations in urban areas and near certain chemical plants.	Effects are similar to those produced by the presence of H_2S in the anode. Strong chemisorption onto the Pt catalyst surface. Reversible with certain techniques like cyclic voltammetry (CV) [109].
Nitrogen dioxide (NO_x)	Internal combustion engine emissions.	Performance degradation. Reversible effects [80].
Sodium chloride (NaCl)	Ocean mists and road deicer.	Effects on protonic conductivity at the membrane as a consequence of exchange of H^+ by Na^+ [24].

3.1.7 Cell exposure and start-up to freezing conditions

Exposure of non-operating fuel cells to freezing temperatures is one of the issues affecting durability. Any residual water in the cell will freeze after a prolonged period of time causing thermal and mechanical stress to its components. Repetitive cycles of ice formation on the membrane surface and melting into water can delaminate the catalyst layer from both the membrane and the GDL causing loss of proper interface contact. The thermal stresses in the membrane depend on the amount of water content at the time it freezes. The higher the membrane water content in the freezing cell, the thicker the ice layer. Certain freeze/thaw repetitive cycle studies (-30°C to 20°C) have shown more serious cracks on a fully hydrated membrane compared to a low humidified membrane at the moment of fuel cell shutdown

[34, 109, 80, 24, 114]. Degradation mechanisms of the membrane will be reviewed in the next section.

3.2   PEM fuel cell degradation mechanisms

This section describes the degradation processes of certain fuel cell components as a result of the issues presented in Section 3.1.

3.2.1   Polymer electrolyte membrane degradation mechanisms

Membrane degradation can be classified into three categories: (i) mechanical, (ii) thermal, and (iii) chemical/electrochemical [34]. Mechanical degradation causes failure due to perforations, cracks, tears, or pinholes, which may result from improper membrane electrode assembly (MEA) fabrication processes. During fuel cell operation, the overall dimensional change due to non-humidification, low humidification, and relative humidity cycling are also detrimental to mechanical durability [109]. A physical breach of the membrane due to local pinholes and perforations can result in crossover of reactant gases into their respective reverse electrodes. When this happens, the highly exothermic reaction of the oxidant and reductant occurs on the catalyst surface and consequently generates local hot points. A destructive cycle of increasing gas crossover and pinhole production is then stablished, which accelerates degradation of the membrane and the entire cell. The results of Huang et al. [80] suggested that mechanical failure of the membrane starts as a random, local imperfection that propagates to total failure.

Several studies have addressed the issue of thermal stability and thermal degradation of polymer electrolyte membranes (Nafion membranes). At high temperatures (beyond 150°C) Nafion begins to decompose via its side sulfonate acid groups. The thermal stability of Nafion was investigated by Surowiec and Bogozek [50] using differential thermal analysis.

Regarding electrochemical degradation of the membrane, the highly exothermal combustion between hydrogen and oxygen can possibly lead to pinholes in the membrane, destroying the MEA. More severly, the chemical reaction on the anode and cathode catalysts can produce peroxide and hydroperoxide radicals, which are commonly believed to be responsible for chemical attack on the membrane and catalysts [80]. Further investigation has also revealed that the generation of these radicals, as well as the chemical degradation of the membrane is accelerated when the fuel cell is operated under open circuit voltage (OCV) and low humidity conditions [24].

3.2.2   Catalyst layer degradation mechanisms

Corrosion of the catalyst carbon support is an important issue pertaining to catalyst layer durability that has attracted considerable attention lately in academic as well as in industry research [114]. In PEM fuel cells, two mechanisms are believed to induce carbon corrosion:

(1) transitioning between startup and shutdown cycles and (2) fuel starvation due to the blockage of hydrogen from a portion of the anode under steady state conditions. The first mechanism referred to as air-fuel front, can be caused by non-uniform distribution of fuel on the anode and crossover of oxygen through the membrane, which is likely to occur during startup and shutdown of the PEM fuel cell.

For the second mechanism, fuel cell starvation in individual cells may result from uneven flow sharing between cells during high overall stack utilization or from gas flow blockage attributed to ice formation when fuel cells work in subfreezing temperatures. In both cases the anode electrode is partially covered with hydrogen and, under the circumstances of hydrogen exhaustion, the anode potential will be driven negative until water and carbon oxidation takes place. When provided with sufficient water in the fuel cell, carbon is actually protected from corrosion by the water oxidation process, unless the water in the electrode is depleted or the cell is subjected to a high current density not sustainable by water oxidation alone [114]. Cell reversal as a result of fuel starvation has a potential impact on the durability of the catalyst layer, the gas difussion layer or even the bipolar plate.

3.2.3 Corrosion and mechanical degradation of the bipolar plates and gaskets

Corrosion of the bipolar plates also impacts performance and life of a fuel cell. Three major degradation mechanisms have been observed: (i) under permanent water contact, the material of the plates dissolves and it is either flushed away or travels into the membrane. The corrosion product staying in the cell accumulates and can poison the membrane. A problem in terms of efficiency arises when (ii) a resistive surface layer is formed on the plates, which results in a higher ohmic resistance. In addition, (iii) when high compressive pressure is used to seal the stack and ensure good conductivity, the mechanical stress may cause fracture and deformation of the bipolar plates [24, 114].

3.3 Conclusions

In this chapter, a literature review of state-of-the-art challenges for the PEM fuel cell technology has been presented, in order to identify the opportunities for novel contributions to the field. Clearly, the fuel cell control strategies play a major role in the achievement of optimal performance and reduction of different degradation mechanisms. The control of reactants distribution, water transport and cell temperature has an impact on every fuel cell component in terms of durability. In the case of external challenges like impurities in the fuel and air streams, as well as extreme temperatures, cell operation strategies are also key to prevent negative effects. Based on this review, the following chapter establishes the modelling and control objectives of the thesis, in the framework of distributed parameter modelling and control approaches.

Chapter 4

Modelling and control objectives

Chapters 2 and 3 introduced the PEM fuel cell technology theory and its current challenges. Figure 4.1 summarises the different performance and degradation issues that are subject of intensive research efforts by both industry and academia. This scheme presents the different challenges for optimal fuel cell operation and performance, as well as the consequences of these problems on cell reliability and durability. The content is not exhaustive but it involves the main areas of interest for this work. Details of these processes were presented in previous chapters. The image also highlights the operation tasks and components of a PEM fuel cell influenced by the results proposed in this thesis.
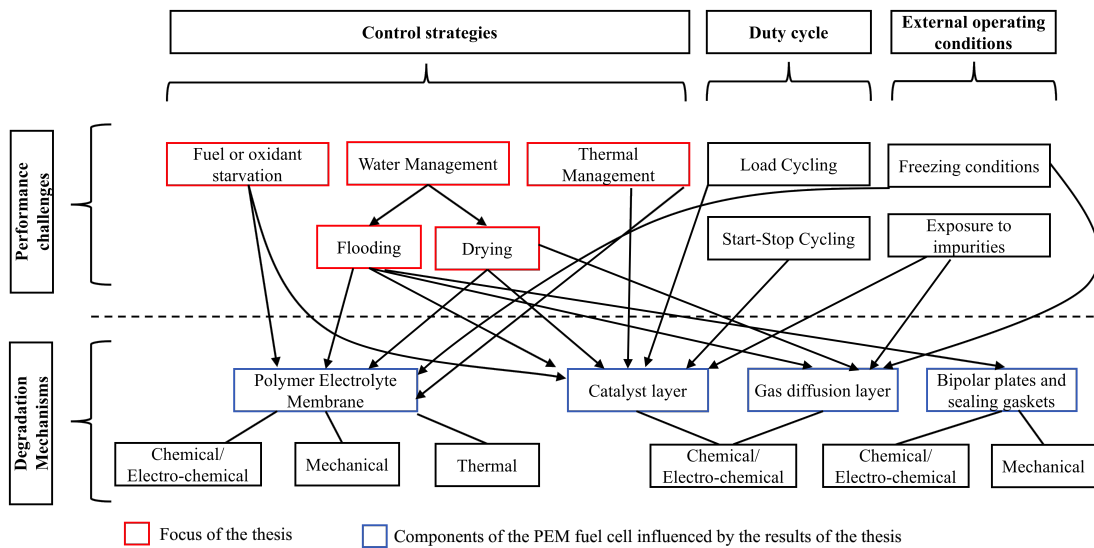
Figure 4.1: PEM fuel cell technology challenges

4.1   Delimitation of the problem

Water management is still a key challenge for optimal performance and durability of PEM fuel cells. As seen in previous chapters, proper water management requires meeting two conflicting requirements, (i) maintaining proper humidification of the membrane and catalyst layer for high proton conductivity, and (ii) avoiding cell drying or flooding on the cathode and anode sides of the membrane. Poor water management in the cell leads to significant performance loss and degradation. Section 3.1.3 describes the water management problem and its consequences in detail.

Water levels in the catalyst layers along the gas channels direction of a PEM fuel cell present important spatial variations that should be taken into account to avoid both local flooding and local drying. The partial pressure of water tends to be higher towards the gas channel outlet due to decreased reactant concentrations, increasing flooding likelihood. On the other hand, strong electro-osmotic forces at the channel inlet can cause drying on the anode side. These are only two examples that indicate the advantage of spatial control strategies.

As explained in Section 3.1.1, fuel or oxidant starvation can cause severe degradation. Higher levels of reaction rate occur towards the gas inlet end of the channels where reactants partial pressure is higher, therefore, the last sections along the gas channels direction are more vulnerable to starvation. However, starvation could occur anywhere along the flow direction due to the presence of liquid water or degradation issues, which makes a spatial control approach the appropriate to prevent such problems.

Membrane water content has also important spatial profile variations along the gas channels direction. Proper thermal management is key to maintain the membrane water content at healthy levels. Monitoring the spatial profile of the membrane water content to take temperature control actions is required to prevent local degradation. Details of the thermal management issue and membrane degradation mechanisms are presented in Chapter 3. Therefore, this thesis targets water management, reactant starvation and membrane water content issues.

4.2   Modelling and control objectives of the thesis

The scope of the work in this thesis is framed within the PEM fuel cell advanced modelling and control strategies field of study. A non-linear distributed parameter model of a single PEM fuel cell is first developed and validated, in order to take into account spatial profiles of the most important internal fuel cell variables. Some of these variables are key for water management, reactant starvation and membrane water content issues. This model is later simplified for control strategies design purposes.

In the control part of the thesis, decentralised model predictive control schemes are designed and implemented to maintain the water activity on both anode and cathode sides

of the PEM at appropriate levels. The decentralised feature consists of two distributed parameter model predictive controllers. One of the controllers focuses on the anode side and the other focuses on the cathode side. Each controller uses an order-reduced reference model derived from the non-linear PEM fuel cell model previously developed. Two model order reduction techniques are considered to decrease the complexity of the non-linear submodels of anode and cathode. The resulting order-reduced reference models are linear with adaptive features.

The proposed strategies tackle the rate of accumulation of liquid water on the surface of the catalyst layers, and the possibility of local drying, by controlling observed water activity spatial profiles. Classic PEM fuel cell issues like reactant starvation are also considered. Moreover, the decentralised feature of the control scheme has important impact on the overall control performance due to the use of order-reduced models within each model predictive controller. The strategy is applied to the developed and validated non-linear distributed parameter PEM fuel cell model, in order to analyse performance differences in comparison to non-spatial control strategies.

Model predictive control (MPC) is part of the family of the optimisation-based control methods that use on-line optimisation for future control steps. An MPC controller uses a reference model to predict system response. It can therefore be used to estimate future states and set the actuators accordingly, improving convergence time and avoiding oscillations in controlled and manipulated signals [19]. Clearly, there is a trade-off between the accuracy of the reference model and the computational complexity of the controller. The use of MPC in this work, being a classic model-based approach, allows the consideration of spatial variations of water activity and other cell variables by using distributed parameter models as reference models.

Spatial variations of water activity and most internal profiles of fuel cell variables are difficult or impossible to measure by sensors and, if possible, the increase in cost is not desirable given the technology challenges. Therefore, it is necessary to estimate these profiles using observers. State observers are able to estimate the internal states of a real system from measures of corresponding inputs and outputs [61, 25]. Details of the overall design of the control strategies will be given in the following chapters.

In summary, the detailed modelling and control objectives of the thesis, expanding those presented in Section 1.4 are:

(1) To develop a non-linear distributed parameter model that incorporates the effects of spatial variations of variables that are relevant to the proper performance of PEM fuel cells. Some of these variables are key for water management, reactant starvation and membrane water content issues.

(2) To simplify the distributed parameter model in order to make it suitable for control purposes and efficient numerical simulations. In this task, two model order reduction

techniques will be applied.

(3) To design and implement state observers that are able to estimate the internal states of the PEM fuel cell from measures of corresponding inputs and outputs.

(4) To design, implement and analyse distributed parameter model-based controllers and control strategies, in order to tackle water management, reactant starvation and membrane water content issues.

In this chapter, modelling and control objectives have been established for this thesis. The following chapter presents the distributed parameter PEM fuel cell model developed including: governing equations of the phenomena occurring within a PEM fuel cell, derived from first principles and empirical models, corresponding discretisation of the equations and the description of considered fuel cell components, as well as model validation approaches.

Part II

Modelling

Chapter 5

Distributed parameter modelling of a single PEM fuel cell

Considerable progress has been made in modelling and simulation of PEM fuel cells, reflecting the importance of having accurate models to understand the behaviour of the cells, assess potential improvements to the different components and design control solutions. In the first sections, this chapter presents a compact literature review of the state of the art in modelling approaches for PEM fuel cells. The main part of the chapter covers the development of a modular PEM fuel cell distributed parameter model, including the description of governing equations for fuel cell processes, analysis of components where these processes take place, discretised equations for simulation and control purposes and model validation.

5.1   PEM fuel cell modelling literature review

The internal behavior of a PEM fuel cell is very complex because of the different and tightly coupled phenomena that occur within a cell: fluid-dynamics phenomena, diffusion, migration, electrochemical reactions, proton transport through proton-conductive polymer membrane, electron conduction through electrically conductive cell components, water transport through polymer membrane including both electro-osmotic drag and back diffusion, water transport (both vapour and liquid) through porous catalyst layers and gas diffusion layers, heat transfer, including both conduction through solid components of the cell and convection of reactant gases and cooling medium, and phase changes (see Figure 5.1).

Modelling is necessary to describe these fundamental phenomena and evaluate cells steady-state and dynamic response. However, the complicated processes inside the fuel cell make the modelling task particularly challenging. In addition, some models include the reactants supply systems, the cooling system, the humidification system and the conditioning system of electric energy generated. Several works on modelling of PEM fuel cells can be found in the literature. Models are also used to predict fuel cell performance under differ-

ent operating conditions, reveal the distribution details of various space dependent variables and optimise the design of fuel cell control systems [81, 108, 87, 69, 77, 12].

There are different types of PEM fuel cell models depending on the purpose they serve. A first kind of models is focused on specific parts of the fuel cell, such as the gas channel, the gas diffusion layer, the catalyst layer, or the polymer electrolyte membrane [108, 87]. A second kind of models focuses on a single cell to describe electrochemical and transport processes in each fuel cell component. Stack level models consider the arrangements of more than one cell to supply the required power demand. The so-called system level models are focused on the entire fuel cell stack and the auxiliary components that form a complete fuel cell system.

Models can also be classified depending on the dimensionality considered: one, two or three-dimensional. Processes can be considered either isothermal or non-isothermal [69, 77, 12]. Two-phase flow models or single-phase flow models can also be differentiated, whether liquid water formation within the cell is a phenomenon of interest [30, 42, 26, 101, 52, 36, 102]. Another important classification of PEM fuel cell models depends on the consideration of spatial variations of variables. System level models are often lumped parameter models. Stack level and single cell models are most likely to be distributed parameter models given the complexity of the fuel cells. However, control-oriented models for single cells, stacks or systems tend to be lumped-parameter for control design purposes.

In the following sections, there is a very brief review of the most important system/stack level control-oriented models available in the literature and a more detailed review on single cell models, as these will be the subject of the thesis.

5.1.1   Single cell models

Single cell models describe the electrochemical and transport processes in each fuel cell component, and the pressure drop, flow distribution, and temperature profile in the gas channels. These models, which quantitatively describe interactions among the various physical and electrochemical phenomena can also be divided into two groups of models: empirical models and first principles models. Most empirical models use simple empirical equations to predict how the fuel cell voltage changes with the current density (polarisation curves) at different operating conditions [94]. First principles models are built-up from ordinary differential equations (lumped parameter models) or partial differential equations and corresponding algebraic conditions (distributed parameter models) that allow the detailed study of fundamental phenomena. A distributed parameter system is one in which at least some dependent variables are functions of time and one or more spatial variables. In this case, solving partial differential equations (PDEs) is required.

For the vast majority of first principles models, Stefan-Maxwell convection and diffusion account for species conservation. Gas flow through porous media is computed using Darcy's law. The principle of mass conservation is used to model reactants concentrations.
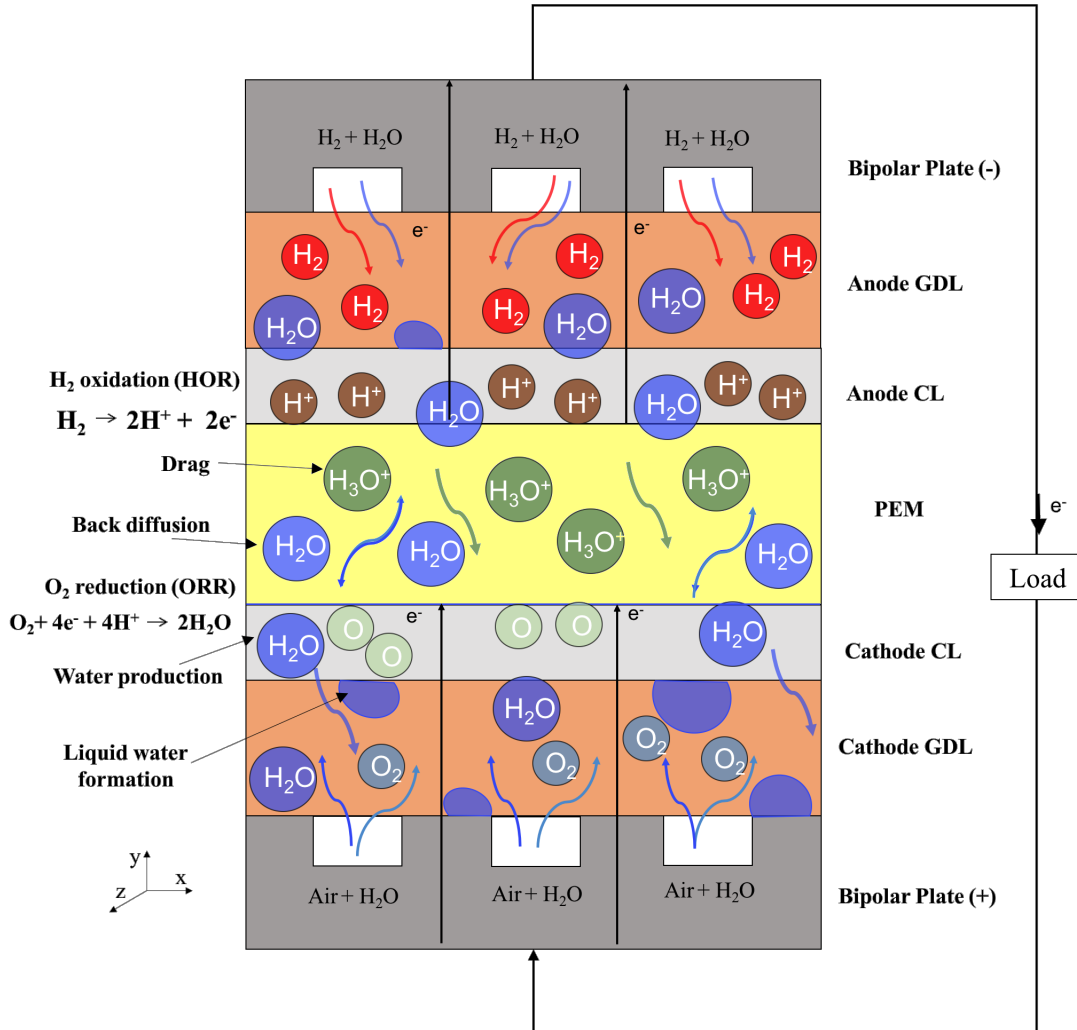
Figure 5.1: Processes occurring within a PEM fuel cell

Membrane behaviour (Nafion) is described by calculating membrane water content, water concentration, drag coefficient, net water flux, and protonic conductivity. Heat transfer by convection and conduction is implemented to describe overall thermal behaviour. Several single PEM fuel cell models can be found in the literature. As indicated before, these models can be classified by: dimension, isothermal/non-isothermal, single phase flow/two-phase flow.

In the early 1990's, Bernardi and Verbrugge [108] and Springer et al. [87] made a considerable effort to develop pioneering first principles models. These models, both one dimensional, analysed species transport, water addition and removal, cathode flooding and the effect of gas humidification. Later, Rowe and Li [81] developed a one-dimensional non-isothermal model of a PEM fuel cell, incorporating water and temperature distribution to investigate the operating conditions on the cell performance, thermal response and water

management. More recently, two-dimensional and three dimensional models have been developed.

The two-dimesional models can be divided into two categories. One group of models describes the plane perpendicular to the flow channels, while the other group of models describes the direction along the flow channel [30, 42, 26, 101, 52, 36]. Each group has its advantages and drawbacks. The first group of models studies the effect of flow channel dimension and configuration, however, changes in the temperature and reactants fraction cannot be analysed. The second group of models can predict the temperature and concentration profiles along the direction of the flow channel, but cannot simulate the effect of flow channel and rib size. Most recently three-dimesional models have been developed by various research groups [87]. An important three-dimensional, two-phase, non-isothermal unit cell model was developed by Tao [94] in order to perform parameter sensitivity examination.

5.1.2   System and stack level control-oriented models

Usually, system level models are lumped parameter models used to evaluate fuel cell performance under different operating conditions and to design controllers. A lumped system is one in which the dependent variables of interest are a function of time alone. In general, this will mean solving a set of ordinary differential equations (ODEs). Pukrushpan [77] developed a system level model that includes the fuel cell stack, the hydrogen supply system, the air supply system, the cooling system and the humidification system. The stack temperature is considered constant because of the slow dynamics of this variable compared to the transient dynamics included in the model. Temperature and humidity of the inlet reactant flows are controlled by humidity and cooling sub-systems. Suh [93] reduced Pukrushpan's model from nine to five states to focus on the control of the voltage conditioning system. Later, Bao et al. [12] developed a system-level model for integrated control study of the air stream.

5.2   Distributed parameter PEM fuel cell model development

This work focuses on a single-channel single cell that includes all the functional parts of the fuel cell. Although this element only considers one channel of the cell, it is a fine representation of the entire cell, given the periodicity of the process. This kind of models meets the purpose of this work because its simplicity facilitates the analysis and control of spatial variations of temperature, reactants concentration, water activity in the catalyst layers and GDL or water content in the membrane, which are important variables related to fuel cell water management and corresponding degradation mechanisms [50].

The system under study is a single-channel single PEM fuel cell that consists of gas channels (GCs), gas diffusion layers (GDLs), catalytic electrodes (CLs), the polymer electrolyte membrane (PEM), current collector plates (end plates) and a liquid cooling system.

Figure 5.2 shows a complete structure of the cell considered.
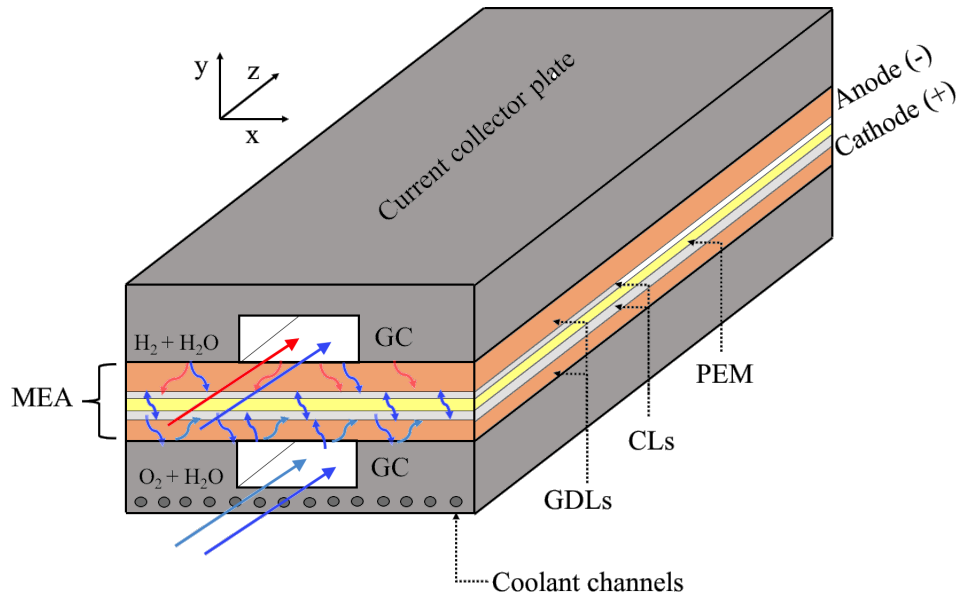
Figure 5.2: Single PEM fuel cell model structure

The phenomena modelled inside the MEA includes: gas diffusion through porous media, electrochemistry reactions, proton transport through proton-conductive polymer membrane, water transport through polymer membrane, including both electro-osmotic drag and back diffusion, electron conduction through electrically conductive cell components and thermal transport. Outside the MEA, the phenomena is described by models of mass and thermal transport. Figure 5.3 shows the scheme of the overall distributed parameter fuel cell model to be developed in this chapter.

A distributed parameter model is one in which all dependent variables are functions of time and one or more spatial variables. In this case, solving partial differential equations (PDEs) is required. This model is non-linear with dimension $1 + 1D$, which considers transport through the MEA as a series of lumped parameter models, i.e. one single volume for each layer of the cell in the y-direction, coupled to 1D models in the direction of the gas flows, i.e. spatial gradients in the z-direction of each layer of the cell. The 1D direction has been discretised in n segments using the central finite differences approach. Some variables of interest for control design purposes are also shown in the scheme. The following sections describe the model processes, components and equations in detail.

5.2.1 Model assumptions

The model is built upon the following assumptions:

- Fluid in gas channels and in the gas diffusion layers behaves like an ideal gas.
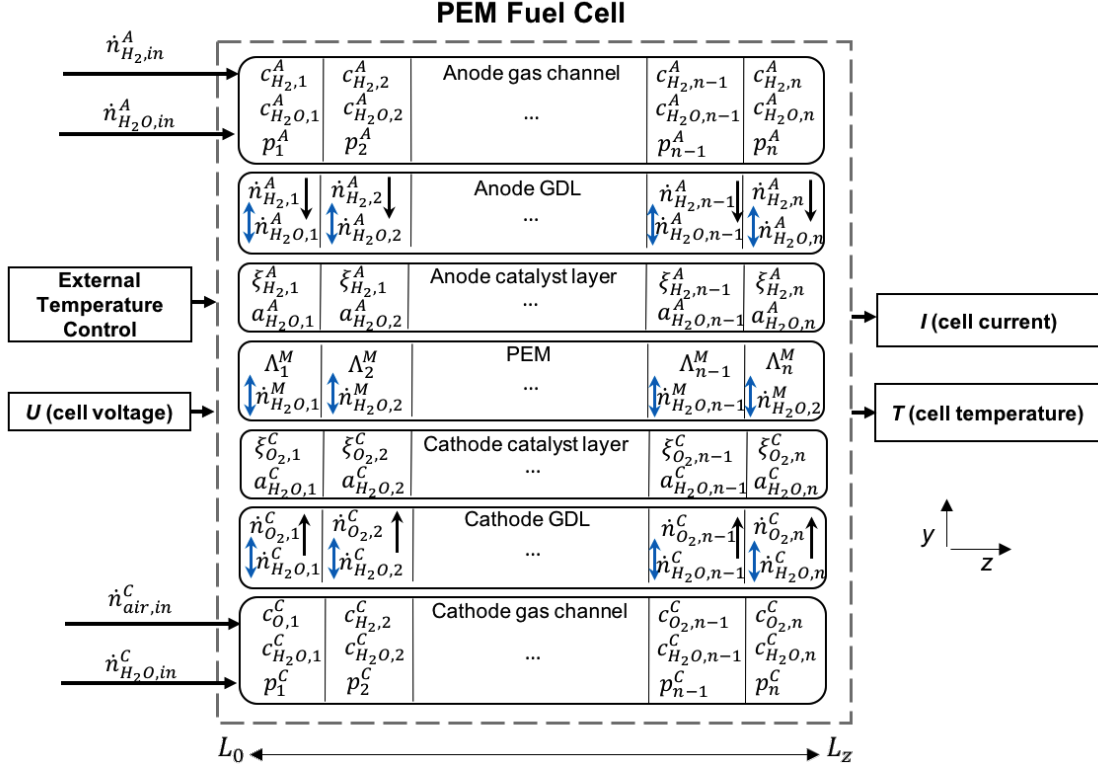
Figure 5.3: Distributed parameter PEM fuel cell model scheme

- Gas channels possess storage capacity for mass and energy.

- No storage capacity for mass is considered for the gas diffusion layers and the catalyst layers.

- Pressure at the outlet of the gas channels is equal to ambient pressure.

- Liquid water formation in the catalyst layers is acknowledged through an empirical model that estimates the effects of water coverage on the electrochemical surface area.

- The membrane is able to store water. Electrical conductivity depends on its water content.

- The MEA components, i. e. membrane, catalyst layers and gas diffusion layers, are on the same temperature level T.

- There are no gradients of electrical potential in the electrodes in the y-direction.

- The ohmic resistance of the cell is caused by the membrane only.

- Fuel and electrons crossover losses and other mass transport losses are not considered. The cell model will be operated in the ohmic region of the polarisation curve.

5.2.2   Model inputs and outputs

There are 6 inputs to the cell: the voltage U, according to a certain duty cycle, the cooling temperature input, the hydrogen inlet $\dot{n}_{H_2,in}^A$ and the anode water inlet $\dot{n}_{H_2O,in}^A$, the oxygen/nitrogen inlet $\dot{n}_{air,in}^C$ and the cathode water inlet $\dot{n}_{H_2O,in}^C$. The model measured outputs are the cell current I and temperature T.

5.2.3   Gas channels submodel

Gas channels are pathways for flow of reactant gases, housed by the bipolar plates or end plates in the case of a single cell. Physical phenomena occurring within the GCs can be represented by the solution of balance equations for mass, momentum and energy. Convective transport in the z-direction and y-direction is studied.

Mass balances

The general equation for mass conservation is

$$\frac{\partial \rho}{\partial t} + \boldsymbol{\nabla} \cdot (\rho v) = 0, \tag{5.1}$$

where $\boldsymbol{\nabla} \cdot = \frac{\partial}{\partial z} + \frac{\partial}{\partial y}$, ρ represents density and v is the velocity vector. The transient term represents accumulation of mass with time, and the second term represents the change in mass flow [56]. Derived from 5.1, the mass balances for the anode and cathode gas channels are,

$$\frac{\partial c_i^j}{\partial t} = -\frac{\partial v^j c_i^j}{\partial z} - \frac{\dot{n}_i^j}{\delta^j}. \tag{5.2}$$

In this model molar mass is used instead of mass. The corresponding boundary equations are,

$$v^j c_i^j|_{0,t} = \dot{n}_{i,in}^j \tag{5.3}$$

The superscript j is used to denote anode side (A) or cathode side(C). The subscript i indicates the species index. On the anode side, it can be either H_2 or H_2O. On the cathode side, i can be either O_2, N_2 or H_2O. The water component is present for hydrogen and air humidification [13]. Gas channel thickness in y-direction is δ^j, $\dot{n}_i^j$ denote molar flow densities between gas channels and gas diffusion layers (convective flows in y-direction), $\dot{n}_{i,in}^j$ denote inlet molar flow densities (inlet flow divided by cross-sectional area of the gas channels). Molar flow densities are assumed positive towards the membrane. The general equation for mass conservation is discretised as follows

$$\frac{dc_{i,k}^j}{dt} = -\frac{v_k^j c_{i,k}^j - v_{k-1}^j c_{i,k-1}^j}{\Delta z} - \frac{\dot{n}_{i,k}^j}{\delta^j}. \tag{5.4}$$

Sub-script $k = 1, 2 \ldots n-1, n$ accounts for mesh segment number. The discretised boundary conditions are

$$v_0^j c_{i,0}^j|_{0,t} = \dot{n}_{i,in}^j, \tag{5.5}$$

which are the algebraic equations used to calculate concentrations at the beginning of the gas channels. In these relations, the terms $\dot{n}_{i,in}^j$ denote inlet molar flow densities (inlet flow divided by cross-sectional area - CCSA of the gas channels).

Flow velocity

Normally, velocity vectors for flow dynamics are determined by the conservation of momentum equations, the so-called Navier-Stokes equations [56]. Considering a set of assumptions, such as neglecting the acceleration terms, the Navier-Stokes equations can be simplified into a pressure drop relation similar to Darcy's law [56]. This is how the flow velocity is calculated in the gas channels,

$$v^j = -K^j \frac{\partial p^j}{\partial z}. \tag{5.6}$$

The corresponding boundary condition, considering pressure at the outlet of the gas channels equal to ambient pressure is

$$p^j (L_z, t) = p^{amb}. \tag{5.7}$$

Discretisation of flow velocities for both anode gas channel and cathode gas channel using forward differencing is

$$v_k^j = -K^j \frac{p_{k+1}^j - p_k^j}{\Delta z}, \tag{5.8}$$

considering corresponding boundary condition,

$$v_n^j = -K^j \frac{p^{amb} - p_n^j}{\Delta z}. \tag{5.9}$$

Flow pressure

Following model assumptions, ideal gas law is used to calculate flow pressure in the gas channels, and this equation also relates pressure with total gas concentration. This is

$$p^j = RT^j \sum_i c_i^j, \tag{5.10}$$

and the corresponding discretised equation is

$$p_k^j = RT_k^j \sum_i c_{i,k}^j. \tag{5.11}$$

Energy balance

Accumulation of energy in the gas channels is described by

$$\frac{\partial (\rho u)^j}{\partial t} = -\frac{\partial}{\partial z}\left(\sum_i v^j c_i^j h_i\left(T^j\right)\right) + \lambda^j \frac{\partial^2 T^j}{\partial z^2} + \frac{\alpha_1}{\delta^j}\left(T - T^j\right) - \sum_i \frac{\dot{n}_i^j}{\delta^j} h_i\left(T^j\right), \tag{5.12}$$

where energy changes are given by the terms on the right hand side of 5.12. The first term describes energy transport in the z-direction due to convective flow. The second term represents heat conduction according to Fourier's law [49]. The third term is heat transfer between MEA parts at temperature T and gas channels. The last term describes another type of convective flow from gas channels to the MEA. This is also an enthalpy transport. The boundary equations are

$$\sum_i \dot{n}_{i,in}^j h_i\left(T_{in}^j\right) = \sum_i v^j c_i^j h_i\left(T^j\right)|_{0,t} - \lambda^j \frac{\partial T^j}{\partial z}|_{0,t}, \tag{5.13}$$

$$\lambda^j \frac{\partial T^j}{\partial z}|_{L_z,t} = 0. \tag{5.14}$$

The discretised equation for accumulation of energy in the gas channels is,

$$\begin{aligned}
\frac{d (\rho u)^j}{dt} &= -\frac{1}{\Delta z}\left(\sum_i v_k^j c_{i,k}^j h_{i,k}\left(T_k^j\right) - \sum_i v^j c_{i,k-1}^j h_{i,k-1}\left(T_{k-1}^j\right)\right) \\
&+ \lambda^j \frac{T_{k+1}^j - 2T_k^j + T_{k-1}^j}{\Delta z^2} + \frac{\alpha_1}{\delta^j}\left(T_k - T_k^j\right) - \sum_i \frac{\dot{n}_{i,k}^j}{\delta^j} h_{i,k}\left(T^{j,k}\right). \tag{5.15}
\end{aligned}$$

The boundary equations discretised using backward differencing are,

$$\sum_i \dot{n}_{i,in}^j h_i\left(T_{in}^j\right) = \sum_i v_0^j c_{i,0}^j h_i\left(T^j\right)|_{0,t} - \lambda^j \frac{T_1^j - T_0^j}{\Delta z}|_{0,t}, \tag{5.16}$$

$$\lambda^j \frac{T_n^j - T_{n-1}^j}{\Delta z}|_{L_z,t} = 0. \tag{5.17}$$

Temperature

In order to calculate temperature in the gas channels, a thermodynamic equation of state is used [49],

$$(\rho u) + p^j = \sum_i c_i^j h_i \left(T^j \right).$$ (5.18)

The discretised temperature equation is,

$$(\rho u)_k^j + p_k^j = \sum_i c_i^{j,k} h_{i,k} \left(T_k^j \right).$$ (5.19)

5.2.4 Gas diffusion layers submodel

The layer between the catalyst layer and the gas channels is the gas diffusion layer, electrode substrate, or diffusor/current collector. This layer (one for each side of the membrane) does not directly participate in the electrochemical reactions, but it has several important functions [13]. The purpose of the GDL model is to introduce a mass transport limitation between gas channels and catalyst layers. The Stefan-Maxwell diffusion equations for a multicomponent gas mixture [17] are used to define the gradient in mole fraction of the components in y-direction,

$$-\bigtriangledown \xi_i^j = \sum_{ks} \frac{\bar{\xi}_{ks}^j \dot{n}_i^j - \bar{\xi}_i^j \dot{n}_{ks}^j}{\bar{c}^j D_{i,ks}^{eff}},$$ (5.20)

where ξ_i^j is the mole fraction of gas species in the gas channels and $D_{i,ks}^{eff}$ is the gas diffusion coefficient between two gas species. In equation (5.24) $j = A$, C; $i = $ H$_2$, H$_2$O for $j = A$ and $i = $ O$_2$, N$_2$, H$_2$O for $j = C$. Similar to i, the new subscript ks is also used to denote gas species, in order to account for all the possible combinations on each side of the membrane. In the y-direction, the gradient of mole fraction $\bigtriangledown \xi_i^j$ is approximated by

$$\bigtriangledown \xi_i^j = \frac{\xi_i^{Cj} - \xi_i^j}{\delta^{Gj}},$$ (5.21)

where δ^{Gj} is the thickness of the gas diffusion layers. Molar fractions inside the GDL are

$$\bar{\xi}_i^j = \frac{1}{2} \left(\xi_i^{Cj} + \xi_i^j \right),$$ (5.22)

where ξ_i^{Cj} denotes mole fractions in the catalyst layers. Finally, the total gas concentration in the GDLs follows from

$$\bar{c}^j = \frac{p^j}{RT}.$$ (5.23)

The set of discretised equations used to calculate mole fractions $\xi_{H_2,k}^{CA}$ and $\xi_{O_2,k}^{CC}$ in the catalyst layers is

$$-\bigtriangledown \xi_{i,k}^j = \sum_{ks} \frac{\bar{\xi}_{ks,k}^j \dot{n}_{i,k}^j - \bar{\xi}_{i,k}^j \dot{n}_{ks,k}^j}{\bar{c}^j D_{i,ks}^{eff}},$$ (5.24)

where ks index is used in this case for gas species, in order to avoid confusion with the k index for mesh segments in the original equation. The gradient of mole fraction $\bigtriangledown \xi_i^j$ is

$$\bigtriangledown \xi_{i,k}^j = \frac{\xi_{i,k}^{Cj} - \xi_{i,k}^j}{\delta^{Gj}}. \tag{5.25}$$

The composition inside the GDL $\bigtriangledown \xi_i^j$ is

$$\bar{\xi}_{i,k}^j = \frac{1}{2} \left(\xi_{i,k}^{Cj} + \xi_{i,k}^j \right), \tag{5.26}$$

Finally, the total gas concentration in the GDLs follows from

$$\bar{c}_k^j = \frac{p_k^j}{RT_k}. \tag{5.27}$$

5.2.5   Catalyst layers submodel

The catalyst layer is the functional core of the PEM fuel cell, pressed between the membrane and the porous gas diffusion layer. It is the layer where the electrochemical reactions take place on anode side and cathode side. In this model the CLs are assumed to have no mass storage capacity and no gradients in y-direction.

Mass fluxes through diffusion layers

Due to model assumptions, hydrogen mass flow from the anode gas channel to catalyst layer is identical to the amount of hydrogen consumed in the anodic reaction $H_2 \rightarrow 2H^+ + 2e^-$

$$\dot{n}_{H_2}^A = r^A, \tag{5.28}$$

where r^A is the rate of the anodic reaction. The net water flow from or to the anode gas channel through the gas diffusion layer depends on membrane water transport,

$$\dot{n}_{H_2O}^A = \dot{n}_{H_2O}^M, \tag{5.29}$$

The oxygen transported from the cathode gas channel is completely consumed in the cathodic reaction $O_2 + 4e^- + 4H^+ \rightarrow 2H_2O$. This is

$$\dot{n}_{O_2}^C = \frac{1}{2} r^C. \tag{5.30}$$

where r^C is the rate of the anodic reaction.Nitrogen is not a reactant, therefore, nitrogen flux cannot permeate through the membrane,

$$\dot{n}_{N_2}^C = 0. \tag{5.31}$$

Water flow from the cathode is given by the cathode catalyst layer water mass balance,

$$\dot{n}_{H_2O}^{C} = -\dot{n}_{H_2O}^{M} - \dot{n}_{H_2O}^{reac}, \tag{5.32}$$

where $\dot{n}_{H_2O}^{M}$ accounts for drag and back diffusion. Generated water from the cathode electrochemical reaction is represented by the second term on the right side of the equation,

$$\dot{n}_{H_2O}^{reac} = r^{C}. \tag{5.33}$$

Discretised equations used to determine the values of the mass fluxes at each mesh segment are

$$\dot{n}_{H_2,k}^{A} = r_k^{A}, \tag{5.34}$$

$$\dot{n}_{H_2O,k}^{A} = \dot{n}_{H_2O,k}^{M}, \tag{5.35}$$

$$\dot{n}_{O_2,k}^{C} = \frac{1}{2}r_k^{C}, \tag{5.36}$$

$$\dot{n}_{N_2,k}^{C} = 0, \tag{5.37}$$

$$\dot{n}_{H_2O,k}^{C} = -\dot{n}_{H_2O,k}^{M} - \dot{n}_{H_2O,k}^{reac}, \tag{5.38}$$

$$\dot{n}_{H_2O,k}^{reac} = r_k^{C}. \tag{5.39}$$

Water activity in the catalyst layers

The water vapour activity (or water activity) on each side of the membrane is calculated from water partial pressure divided by corresponding saturation pressure according to cell temperature. Discretised equation is

$$a_{H_2O,k}^{j} = \frac{p_k^{j}\xi_{H_2O,k}^{Cj}}{p_k^{sat}}, \tag{5.40}$$

where $\xi_{H_2O,k}^{Cj}$ represents the mole fraction of water in each catalyst layer. Saturation pressure p^{sat} is determined from the empirical relation given by [13],

$$p_k^{sat} = \exp\left\{19.016 - \left(\frac{4064.95}{(T_k + 236.250)}\right)\right\}, \tag{5.41}$$

where T_k is the temperature of a particular cell segment.

Water activity values higher than one indicate condensation on the catalyst layers. In this model, liquid water coverage is approximated by flagging up the presence of conden-

sation when the average of the water activity spatial profile in the anode ($a_{H_2O,avrg}^A$) or cathode ($a_{H_2O,avrg}^C$) catalyst layer reaches the value one. The water film coverage on each side of the membrane is assumed to decrease reactant access to the electrochemical surface area (ECSA), according to estimated steady-state water coverage ratios in the gas diffusion layers from experimental results reported in [85]. This is a very simple empirical logic developed in this model to account for the effects of accumulated liquid water in the fuel cell, in order to visualise the benefits of control strategies proposed in Section 8.3. Table 5.1 shows this empirical function in detail.

Table 5.1: ECSA approximation function

For both anode and cathode catalyst layers ($j = A, C$):
Set ECSA theoretical value on anode and cathode to 5 cm^2,
Set accumulation timer t_j to zero,
While simulation is running, increment t_j by 1 every second and do:
If $a_{H_2O,avrg}^j \leqslant 1$
Reset t_j,
else if $a_{H_2O,avrg}^j > 1$ and $t_j > 5$ s
If $I > 0.5$ A cm^{-2}
Reduce ECSA by 1% if anode and 0.01% if cathode,
Reset t_j,
else if $I > 0.2$ A cm^{-2}
Reduce ECSA by 2% if anode and 0.05% if cathode,
Reset t_j,
else
Reduce ECSA by 4% if anode and 1% if cathode,
Reset t_j,
end
end

In this logic a 5 cm^2-active area single PEM fuel cell example is considered. The ratios of water film coverage at steady-state current values include the effect of water removal by the gas flow rates, therefore ECSA reduction due to water coverage is greater at lower cell current levels. The accumulation time value is 5 seconds, which is representative of rapid duty cycle changes in the operation of the cell, with steady-state behaviour towards the end of the 5-second slot. Active area recovery after a water removal action is not modelled since the focus is on the accumulation rate before such action.

Electrochemistry reactions kinetic rates

The rate of an electrochemical reaction is determined by an activation energy barrier that the charge must overcome in moving from an electrolyte to a solid electrode or vice versa [20]. The speed at which an electrochemical reaction proceeds on the electrode surface is the rate at which the electrons are released or "consumed"; this is the electrical current.

The reaction rates are modeled by Butler-Volmer equations, which are a current density-potential relations, and Faraday's law [13], which states that current density is proportional to the charge transferred and the consumption of reactant per unit area. For the anode reaction the kinetic rate is [105],

$$r^A = f^V \frac{i_{A_0}}{2F} \left[exp \left(\frac{2F}{RT} \left(\Delta \Phi^A - \Delta \Phi^A_{ref} \right) \right) \frac{\xi^{CA}_{H_2} p^A}{p_{H_2,ref}} - 1 \right], \tag{5.42}$$

where f^V is a parameter related to the platinum catalyst loading and i_{A_0} is the corresponding exchange current density. The Butler-Volmer equation is similar to the the Tafel equation in that it is a current density-potential relation. Tafel equation was used in section 2.5.1 to describe the activation polarisation losses. For the cathode reaction the kinetic rate is [105]:

$$r^C = f^V \frac{i_{C_0}}{2F} exp \left[\frac{\Delta G_0}{R} \left(\frac{1}{T} - \frac{1}{T_{ref}} \right) \right] \frac{\xi^{CC}_{O_2} p^C}{p_{O_2,ref}} \text{ x } exp \left[\frac{\alpha 2F}{RT} \left(\Delta \Phi^C - \Delta \Phi^C_{ref} \right) \right], \tag{5.43}$$

where $\Delta \Phi^A$ and $\Delta \Phi^C$ are space dependent potential differences of the anode and the cathode double layer, i_{C_0} is the corresponding exchange current density and ΔG_0 refers to activation energy. These terms are defined by

$$\Delta \Phi^A (z,t) = \Phi^A (t) - \Delta \Phi^{AM} (z,t), \tag{5.44}$$

$$\Delta \Phi^C (z,t) = \Phi^C (t) - \Delta \Phi^{CM} (z,t), \tag{5.45}$$

where Φ^{AM} and Φ^{CM} are potentials of the membrane on the anode side and on the cathode side. Anode and cathode potentials are related by

$$U(t) = \Phi^C (t) - \Phi^A (t). \tag{5.46}$$

Corresponding discretised equations for the kinetic rates are

$$r^A_k = f^V \frac{i_{A0}}{2F} \left[exp \left(\frac{2F}{RT_k} \left(\Delta \Phi^A_k - \Delta \Phi^A_{ref} \right) \right) \frac{\xi^{CA}_{H_2,k} p^A_k}{p_{H_2,ref}} - 1 \right], \tag{5.47}$$

$$r^C_k = f^V \frac{i_{C0}}{2F} exp \left[\frac{\Delta G_0}{R} \left(\frac{1}{T_k} - \frac{1}{T_{ref}} \right) \right] \frac{\xi^{CC}_{O_2,k} p^C_k}{p_{O_2,ref}} \text{ x } exp \left[\frac{\alpha 2F}{RT_k} \left(\Delta \Phi^C_k - \Delta \Phi^C_{ref} \right) \right]. \tag{5.48}$$

Figure 5.4 depicts the submodels of the anode and cathode of the PEM fuel cell framed in the dashed boxes. The main variables are shown in the image. Black arrows indicate

fluxes of reactants ($\dot{n}^A_{H_2,k}$ and $\dot{n}^C_{O_2,k}$ variables) and proton flux ($\dot{n}^+_k$). Blue arrows describe water transport processes ($\dot{n}^A_{H_2O,k}$, $\dot{n}^C_{H_2O,k}$ and $\dot{n}^M_{H_2O,k}$ variables). Bi-directionality of the blue arrows denotes water flow that could be from the anode to the cathode or vice versa, depending on the water activity levels on the catalyst layers and the membrane transport processes.
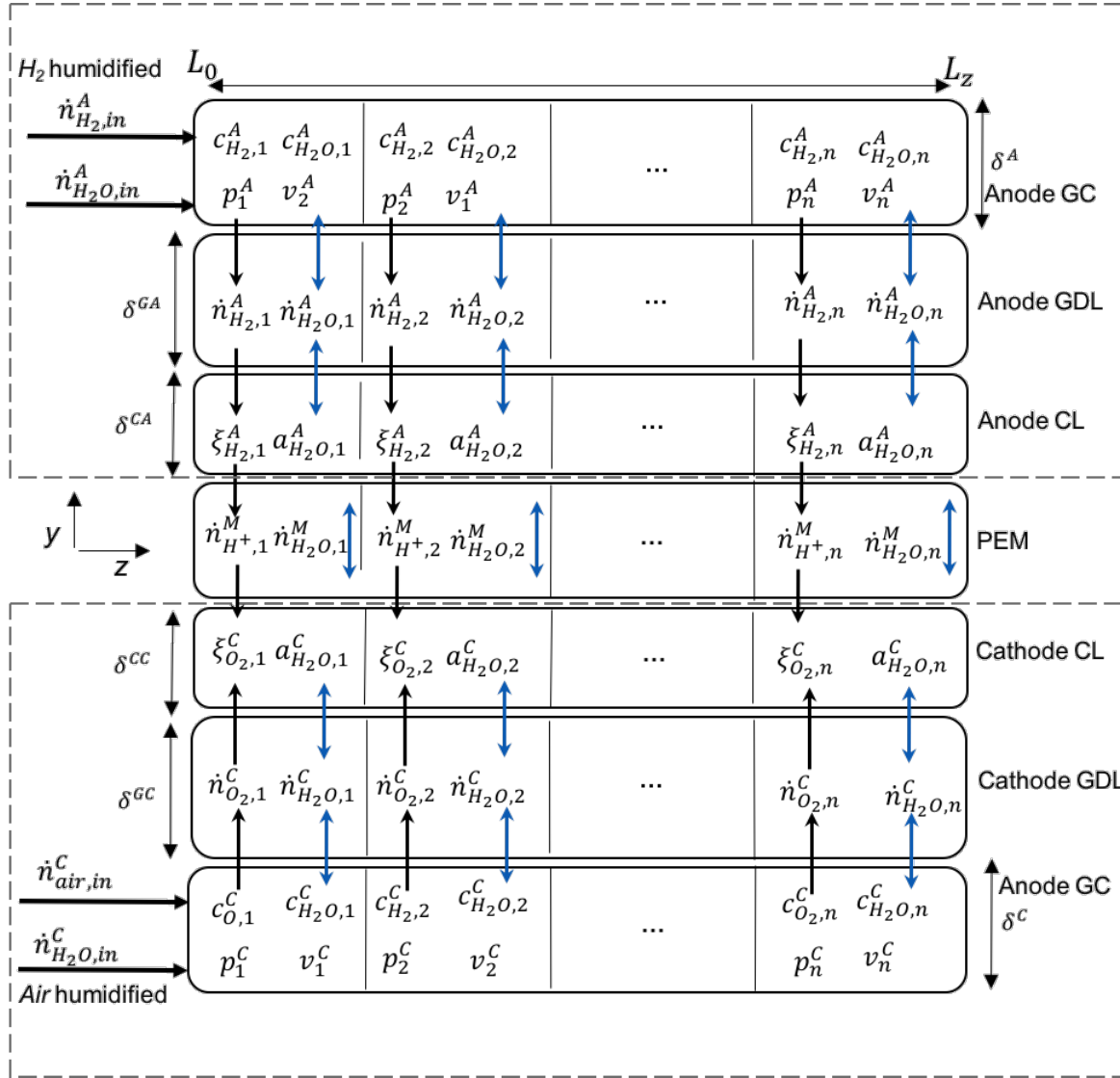
Figure 5.4: Distributed parameter anode and cathode submodel scheme

Note: throughout the previous sections, first principles and empirical model equations have been presented alongside corresponding discretised equations. For simplicity of the text, in the following sections only discretised equations are considered.

5.2.6 Polymer electrolyte membrane (PEM) submodel

A key component of the fuel cell is the polymer electrolyte membrane. This component separates the anode from the cathode and it has several functions. The PEM should prevent electrons and reactant gasses from crossing to the opposite electrode, whilst closing the electrical circuit internally by efficiently transporting protons from the anode to the cathode. In polytetrafluoroethylene (PTFE)-based polymer membranes like Nafion, ions are transported through the polymer membrane by forming hydronium complexes (H_3O^+), which transport the protons in the aqueous phase (Figure 5.1). This type of material has high conductivity and it is the most popular membrane used for PEM fuel cells. The electrical conductivity of Nafion is dependent upon the amount of hydration and can vary with the water content. Hydration can be achieved by humidifying the inlet gases or by relying upon the water generated at the cathode. When Nafion is fully hydrated its conductivity is similar to liquid electrolytes [90].

The water content in the membrane is the ratio of water molecules to the number of charge sites $(SO_3^-H^+)$ and can be expressed as a function of the water vapour activity. The widely used empirical relationships presented by Springer *et al.* [91] for a Nafion 117 membrane are used to determine the water content in the membrane and water transport through the membrane. Water contents at membrane boundaries on the anode side Λ^{AM} and cathode side Λ^{CM} depend on the water activity in the catalyst layers. Calculation is given by sorption isotherms at 80°C,

$$\Lambda_k^{AM} = 0.3 + 12.5 \left(a_{H_2O,k}^A\right) - 16 \left(a_{H_2O,k}^A\right)^2 + 14.1 \left(a_{H_2O,k}^A\right)^3, \tag{5.49}$$

$$\Lambda_k^{CM} = 0.3 + 12.5 \left(a_{H_2O,k}^C\right) - 16 \left(a_{H_2O,k}^C\right)^2 + 14.1 \left(a_{H_2O,k}^C\right)^3. \tag{5.50}$$

Two different methods of water transport in the membrane are considered, electro-osmotic drag and back diffusion.

Electro-osmotic drag flux

As previously explained, water is dragged from the anode to the cathode by protons moving through the membrane. The number of water molecules that accompanies each proton is called electro-osmotic drag (t_W), which is

$$t_W(\Lambda_k) = t_W^{Coeff} \frac{\Lambda_k}{22}, \tag{5.51}$$

where t_W^{Coeff} is the electro-osmotic drag coefficient (usually between 2.5 ± 0.2), and Λ is the water content (which ranges from 0 to 22 water molecules per sulfonate group, and when $\Lambda = 22$, Nafion is fully hydrated). The water drag flux from the anode to the cathode is

$$\dot{n}_{H_2O,k}^{drag} = t_W \left(\Lambda_k\right) \frac{i_k^M}{F}, \tag{5.52}$$

where i_k^M is membrane current density at segment k.

Back diffusion flux

As the reaction at the cathode produces water, it tends to build up on that side, and some water travels back through the membrane. This is known as "back diffusion", and it usually occurs because the amount of water at the cathode is many times greater than at the anode, resulting in a large concentration gradient across the membrane [90]. The water back diffusion flux can be determined by

$$\dot{n}_{H_2O,k}^{back} = -\frac{\rho_{dry}}{M_{mem}} D_w \left(\Lambda_k\right) \frac{d\Lambda_k}{dy}, \tag{5.53}$$

where D_w is the diffusion coefficient expressed as an empirical function of membrane water content for a Nafion 117 membrane, ρ_{dry} is the membrane dry density and M_{mem} is its molecular mass [91],

$$D_w \left(\Lambda_k\right) = D_w^{80} \left(\Lambda_k\right) exp\left[-2640 \left(\frac{1}{T} - \frac{1}{80}\right) \right], \tag{5.54}$$

which is an empirical relation corrected for temperature variations from the value of the diffusion coefficient at 80°C,

$$D_w^{80} \left(\Lambda_k\right) = -0.206465 + 0.0859107 \left(\Lambda_k\right) + 0.00621518 \left(\Lambda_k\right)^2. \tag{5.55}$$

Membrane water content

The protonic conductivity of a polymer membrane is strongly dependent on membrane structure and its water content, as well as membrane fabrication procedures [27]. The water content Λ in the membrane is usually expressed as grams of water per gram of polymer dry weight, or as number of water molecules per sulfonic acid groups present in the polymer, $\Lambda = N(H_2O)/N(SO_3^-H^+)$. In this case, Λ is defined as the ratio between moles of water in the membrane and moles of polymer in the membrane. Considering the model assumptions, the variation of membrane water content is estimated from equations (5.49) and (5.50) as

$$\frac{d\Lambda_k}{dy} = -\frac{\Lambda_k^A - \Lambda_k^C}{\delta^M}, \tag{5.56}$$

where δ^M is the thickness of the membrane.

Net water transport through the membrane

The total amount of water in the membrane is a combination of the electro-osmotic drag and back diffusion,

$$\dot{n}_{H_2O,k}^{M} = \dot{n}_{H_2O,k}^{drag} - \dot{n}_{H_2O,k}^{back}. \tag{5.57}$$

Figure 5.5 illustrates the water transport processes considered in the membrane submodel in detail. The black arrows indicate variable dependency on other variables of the model. The net water flux through the membrane $\dot{n}_{H_2O,k}^{M}$ is divided into the dragged water flux $\dot{n}_{H_2O,k}^{drag}$ and the water back diffusion flux $\dot{n}_{H_2O,k}^{back}$. Important variables from the adjacent submodels (catalyst layers) are included to indicate interaction and dependency. The membrane submodel will also be analysed in Chapter 8 for control design purposes.
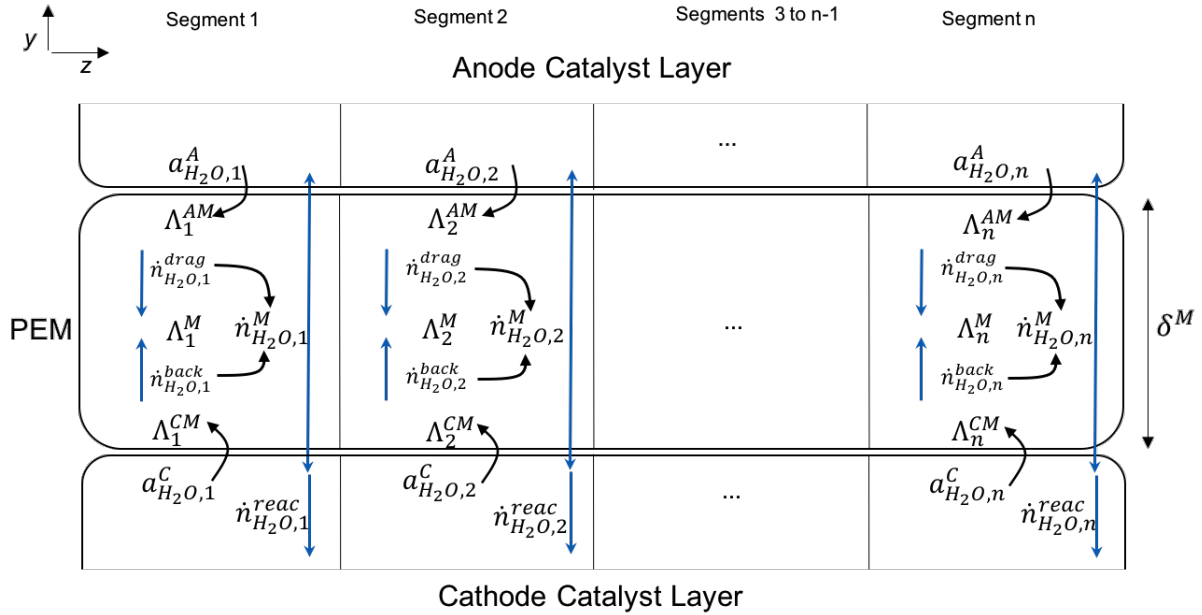
Figure 5.5: PEM submodel water transport scheme

Electrical current density through the membrane

The proton flux through the membrane is driven by gradients of chemical potentials that will be introduced in the following section

$$\dot{n}_{H+,k} = -\frac{\kappa\left(\Lambda_k\right)}{F^2} \bigtriangledown \mu_{H+,k} - \frac{t_W\left(\Lambda_k\right)\kappa\left(\Lambda_k\right)}{F^2} \bigtriangledown \mu_{H_2O,k}, \tag{5.58}$$

where $\kappa\left(\Lambda_k\right)$ is the membrane protonic conductivity as a function of membrane water content Λ [91] in segment k,

$$\kappa\left(\Lambda_k\right) = \kappa_{80}\left(\Lambda_k\right) exp\left[-2640\left(\frac{1}{T} - \frac{1}{80}\right)\right], \tag{5.59}$$

which is an empirical relation corrected for temperature variations from the value of the protonic conductivity at 80°C,

$$\kappa^{80}\left(\Lambda_k\right) = -0.0131556 + 0.00638558\left(\Lambda_k\right) + 0.000167811\left(\Lambda_k\right)^2. \tag{5.60}$$

Electrical current density through the membrane is then related to proton flux by

$$i_k^M = F\dot{n}_{H+,k}, \tag{5.61}$$

in order to quantify the electrical charge.

Gradients of chemical potentials

The water flows through the membrane are assumed to be driven by gradients of chemical potential of water and protons. This is an electrochemical method developed in [13], based on electrochemical potential that arises across a membrane sample exposed at each side to different water activities. Considering that there is no accumulation of protons in the membrane, the gradients of chemical potential are calculated from:

$$\begin{aligned} \bigtriangledown\mu_{H_2O,k} &= \frac{RT_k}{\xi_{H_2O,k}\left(\Lambda_k\right)}\bigtriangledown\xi_{H_2O,k}, \\ \bigtriangledown\mu_{H+,k} &= \frac{RT_k}{\xi_{+,k}\left(\Lambda_k\right)}\bigtriangledown\xi_{H+,k} + F\bigtriangledown\Phi_k, \end{aligned} \tag{5.62}$$

where R is the ideal gas constant. Corresponding gradients are approximated by simple difference formulas,

$$\bigtriangledown\xi_{H2O,k} = \frac{\xi_{H_2O,k}\left(\Lambda_k^{CM}\right) - \xi_{H_2O,k}\left(\Lambda_k^{AM}\right)}{\delta^M}, \tag{5.63}$$

$$\bigtriangledown\xi_{H+,k}^j = \frac{\xi_{H+,k}\left(\Lambda_k^{CM}\right) - \xi_{H+,k}\left(\Lambda_k^{AM}\right)}{\delta^M}, \tag{5.64}$$

$$\bigtriangledown\Phi_k = \frac{\Phi_k^{CM} - \Phi_k^{AM}}{\delta^M}. \tag{5.65}$$

5.2.7   MEA energy balance

Similar to the gas channels energy balance, the energy balance for the MEA parts is:

$$\delta^s \frac{\partial (\rho e)^j}{\partial t} = \sum_{i,j} \dot{n}_i^j h_i \left(T^j \right) + \sum_{j=A,C} \alpha_1 \left(T^j - T \right) + \alpha_2 \left(T^{cool} - T \right) + \lambda^s \delta^s \frac{\partial^2 T^j}{\partial z^2} - \left(\Phi^C - \Phi^A \right) i^M,$$

(5.66)

where h_i denotes enthalpy of gas species and T^{Cool} is the temperature of the coolant flow. The superscript S indicates MEA components. Energy changes are given by the terms on the right hand side of (5.66). This is mass exchange between gas channels and MEA, heat exchange between gas channels and MEA, heat exchange between coolant and MEA, Fourier heat conduction and electrical work. The boundary equations are

$$\frac{\partial T}{\partial z}\Big|_{0,t} = \frac{\partial T}{\partial z}\Big|_{L_z,t} = 0.$$

(5.67)

The total energy relation is defined as internal energy (enthalpies of the different parts of the MEA) and electrical energy. This is

$$\delta^s \left(\rho e \right) = \delta^s \left(\rho u \right) + C^A \delta^{AC} \frac{\Delta \Phi^{A^2}}{2} + C^C \delta^{CC} \frac{\Delta \Phi^{C^2}}{2} = \delta^s \left(\bar{\rho} h \right) (T) + C^A \delta^{AC} \frac{\Delta \Phi^{A^2}}{2} + C^C \delta^{CC} \frac{\Delta \Phi^{C^2}}{2},$$

(5.68)

where,

$$\delta^s \left(\bar{\rho} h \right) (T) = \left(\delta^S - \delta^M \right) (\rho h)^S (T) + \delta^M (\rho h)^M (T) + \delta^M \rho_{H_2O}^M h_{H_2O} (T).$$

(5.69)

In this relation ρ represents corresponding density of MEA components and polymer membrane. Discretised equations are

$$\delta^s \frac{\partial (\rho e)^j}{\partial t} = \sum_{i,j} \dot{n}_i^j h_i \left(T_k^j \right) + \sum_{j=A,C} \alpha_1 \left(T_k^j - T_k \right) + \alpha_2 \left(T_k^{cool} - T_k \right) + \lambda^s \delta^s \frac{T^j}{\Delta z^2} - \left(\Phi_k^C - \Phi_k^A \right) i_k^M,$$

(5.70)

$$\delta^s \left(\rho e_k \right) = \delta^s \left(\rho u_k \right) + C^A \delta_k^{AC} \frac{\Delta \Phi_k^{A^2}}{2} + C^C \delta_k^{CC} \frac{\Delta \Phi_k^{C^2}}{2} = \delta^s \left(\bar{\rho} h \right) (T) + C^A \delta^{AC} \frac{\Delta \Phi^{A^2}}{2} + C^C \delta^{CC} \frac{\Delta \Phi^{C^2}}{2},$$

(5.71)

where

$$\delta^s \left(\bar{\rho} h \right) (T_k) = \left(\delta^S - \delta^M \right) (\rho h)_k^S (T_k) + \delta^M (\rho h_k)^M (T_k) + \delta^M \rho_{H_2O,k}^M h_{H_2O,k} (T_k).$$

(5.72)

5.2.8 Conservation of charge

Current transport is described by governing equations for conservation of charge [13]. Charge balances at the anode and cathode double layers are

$$C^A \delta^{CA} \frac{d\Delta\Phi_k^A}{dt} = i_k^M - 2Fr_k^A, \tag{5.73}$$

$$C^C \delta^{CC} \frac{d\Delta\Phi^C}{dt} = -i_k^M + 2Fr_k^C, \tag{5.74}$$

where δ^{Cj} represents the thickness of the catalyst layers.

5.2.9 Cell current

In actual fuel cell operation, a small number of electrons (relative to the number of protons) is conducted across the membrane, before combining with the protons at the cathode catalyst layer. However, this loss is neglected in this model given the considered fuel cell current range of operation. Therefore, in this model the total cell current is calculated by integrating the membrane current density along the z-direction,

$$I(t) = L_x \left(\sum_k^{L_z} i_k^M \right) L_z, \tag{5.75}$$

where L_x and L_z are the depth and length of the membrane respectively. Theoretical ECSA is given by $L_x L_z$. In this model, a logic was developed to account for liquid water coverage, therefore, the actual total cell current is given by

$$I(t) = ECSA_{app} (L_x L_z) \left(\sum_k^{L_z} i_k^M \right), \tag{5.76}$$

where $ECSA_{app}$ is the proportion of active area not covered by liquid water.

5.2.10 Cell potential

Since cell voltage U is an input, a relation similar to the polarisation curve equation is used to calculate potential drop in the membrane

$$U(t) = \Delta\Phi^C(z,t) - \Delta\Phi^M(z,t) - \Delta\Phi^A(z,t). \tag{5.77}$$

In this relation, activation polarisation losses (energy activation barrier) and ohmic losses (potential drop in the membrane) are considered.

5.3   Model implementation and validation

The set of discretised model equations was implemented and numerically solved with MAT-LAB Simulink using the ODE15s solver for stiff systems and differential-algebraic equations (DAEs). The model is non-linear with 110 states (ODEs) and 310 algebraic variables corresponding to 10 mesh segments. Initial values for each state are determined by a set of initial conditions obtained from the steady-state behaviour of an experimental single PEM fuel cell from Pragma Industries. This cell is available in the fuel cell laboratory of the Robotics and Industrial Informatics Institute, Barcelona, Spain. This is a joint research facility sponsored by the Polytechnic University of Catalonia and the National Spanish Research Council.

The distributed parameter single cell model developed in this chapter has been validated using two approaches. A classic lumped-parameter fuel cell model quantitative validation approach is presented in this section. In this case, physical and empirical parameters of the model were adjusted to meet the specifications of the Pragma fuel cell. Empirical parameters were found using an algorithm that sweeps the range of feasible values in order to minimise the mean square error between model polarisation curve and Pragma cell experimental polarisation curve.

The list of model parameters is found in Appendix A. A polarisation curve was run from 0.15 A cm^{-2} to 1.3 A cm^{-2} in order to compare steady-state behaviour of both the Pragma fuel cell and the model. Table 5.2 indicates simulation parameters and Figure 5.6 shows the results of this validation study.

Table 5.2: Polarisation curve test operating conditions

Variable	Setpoint / Value
Active area (ECSA)	5 cm^2 (theoretical)
H_2 stoichiometry	1.5
O_2 stoichiometry	3
Cell Temperature T	70°C
H_2 inlet RH	50 %
O_2 inlet RH	45 %
Back pressure P	1.01 Bar.a

In this study, overall cell temperature is controlled to a constant value of 70°C. It is assumed that the temperature of the gas channels will converge to the same temperature level of the MEA components T. Throughout the following chapters this parameter T is considered the overall cell temperature.

Notice the polarisation curve for the model only covers the valid range of operation according to assumptions established in section 5.2.1. Comparing both polarisation curves within the range of operation valid for the model, the average absolute current error is 0.053 A. The results indicate that the distributed parameter model gives a good representation of the experimental single PEM fuel cell across a range of steady-state operating points. The
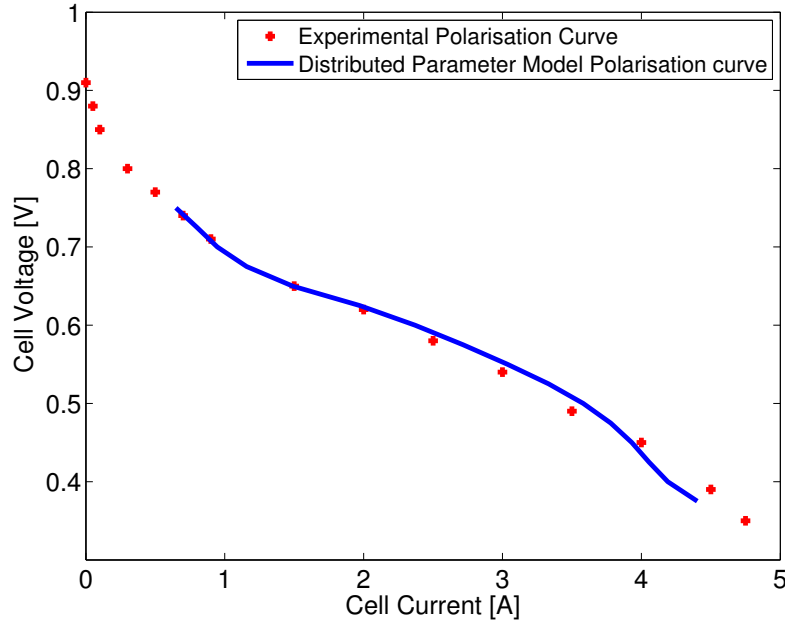
Figure 5.6: Quantitative validation study - Experimental polarisation curve vs. Model polarisation curve

accuracy of the model validates mass and energy balances, as well as the cell voltage model.

Validation of spatial profiles within the PEM fuel cell is a very challenging task, due to the lack of sensors to measure such profiles, or if available, the cost and complexity these sensors add up to the system. Several authors have analysed internal cell behaviour through electrochemical impedance analysis or imaging techniques, which generate important results and conclusions at cell research and development stages [23]. In this work, the second approach used to validate the model consists of a qualitative analysis of the internal spatial profiles of the fuel cell. This approach will be considered in the following chapter, dedicated to analyse transient and steady-state behaviours of internal variables along the z-direction of the cell.

5.4   Conclusions

In this chapter, a distributed parameter model of a PEM fuel cell has been developed. The first sections cover a brief literature review of the most important categories of models in the PEM fuel cell field. The model for this work falls within the single cell range of modelling approaches. The cell components under study include gas channels, gas diffusion layers, catalyst layers, polymer electrolyte membrane and bipolar plates (end plates).

The model is nonlinear with 1+1D dimensions. The 1D dimension (z-direction) was discretised using finite differences. Governing first principles and empirical equations for the processes that occur within the gas channels and the MEA are presented. Mass and

energy balances for the gas channels and MEA were calculated. Well-known electrochemical equations were used to describe the consumption of reactants and generation of products, as well as the cell current and voltage. Empirical equations are used to describe the water transport processes through the membrane.

The model was validated following a quantitative analysis using polarisations curves presented in this chapter. A qualitative validation analysis will be presented in the next chapter. The results show that the distributed parameter model gives a good representation of an experimental Pragma Industries single PEM fuel cell across a range of steady-state operating points. Two publications resulted from this work:

Journal paper

M.L. Sarmiento-Carnevali, M. Serra, C. Batlle, Distributed parameter model simulation tool for PEM fuel cells, International Journal of Hydrogen Energy 39, 4044-4052 (2014).

Conference paper

M.L. Sarmiento-Carnevali, M. Serra, C. Batlle, Distributed parameter model simulation tool for PEM fuel cells, presented at V Congreso Nacional de Pilas de Combustible (CONAP-PICE 2012), November 21-23th, 2012, Madrid, Spain.

The following chapter is dedicated to analyse transient and steady-state behaviours of internal variables along the z-direction of the cell, using the distributed parameter model developed in this chapter. Some of the PEM fuel cell challenges presented in Chapter 3 will be studied under the perspective offered by this model.

Chapter 6

PEM fuel cell analysis with a distributed parameter model

In the previous chapter, a PEM fuel cell distributed parameter model was designed and implemented. A quantitative validation approach using polarisation curves was presented. The results reflected the model accurately represented the steady- state behaviour of a 5-cm^2 single PEM fuel cell from Pragma Industries over a wide range of operating conditions.

In this chapter, a qualitative analysis of cell spatial profiles generated by the model is performed. The aim of this task is to assess the ability and accuracy of the model to simulate steady-state and transient behaviour, along the direction of the gas channels (z), of the variables from different components. In some cases, similarities to results presented in benchmark works available in the literature will be pointed out. In addition, PEM fuel cell challenges introduced in previous chapters will be analysed using the model. Overall, this qualitative study shows the possibilities of the model to perform PEM fuel cell analysis of distributed variables.

6.1   Distributed parameter model

Figure 6.1 illustrates the distributed parameter model developed in Chapter 5. The model under study is a single-channel single PEM fuel cell that consists of gas channels (GCs), gas diffusion layers (GDLs), catalytic electrodes (CLs), the polymer electrolyte membrane (PEM), current collector plates (end plates) and a liquid cooling system. There are 6 inputs to the cell: the voltage U, according to a certain duty cycle, the cooling temperature input, the hydrogen inlet flux $\dot{n}_{H_2,in}^A$ and the anode water inlet flux $\dot{n}_{H_2O,in}^A$, the oxygen/nitrogen inlet flux $\dot{n}_{air,in}^C$ and the cathode water inlet flux $\dot{n}_{H_2O,in}^C$. The measured outputs are the cell current I and temperature T. The model is non-linear with dimension 1 + 1D, which considers transport through the MEA as a series of lumped parameter models, i.e. one single volume for each layer of the cell in the y-direction, coupled to 1D models in the direction

of the gas flows, i.e. spatial gradients in the z-direction of each layer of the cell. The 1D direction has been discretised in n segments using the central finite differences approach. Some model variables are shown in the scheme. These variables have spatial profiles along the z-direction. Detailed information of the model development, implementation, variables and parameters can be found in Chapter 5.
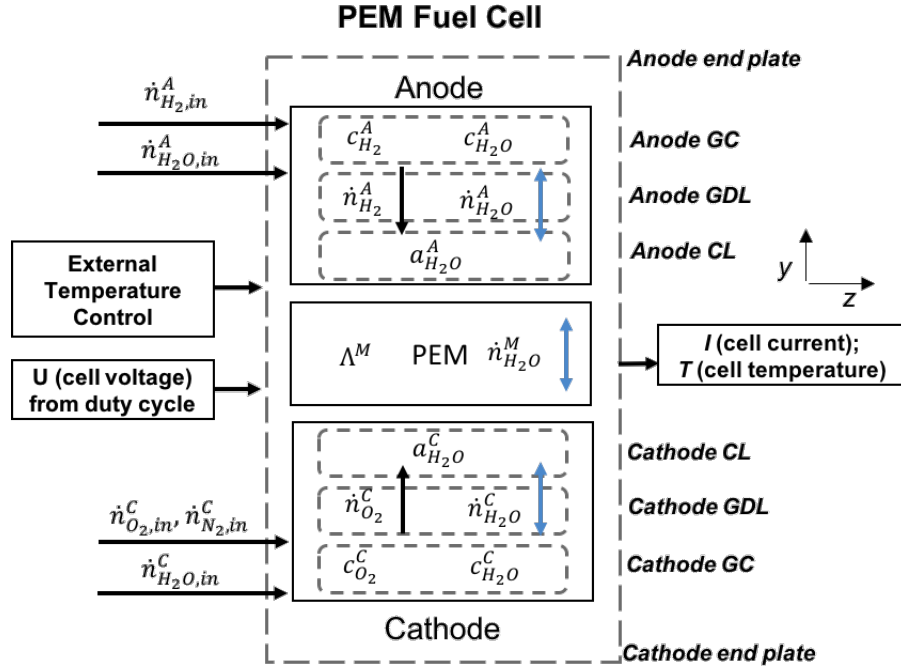
PEM Fuel Cell

Figure 6.1: Distributed parameter PEM fuel cell model scheme (simplified)

6.2 Steady-state analysis of model variables

The steady-state results of some important fuel cell variables considered in the model are presented in this section. Spatial variations along the directions of the gas channels (z) are considered. The scenario under analysis falls within the ohmic region of the model polarisation curve (Section 5.3 in Chapter 5). Table 6.1 presents corresponding operating conditions.

6.2.1 Concentration of gases, pressure and velocity in the gas channels

Spatial profiles of the concentration of gases in the anode and cathode gas channels, anode and cathode pressure and flow velocity are presented in Figure 6.2. Concentrations of reactants are higher at the beginning of the channels, which correspond to the area of higher gas pressure on both anode and cathode. Concentration of oxygen is lower than concentration of hydrogen due the presence of nitrogen in the cathode gas stream.

Table 6.1: Steady-state operating conditions

Variable	Setpoint
H_2 stoichiometry	1.5
O_2 stoichiometry	3
H_2 inlet RH	50 %
O_2 inlet RH	45 %
I Cell current	1.4545 A
U Cell voltage	0.65 V
Back pressure P	1.01 Bar.a

The results clearly show important spatial profile variations. Concentration of water increases towards the outlet end of the anode gas channel due to the consumption of hydrogen and back diffusion effect. On the cathode side, water concentration increases towards the outlet end of the channel due to generation of water by the corresponding electrochemical reaction, the consumption of oxygen and the electro-osmotic drag effect.

(a) H_2 and H_2O concentration $\left(c_{H_2}^A, c_{H_2O}^A\right)$ (b) O_2, N_2, H_2O concentrations $\left(c_{O_2}^C, c_{N_2}^C, c_{H_2O}^C\right)$

(c) Anode pressure, cathode pressure (p^A, p^C) (d) Anode and cathode flow velocity (v^A, v^C)
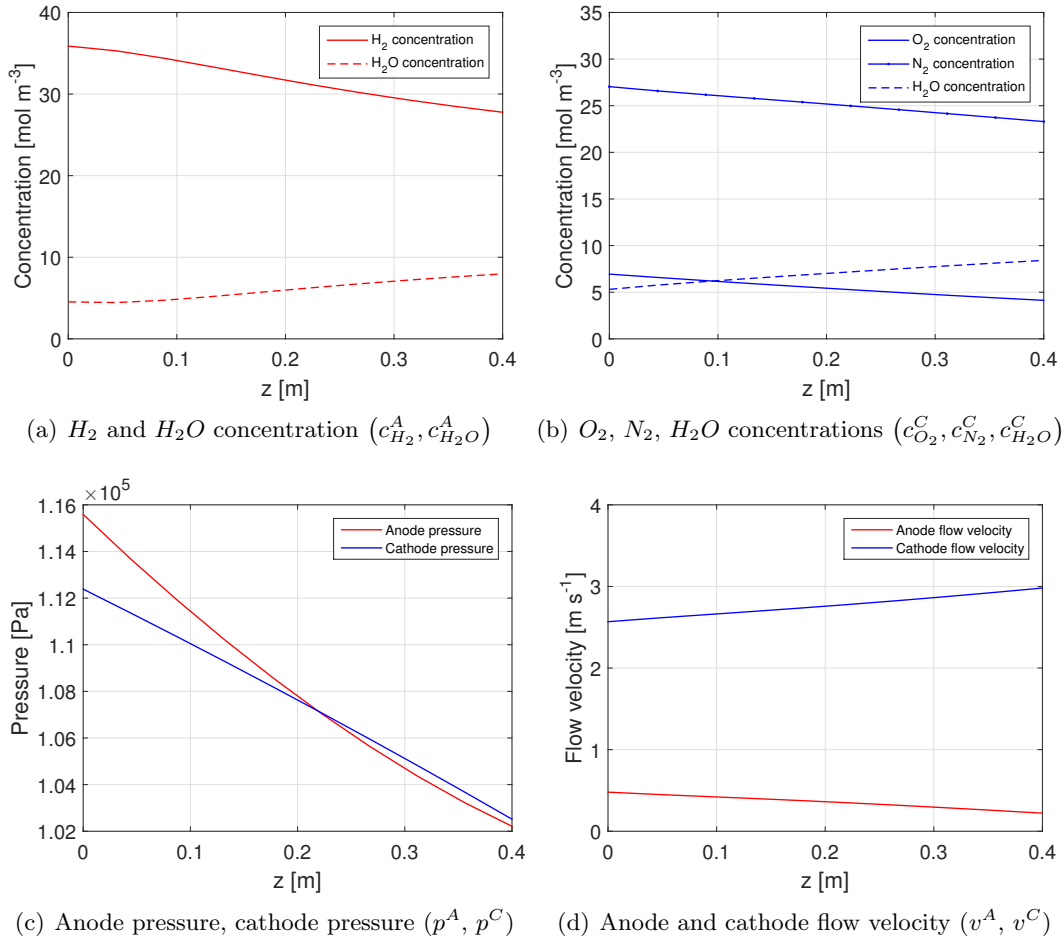
Figure 6.2: Spatial profile of anode and cathode pressure, flow velocity and reactants concentration along the z-direction

Therefore, water partial pressure increases in this region of the cathode with higher possibility of liquid water formation. This effect will be noted in further sections. The velocity in both gas channels changes due to the consumption of reactants and generation of water. Pressure in the anode and cathode are quite similar due to the combination of reaction rates and stoichiometries, and decreases towards the channel outlet as the concentrations of reactants decrease.

Spatial variation of the reactant concentrations observed along the channels should be taken into account in the design of control strategies for the supply of gases. Degradation phenomena such as carbon corrosion, as seen in section 3.1.1, is highly enhanced by extremely non-uniform spatial profiles and starvation of reactants. The channel outlet is particularly a critical area. A supply strategy using high stoichiometries of reactants will help to reduce the possibility of starvation in this region, but the efficiency and net power of the fuel cell may be compromised. High stoichiometries cause higher losses of hydrogen and excess of air into the cathode requires higher effort from the air supply system (compressor), resulting in higher parasitic losses.

6.2.2   Reactant fluxes along the gas channels

Figure 6.3 shows the spatial profile of reactant convective fluxes along the z-direction. This is the horizontal flux of reactants from the inlet to the outlet ends of the channels represented by the product $c_{H_2}^A v^A$ (concentration multiplied by velocity) for the anode channel and $c_{O_2}^C v^C$ for the cathode channel.

(a) H_2 flow $\left(c_{H_2}^A v^A\right)$ (b) O_2 flow $\left(c_{O_2}^C v^C\right)$
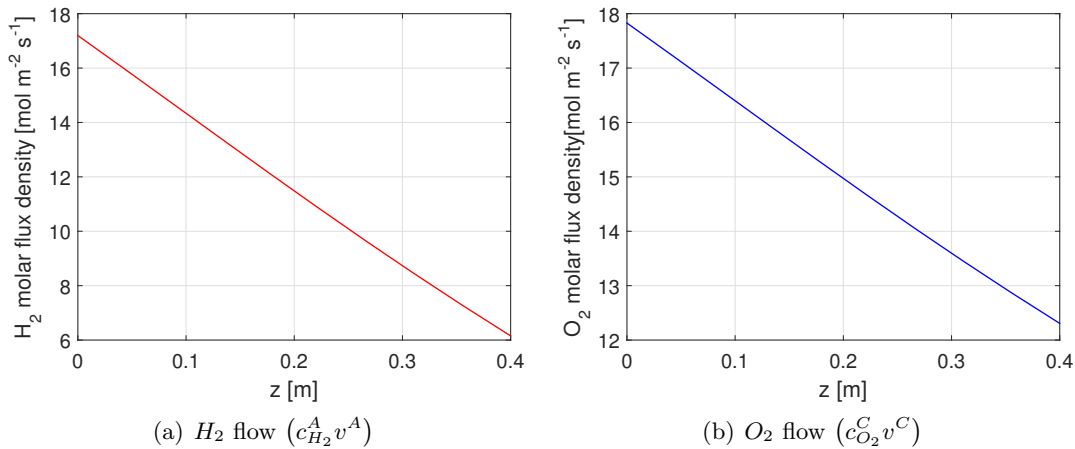
Figure 6.3: Spatial profile of reactant fluxes along the corresponding gas channels

As expected, the fluxes are higher towards the channel inlet and decrease along the z-direction as the hydrogen and oxygen are consumed. The anode reaction consumes hydrogen at twice the rate that the cathode reaction consumes oxygen. In this scenario, the stoichiometry values compensate the difference in reaction rates. A stoichiometry value of 1.5 for hydrogen and 3 for oxygen will cause the inlet flux density of both reactants to be

equal. Detailed information on hydrogen and oxygen consumption rates by the corresponding electrochemical equations can be found in Chapter 2. Equations (6.1) and (6.2) briefly describe this situation,

$$n_{H_2} = \frac{3}{2}\left(\frac{I}{2F}\right),\tag{6.1}$$

$$n_{O_2} = 3\left(\frac{I}{4F}\right) = \frac{3}{2}\left(\frac{I}{2F}\right),\tag{6.2}$$

where n_{H_2} and n_{O_2} are inlet flux rates of hydrogen and oxygen. The values $\frac{3}{2}$ and 3 represent corresponding stoichiometries. The electrochemical consumption of hydrogen and oxygen is given by $\frac{I}{2F}$ and $\frac{I}{4F}$ respectively. Note that these values are not flux densities but fluxes.

The stoichiometry values can be confirmed from Figure 6.3. Towards the end of the anode gas channel, the hydrogen flux has decreased around 2/3 of the total flow at the inlet. This agrees with a hydrogen stoichiometry value of 1.5. On the cathode side, towards the outlet end of the gas channel the oxygen flux has decreased around 1/3 of the total value available at the inlet. This agrees with an oxygen stoichiometry value of 3. Overall, the results presented in the current and previous sections qualitatively validate the mass balances in the gas channels along the z-direction. Similar behaviour of some of these variables was reported in [30, 42].

6.2.3 Water fluxes along the gas channels

Figure 6.4 shows the spatial profile of water convective fluxes along the z-direction. As in the previous section, this is the horizontal (according to Figure 6.1) flux of water from the inlet to the outlet ends of the channels represented by the product $c_{H_2O}^A v^A$ (concentration multiplied by velocity) for the anode channel and $c_{H_2O}^C v^C$ for the cathode channel.

(a) H_2 horizontal flux anode $\left(c_{H_2O}^A v^A\right)$ (b) H_2O horizontal flux cathode $\left(c_{H_2O}^C v^C\right)$
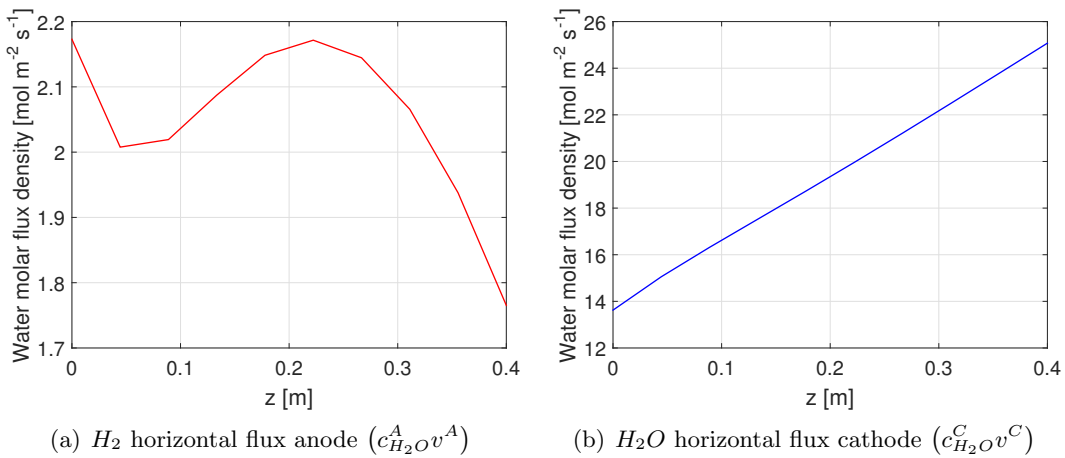
Figure 6.4: Spatial profile of water fluxes along the corresponding gas channels

Interesting results can be analysed from this figure. Figure 6.4(a) presents the horizontal water flux density in the anode. The flux tends to decrease towards the outlet end of the gas channel. This behaviour is expected in cases where the electro-osmotic drag effect surpasses the back diffusion. In addition, this situation occurs at lower current densities, which is the case in this scenario. As seen in previous sections the water concentration on the anode gas channel increases, due to the consumption of hydrogen, but the horizontal flux density of the anode has a net result of decreasing water.

Figure 6.4(a) also reveals an issue introduced in Chapter 3 regarding water management. At the inlet side of the anode gas channel the electro-osmotic force is stronger. Depending on the cell current, this effect causes a drop in the water flux density that is clearly seen in this figure. The issue is also slightly noted in the spatial profile of concentration of water in the anode (Figure 6.2(a)), although it does not cause a major drop in water concentration due to the higher consumption of hydrogen in this area (as will be seen in the following section).

The issue in discussion can cause local dryness in the anode GDL, anode catalyst layer and polymer electrolyte membrane, with considerable fuel cell degradation consequences as explained in Chapter 3. The magnitude of this problem depends on the combination of variables such as inlet hydrogen gas humidification, electro-osmotic drag flux and current density. A few modelling works in the literature have also reported this condition [26, 101, 52].

Figure 6.4(b) shows the horizontal flux density of water on the cathode gas channel. As expected, the water flux in the cathode increases considerably towards the outlet end of the channel due to the generation of water by the cathode electrochemical reaction, as well as the electro-osmotic drag effect. Moreover, liquid water dragged by high air flow rates tends to accumulate in this region making it more vulnerable to issues such as local flooding.

In summary, the results presented in Figure 6.4 demonstrate the importance of internal spatial profiles for control actions in water management strategies. These results will be considered and widely discussed in Chapter 8.

6.2.4   Reactant fluxes from the gas channels to the catalyst layers

Figure 6.5 presents the reactant flux densities from the gas channels, through the GDL, towards the catalyst layer (vertical fluxes indicated by black arrows in Figure 6.1). These flux densities represent the consumption of reactants in anode and cathode catalyst layers and depend on corresponding electrochemical reactions. Figure 6.5(a) confirms the model ability to calculate the rate of hydrogen consumption along the anode catalyst layer and the rate of oxygen consumption in the cathode catalyst layer (shown in Figure 6.5(b)). The flux density of oxygen consumption is half the flux density of hydrogen consumption, according to corresponding electrochemical reactions.

As expected, higher reactant consumption rates can be noted towards the left side of the

catalyst layers, where concentrations of reactants in the gas channels and electrochemical reaction rates are higher (inlet flow side). Both flux densities of the anode and cathode have positive signs, due to the assumption that positive values indicate the flux moves from the corresponding gas channels to the membrane. These results agree with the spatial profile behaviour of variables analysed in the previous sections.

(a) H_2 flux $\left(\dot{n}_{H_2}^A\right)$ (b) O_2 flux $\left(\dot{n}_{O_2}^C\right)$
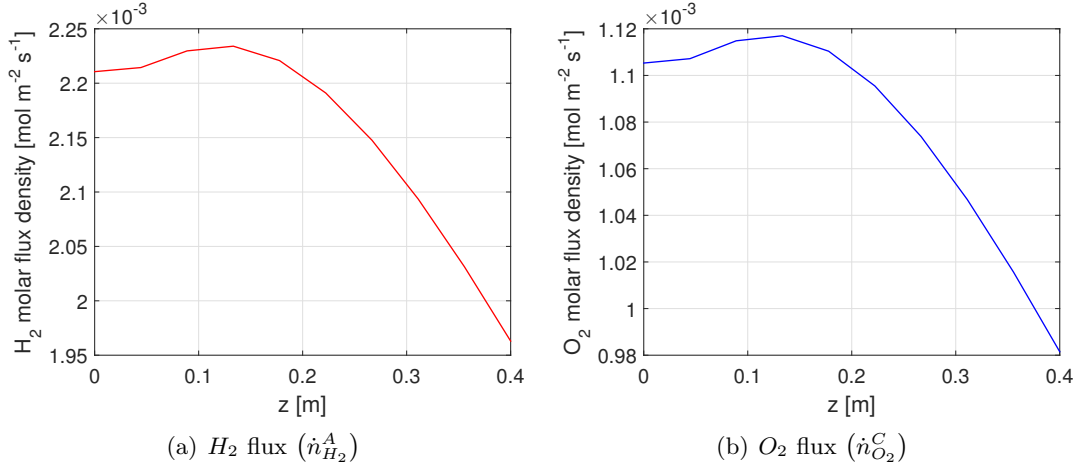
Figure 6.5: Reactant fluxes from the anode and cathode gas channels to the catalyst layers (profile along the z-direction)

6.2.5 Water vapour activity in the catalyst layers

Water vapour activity, or water activity, in the catalyst layers, along with membrane water content (Section 6.2.10), are the key variables in the design of PEM fuel cell water management strategies. As indicated in Chapter 5, water activity is given by the partial pressure of water on the catalyst layers, divided by the saturation pressure of water that depends on the overall temperature of the fuel cell (T). Figure 6.6 shows spatial profiles of water activity, along the z-direction, for anode and cathode catalyst layers.

The values of the water activity range from 0 to 1. Values closer to 0 indicate dryness in the catalyst layer-membrane boundaries and a value of 1 represents condensation or liquid water formation. As seen in Figure 6.6, in the current scenario, water condensation is not present. Notice that, as expected, water activity in both anode and cathode catalyst layers is higher towards the right side. This result agrees with the behaviour of concentration of gases in the gas channels (Figure 6.2). Due to the consumption of hydrogen and oxygen, concentration of water increases towards this side of the catalyst layer.

Another result in this image, which is important to confirm that the model properly represents the behaviour inside a PEM fuel cell, is the difference between cathode water activity and anode water activity. As expected, the water activity in the cathode catalyst layer is higher than the water activity in the anode catalyst layer. As analysed in previous

chapters, the cathode is more vulnerable to accumulation of liquid water in its catalyst layer and other backing layers since it is the water generating electrode. Liquid water accumulation is not analysed in this section, but will be discussed in further sections.

Excess of liquid water in the gas channels, gas diffusion layers and catalyst layers can impede the reactants to access the active reaction platinum sites. These results already demonstrate the importance of considering the behaviour of spatial profiles of water activity in water management control strategies. The water activity on the right side of the catalyst layers along the z-direction can be quite different from the value on the left side. Conditions like flooding and drying could simultaneously occur, and water management decisions based on lumped-parameter indicators can lead to inadequate operation control actions that result in loss of performance and degradation of the fuel cell.
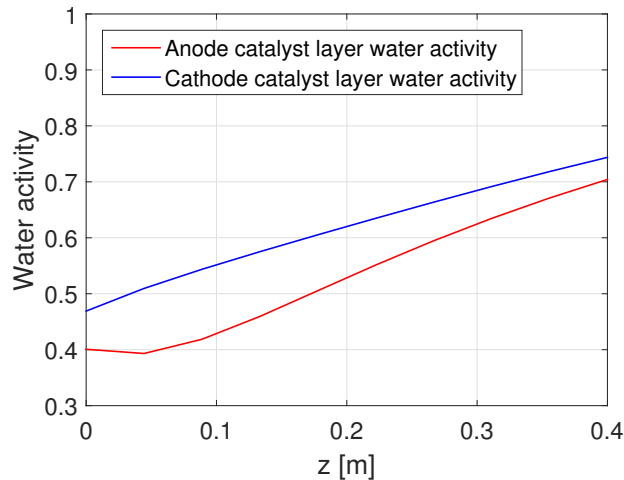
Figure 6.6: Spatial profile of water activity in the catalyst layers along the z-direction

6.2.6   Membrane current density

Figure 6.7 shows the membrane current density spatial profile along the z-direction. Increased current density values are seen towards the left side of the membrane, where hydrogen and oxygen concentrations and partial pressures are higher. Notice that the current density spatial profile has the same curve shape in comparison to the spatial profiles of the hydrogen and oxygen consumption flux densities (Figure 6.5). This result is very important to confirm the accuracy of the entire PEM fuel cell model and the proper interconnection of the GDLs, catalyst layers and polymer electrolyte membrane submodels. Some authors have also reported the behaviour noted in this image [36].

The current density has a peak value around the first quarter section of the membrane, not on its leftmost side. This is also an important spatial aspect for the development of inlet gas humidification control strategies. During this first section, the membrane is still not properly humidified and the electro-osmotic drag effect tends to dry its anode

side (Figure 6.3(a)), as well as the boundary area with the corresponding catalyst layer, causing protonic conductivity to be lower in this left part along the z-direction. Towards the last (right) sections of the polymer membrane, the current density decreases due to less consumption of gases and reduction in the hydrogen and oxygen partial pressure.
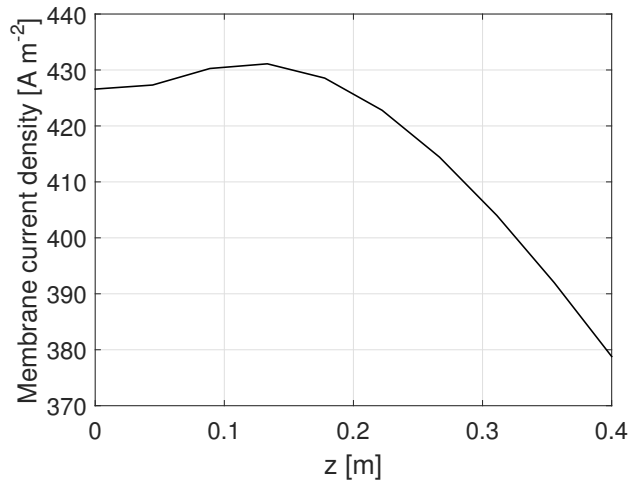
Figure 6.7: Membrane current density spatial profile along the z-direction

6.2.7 Voltage losses

As previously indicated, this model takes into account anode and cathode activation polarisation losses, as well as ohmic losses. The ohmic resistance of the cell is caused only by the membrane. Fuel and electrons crossover losses and mass transport losses, due to current densities close to the limiting current, are not considered. However, the logic presented in Section 5.2.5 is used to estimate concentration losses due to the presence of liquid water in the cell. Moreover, the model is only run in the ohmic region of the polarisation curve, which is considered normal operation of the experimental fuel cell used in the model validation stage. Figure 6.8 presents activation polarisation losses in the anode and cathode.

As expected, the activation polarisation losses are quite uniform along the z-direction. These results agree with the theory, as the operating conditions under analysis fall within the ohmic region of the polarisation curve, where these losses are not predominant. Figure 6.9 shows the voltage losses due to membrane ohmic resistance. The behaviour of this curve agrees with the theory. Increased ohmic losses are seen in the same region of higher current densities. The ohmic losses are predominant in the case scenario under analysis. Other authors have reported similar results [46].

6.2.8 Water generated in the cathode catalyst layer

Figure 6.10 shows the flux of water generated from the electrochemical reaction on the cathode. As expected, the curve shape of this flux is similar to the shape of the current
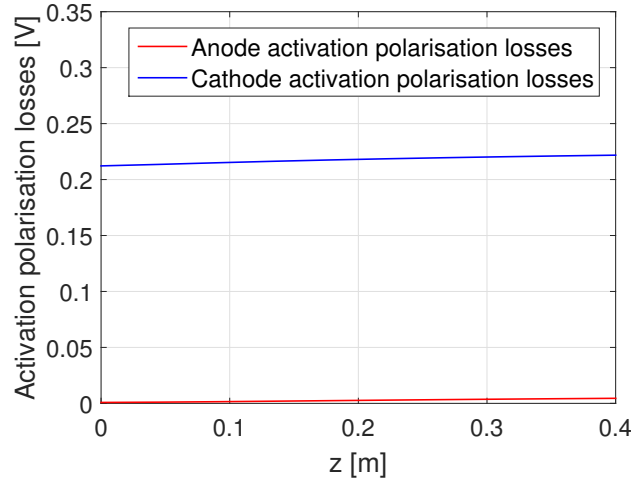
Figure 6.8: Spatial profile along the z-direction of anode and cathode activation polarisation losses
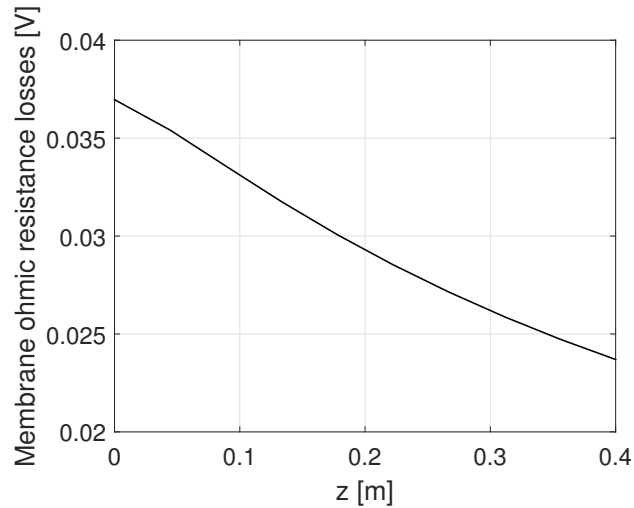
Figure 6.9: Ohmic losses spatial profile along the z-direction

density curve and the ones for the consumption of reactants. This means more water is generated around the area where the current density is higher. The amount of generated water confirms the accuracy of the electrochemical submodel, as it is twice the magnitude of the oxygen consumption.

Accumulation of water around the right end of the catalyst layer, along with higher water partial pressure on this side, as seen in the water activity analysis of Section 6.2.5, can cause undesirable operating issues such as cell flooding, which is likely to occur in the cathode side. This condition reveals the need for advanced control strategies that can monitor the behaviour of the spatial profile of water in the cathode, and also in the anode, to base the decisions of corresponding fuel cell control strategies on this information. A control approach with this feature could manage the humidification of the electrolyte membrane

and catalyst layers taking full advantage of the water processes that occur in the fuel cell.
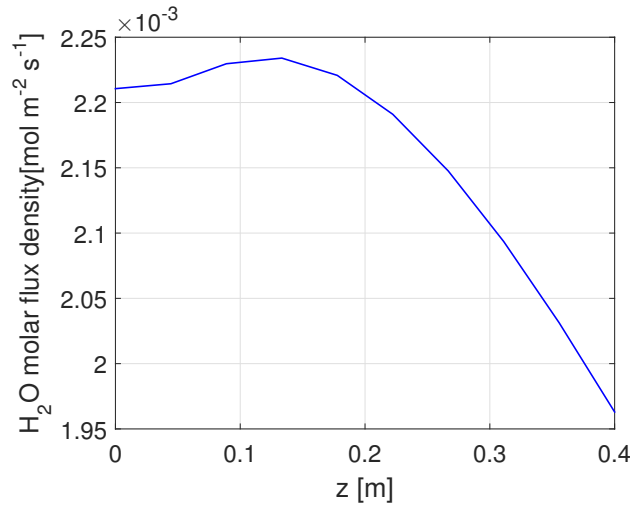
Figure 6.10: Spatial profile of water generated in the cathode catalyst layer along the z-direction

6.2.9   Water fluxes through the membrane

Figure 6.11 shows spatial variations along the z-direction of the different water fluxes through the membrane for the scenario under analysis. This figure presents very interesting results since the water transport through the membrane is a key aspect of the fuel cell performance. Two different fluxes through the membrane are shown in the figure, electro-osmotic drag and back-diffusion. As previously explained, the electro-osmotic flux is the amount of water dragged by the protons travelling through the membrane in the form of hydronium complexes (H_3O^+). The back diffusion flux if the amount of water that travels back from the cathode to the anode due to the gradient of water concentration across the membrane.

As expected, the electro-osmotic drag flux is higher towards the left side of the membrane, due to higher electrochemical reaction rates on this same side in the anode catalyst layer. As indicated in Chapter 5, this flux depends on the current density and membrane protonic conductivity, which is a function of membrane water content (Section 6.2.10). Therefore, the curve of the electro-osmotic drag has a different shape in comparison to the current density curve shape. The effect of the current density curve shape certainly dominates the spatial profile of this flux, however it is not as steep towards the right side of the membrane, as is the current density profile. This variation is caused by increased protonic conductivity on the right side of the membrane, due to higher water content in that region as will be seen in the following section.

The spatial profile of the back diffusion flux has also a behaviour according to the variables analysed in the previous sections. This flux increases towards the right end of the

membrane on the cathode side, where water concentration and, therefore, partial pressure are higher. Increased water partial pressure is caused mainly by the generation of water from the cathode electrochemical reaction, the electro-osmotic drag effect and the decreasing concentration of oxygen as it is consumed in the reaction. In this section of the cathode side of the membrane, water tends to build up and create a concentration gradient across the membrane causing the back diffusion flux to be higher. In this particular scenario under analysis the electro-osmotic drag flux surpasses the back diffusion flux.
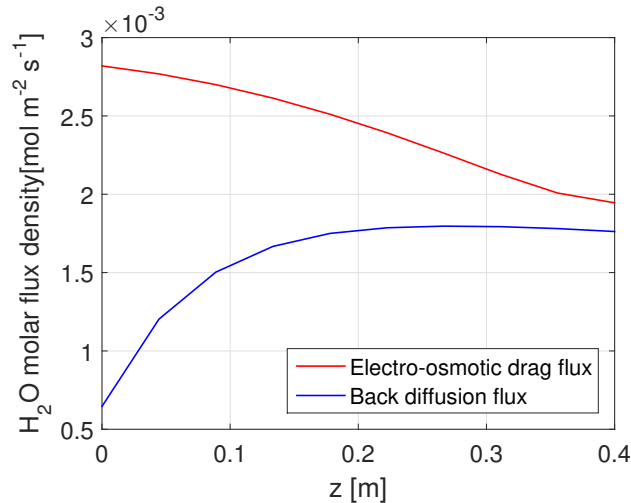
Figure 6.11: Spatial profile of water fluxes through the membrane along the z-direction

6.2.10   Membrane water content

Figure 6.12 presents the spatial profile of water content in the polymer electrolyte membrane. As expected, the water content is higher towards the right side of the membrane in the z-direction. This result agrees with the behaviour analysed in previous sections. The water content in the polymer electrolyte membrane depends on different aspects. First, it depends on the water transport through the membrane, this is the electro-osmotic drag and the back-diffusion fluxes discussed in Section 6.2.9.

In the region where the electro-osmotic drag is higher, due to the shape of the current density curve, the temperature of the cell (Section 6.2.11) is also higher. This condition contributes to evaporation of water with a tendency to dry the membrane. Finally, the water content strongly depends on the water activities of neighbouring catalyst layers, which are higher towards the right side of the membrane in the z-direction during normal cell operation. The effect of the water activities clearly dominates the shape of the water content curve.
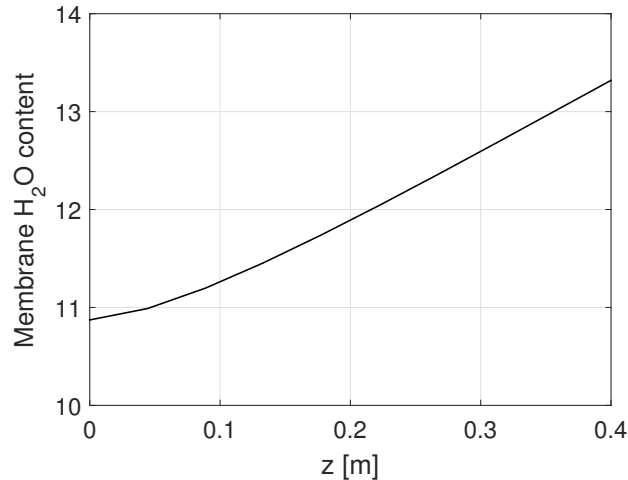
Figure 6.12: Membrane water content spatial profile along the z-direction

6.2.11 Cell temperature

Figure 6.13 shows the spatial profile of the fuel cell temperature T. As expected, temperature is higher around the same region where current density is higher since the overall reaction of a PEM fuel cell is an exothermic process. Water and heat are the fuel cell by-products, therefore, the shapes of the curve of generated water in the cathode catalyst layer and the temperature of the cell are quite similar. Overall, this result agrees with the spatial profile behaviour of several variables analysed in the previous sections.

As seen in the figure, spatial variations of temperature in the cell are important. Local over-heating of the cell can lead to degradation mechanisms such as thermal stress or material fractures in certain components. Therefore, the spatial profile of temperature should be taken into account for thermal management control strategies. Advanced control strategies with this feature could keep the temperature profile under analysis to avoid local issues by providing the correct control actions. A few authors have also reported this spatial behaviour of the cell temperature [42, 26].

6.3 Steady-state analysis of water management challenges

Some of the most relevant problems related to the performance and degradation of PEM fuel cells were previously described in Chapter 3. It has already been stated that many PEM fuel cell problems highlight the importance of taking internal spatial variations of some cell variables into account. In this section, a set of these issues related to water management are analysed using the benefits of the distributed parameter model presented in Chapter 5 and analysed in Section 6.2, in order to understand the problems in terms of the behaviour along the z-direction.

This study is focused on the water activities in the anode and cathode catalyst layers.
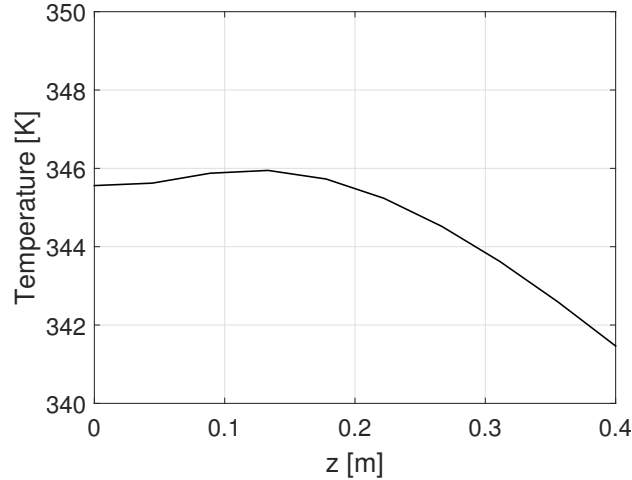
Figure 6.13: PEM fuel cell temperature along the z-direction

The key objective of this analysis is to recreate, via simulations, the operating conditions that result in liquid water formation within the anode and cathode sides of the polymer electrolyte membrane, as well as situations that cause the anode to lose inlet gas humidification resulting in dryness that also affects the membrane protonic conductivity and durability. An analysis of available variables suitable to control the water activity in the anode and cathode is also performed, in order to establish the different issues as control problems.

6.3.1   Analysis of water activities under a high current density scenario

In this section, a high current density scenario is considered. Fixed simulation parameters are specified in Table 6.2. Figure 6.14 shows the spatial profile of water activity in the anode and cathode catalyst layers along the z-direction. The figures on the left side show results for anode water activity under various operating conditions. Likewise, figures on the right side show results for the cathode water activity under similar operating conditions. In general, this figure presents the effect of different values of hydrogen and oxygen stoichiometry and inlet gas relative humidity on the spatial behaviour of the water activity.

Table 6.2: Operating conditions - High current density scenario

Variable	Symbol	Setpoint
Cell temperature	T	344 K
Cell current density	i	0.6 - 0.7 A cm^{-2}
Cell current	I	3 - 3.5 A
Cell voltage	U	0.5 V

Figures 6.14(a) and 6.14(b) show the results for a scenario where the inlet gas relative humidity is fixed at 10% for both hydrogen and air. For this fixed condition, different values of hydrogen and oxygen stoichiometry are presented. In the anode catalyst layer the

effect of the electro-osmotic drag force on the side of the catalyst layer, parallel to the gas inlet side of the corresponding gas channel, is clearly noted. As seen in previous sections, there is a tendency to dryness in this area. Since the relative humidity of the inlet gases is low, dryness is noted on this side of the anode catalyst layer. Highly non-uniform spatial variations are noticeable in this image. The behaviour of the left side of the catalyst layer, along the z-direction, considerably differs from that seen in the right side.

In Figure 6.14(a) the effect of different levels of hydrogen stoichiometry are also seen. In the first section of the anode catalyst layer along the z-direction, higher stoichiometries help to reduce the drying effect of the electro-osmotic drag forces, due to an increased amount of humidification present in this area, which is necessary to maintain the fixed inlet hydrogen relative humidity. However, this effect is not enough to avoid the situation of dryness. On the opposite site of the anode catalyst layer, condensation is only seen for a hydrogen stoichiometry value of 1.

Figure 6.14(a) also shows how the stoichiometry variable could be used to reduce the rate of liquid water formation in the cell. However, the results in this figure show the importance of a controller that optimises the combined use of the humidification and stoichiometry of reactants, taking into account spatial variations to control the water activity profile. A poor combination of these two variables will lead to undesirable operating conditions such as a dry anode. Morever, the use of hydrogen stoichiometries higher than 1 compromises the efficiency of the fuel cell if the gas is not recirculated.

Figure 6.14(b) clearly shows the self-humidifying behaviour of the cathode. Condensation is seen towards the right side of the catalyst layer where the partial pressure of water is higher. The effect of oxygen stoichiometry on the partial pressure of water is clear. This result also indicates how the stoichiometry variable could be used, in combination with the inlet gas relative humidity, to reduce the rate of condensation. However, increased use of this variable leads to larger parasitic losses. Therefore, a controller that manages the actions of these two variables combined should: (i) consider the cost-benefit behaviour of such variables and (ii) take into account spatial profiles, in order to understand the entire situation of the water activity in the catalyst layer.

Figures 6.14(c) and 6.14(d) show the results for a scenario where the inlet gas relative humidity is fixed at 25% for both hydrogen and air. The behaviour of the water activity spatial profiles for both anode and cathode catalyst layers is quite similar to that seen in the figures previously analysed. The effect of higher inlet gas relative humidity is noted. The condition of dryness on the left side of the anode catalyst layer is less severe but still present. Previous comments apply to the behaviour of the spatial profile of the water activity in the cathode catalyst layer.

Figures 6.14(e) and 6.14(f) show the results for a scenario where the inlet gas relative humidity is fixed at 50% for both hydrogen and air. The effect of higher inlet gas relative humidity is seen. The water activity spatial profiles of both anode and cathode catalyst

(a) 10% H_2 RH

(b) 10% Air RH

(c) 25% H_2 RH

(d) 25% Air RH

(e) 50% H_2 RH

(f) 50% Air RH

(g) 75% H_2 RH

(h) 75% Air RH

Figure 6.14: Spatial profile of water activity in the anode and cathode catalyst layers along the z-direction under a high current density scenario

layers present healthier values. The condition of dryness on the left side of the anode catalyst layer is not severe anymore but the tendency to this behaviour is still present given the high current density operating condition. The possibilities of condensation in the anode catalyst layer are now higher due to increased inlet hydrogen relative humidity. The spatial profile of the water activity in the cathode catalyst layer shows clear signs of inlet gas over-humidification, as condensation is seen in a larger part of the layer along the z-direction.

Figures 6.14(g) and 6.14(h) show the results for a scenario where the inlet gas relative humidity is fixed at 75% for both hydrogen and air. The effect of inlet gas over-humidification in the water activity spatial behaviour of both catalyst layers is seen. The water activity spatial profiles of both anode and cathode catalyst layers show condensation along the entire z-direction. Tendency to dryness on the anode catalyst layer is less noticeable.

In this study, the current density values range from 0.6 A cm^{-2} to 0.7 A cm^{-2} due to the impact of dryness on the protonic conductivity of the polymer electrolyte membrane, and the effects of accumulated liquid water on the ECSA, as modelled in Chapter 5. These effects will be analysed in detail in Chapter 8. In summary, Figure 6.14 has demonstrated the importance of spatial variations along the z-direction of the water activity in the anode and cathode catalyst layers.

The effect of potential control variables has also been evaluated. This study and the results presented in the following sections are the first steps towards the design of a distributed parameter model-based control strategy for the water activity in the anode and cathode catalyst layers. This strategy will consider the inlet gas humidification inputs and the reactant stoichiometry inputs as manipulated variables. It is clear that an optimal combination of these variables can lead to healthy water activity values and reduce the rate of condensation when possible. The limitations and effects of these variables learned from this analysis will be taken into account for the development of control strategies in Chapter 8.

6.3.2 Analysis of water activities under a low current density scenario

In this section, a low current density scenario is considered. Fixed simulation parameters are specified in Table 6.3. Figure 6.15 shows the spatial profile of water activity in the anode and cathode catalyst layers along the z-direction. As in the previous section, the figures on the left side show results for anode water activity under various operating conditions and figures on the right side show results for the cathode water activity under similar operating conditions. In general, this figure presents the effect of different values of hydrogen and oxygen stoichiometry and inlet gas relative humidity on the spatial behaviour of the water activity.

Figure 6.15 show the results for situations where the inlet gas relative humidity is fixed at 10%, 25%, 50% and 75% for both hydrogen and air. Under these fixed conditions, different

Table 6.3: Operating conditions - Low current density scenario

Variable	Symbol	Setpoint
Cell temperature	T	344 K
Cell current density	i	0.1 - 0.2 A cm^{-2}
Cell current	I	0.5 - 0.98 A
Cell voltage	U	0.75 V

values of hydrogen and oxygen stoichiometry are presented. Figures 6.15(a) and 6.15(b) cover the results of the inlet gas relative humidity at 10%. In this condition, the anode presents tendency to dryness. Clearly, the humidification level is low and the back diffusion effect is not able to compensate this lack of water. On the cathode side, the self-humidifying condition is seen for an oxygen stoichiometry value of 2. Condensation is seen towards the right side of the catalyst layer along the z-direction. Under higher stoichiometry values, the water activity on the cathode catalyst layer presents an interesting tendency towards lower levels that is assumed to be due to the back diffusion effect, and the combination of high stoichiometry levels and very low current density. This situation is not seen in any other cases with the current distributed parameter model under analysis.

Figures 6.15(c) and 6.15(d), as well as the pair of Figures 6.15(e) and 6.15(e), present similar behaviour showing the effect of increased humidification. Under a 50 % relative humidity of inlet hydrogen, the anode shows the first signs of over-humidification due to the low current density level. This condition allows for faster liquid water accumulation, which is undesirable at low current densities, hence lower flow rates, and particularly at low temperatures. This combination leads to anode flooding. Condensation is seen towards the right side of the cathode catalyst layer along the z-direction for different values of oxygen stoichimetry. Figures 6.15(g) and 6.15(h) show clear signs of over-humidification of gases. Condensation is seen on most of the anode and cathode catalyst layers length along the z-direction. This situation can lead to both anode and cathode flooding under low current densities scenarios.

In this study, the current density values range from 0.1 A cm^{-2} to 0.2 A cm^{-2} due to the impact of dryness on the protonic conductivity of the polymer electrolyte membrane, and the effects of accumulated liquid water on the ECSA. These effects will also be analysed in detail in further chapters. In summary, Figure 6.14 has demonstrated the importance of spatial variations along the z-direction of the water activity in the anode and cathode catalyst layers. As stated in the previous section, advanced control strategies should take into account the behaviour of spatial profiles and optimally manage the humidification of inlet gases, along with the stoichiometry values of hydrogen and oxygen.

(a) 10% H_2 RH

(b) 10% Air RH

(c) 25% H_2 RH

(d) 25% Air RH

(e) 50% H_2 RH

(f) 50% Air RH
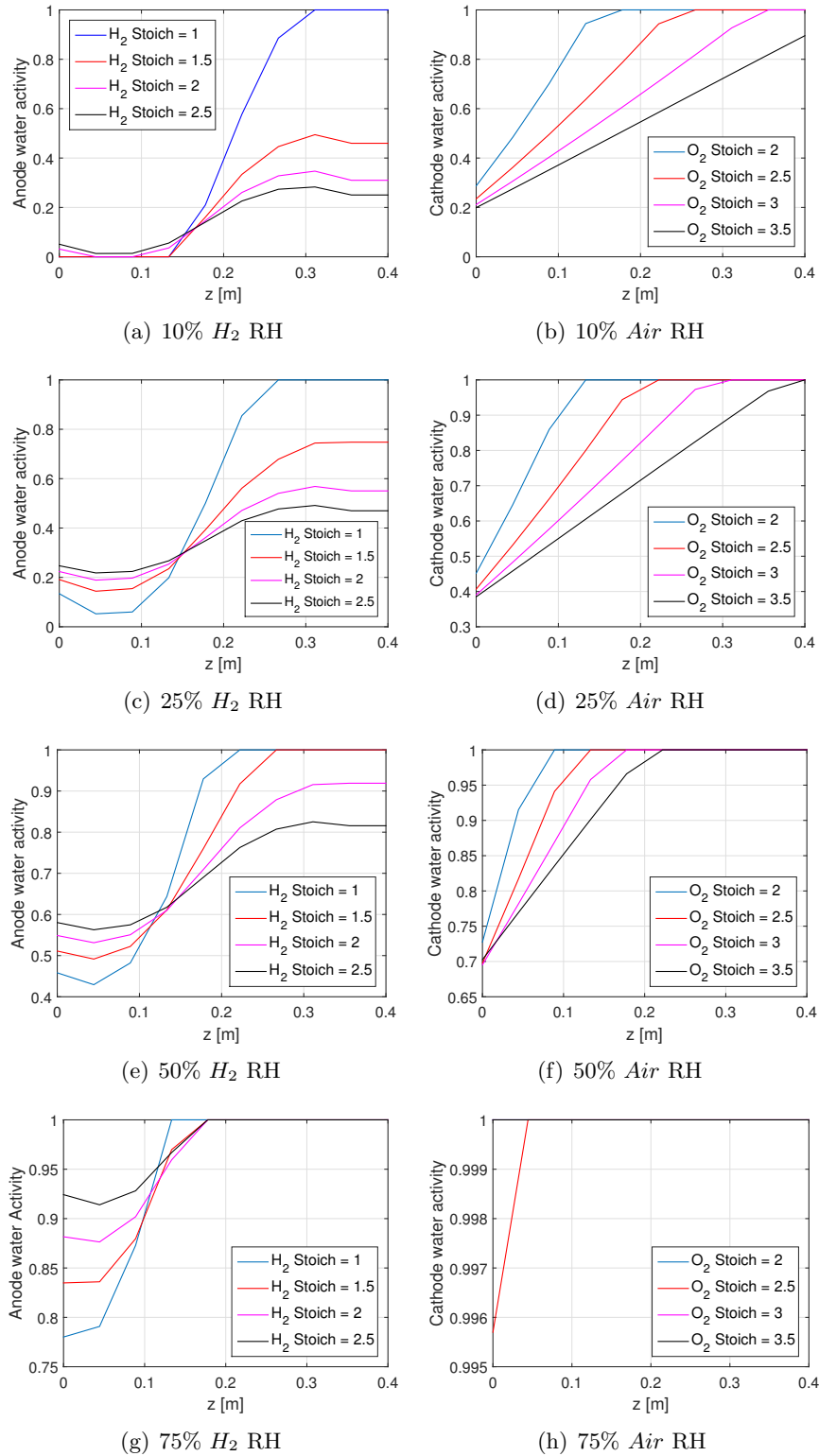
(g) 75% H_2 RH

(h) 75% Air RH
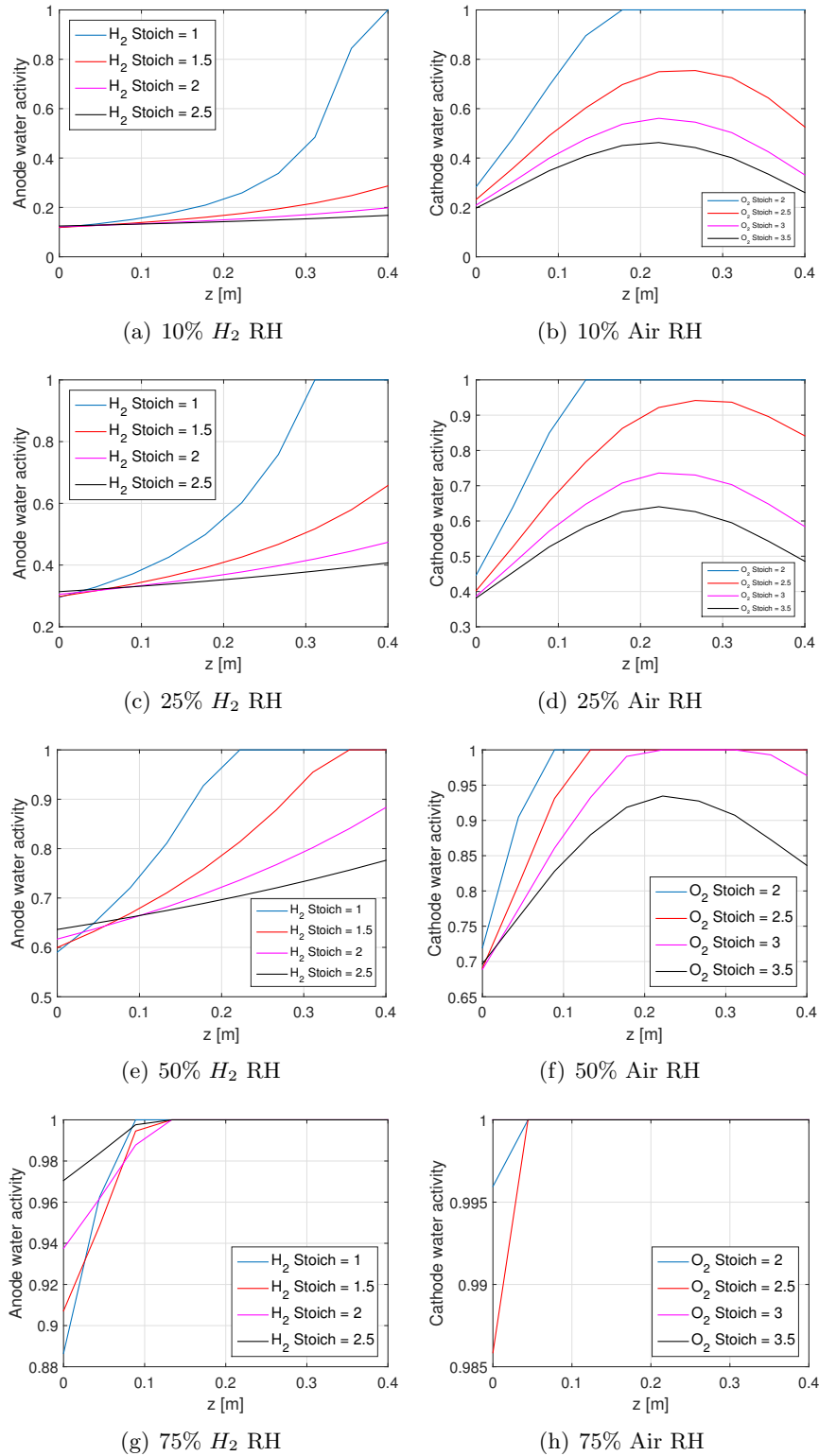
Figure 6.15: Spatial profile of water activity in the anode and cathode catalyst layers along the z-direction under a low current density scenario

6.4   Steady-state analysis of reactant starvation

This study focuses on the distribution of reactants in the anode and cathode along the z-direction. The key objective of the analysis is to recreate, via simulations, the operating conditions and issues that could lead to starvation of reactants. Section 6.2.2 introduced the molar flux densities of hydrogen and oxygen along the channel (horizontal convective flows), as the variables used to confirm the stoichiometry of the PEM fuel cell distributed parameter model under analysis. Table 6.4 shows the simulation parameters considered. Figure 6.16 presents the spatial behaviour of these variables for different hydrogen and oxygen stoichiometry setpoints.

Table 6.4: Operating conditions - Reactants stoichiometry analysis

Variable	Setpoint
H_2 inlet RH	50 %
O_2 inlet RH	45 %
U Cell voltage	0.65 V
Back pressure P	1.01 Bar.a

(a) Anode   (b) Cathode
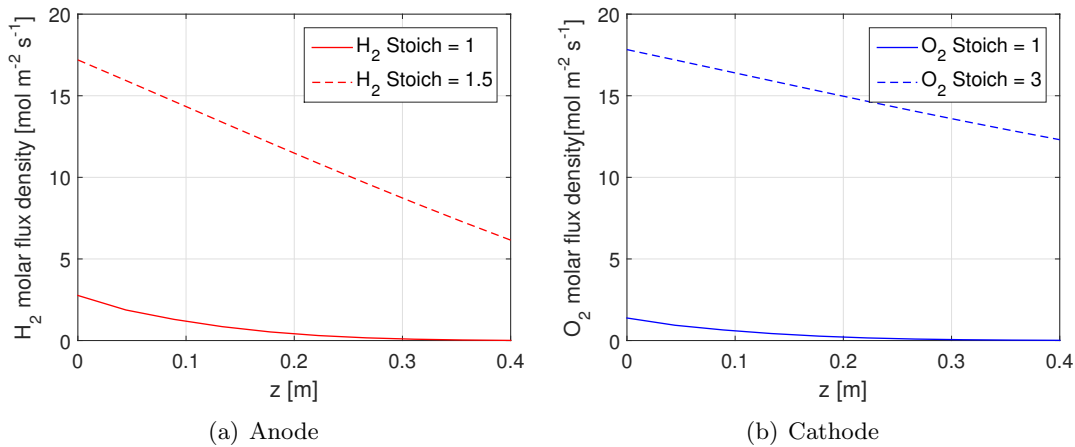
Figure 6.16: Spatial profile of hydrogen and oxygen horizontal flux densities along the z-direction under different stoichiometry setpoints

As expected, the amount of gas towards the outlet end of the gas channels tends to zero for stoichiometry values of 1. In practice, a certain amount of gas crossover is present during the operation of a fuel cell. The amount of crossover gas depends on the current drawn from the cell and its design, manufacturing and assembly. Therefore, it a classical approach in the supply of reactants to use higher stoichiometry levels. However, in the case of hydrogen, this approach leads to a reduction in fuel cell efficiency. Figure 6.16(a) clearly shows excess hydrogen towards the outlet end of the channel. Unless there is a proper recirculation system, this excess fuel will be purged into the exhaust manifold. Hydrogen

recirculation could also carry over some losses due to design issues and hydrogen purification approaches [54].

In addition, high stoichiometries of oxygen require more effort from the air compressor. This situation also impacts the performance of the fuel cell by increasing the parasitic losses affecting the net power output. It is important to point out that in this model the current level is affected by the partial pressure of reactants, which is why lower stoichiometry levels lead to lower current values. Since the voltage is fixed, the current in the two sets of curves for each figure is different.

These results confirm the need for a control strategy that takes into account both, the stoichiometry level and the spatial profile of reactants. Such strategy could supply the appropriate amount of gas to mitigate loss of cell efficiency and also monitor its levels along the z-direction to avoid starvation on both anode and cathode. With this idea established, the following chapters cover the design, implementation and analysis of a distributed parameter control strategy for the supply of reactants.

6.5   Transient-state results

The objective of this study is to analyse the behaviour of the hydrogen and oxygen concentration, as well as the water activity, in three mesh segments, in order to understand the differences in transient-state results for different variables along the spatial profile. Figure 6.17(a) presents the results of a 30-second simulation. Simulation parameters for the transient state analysis are specified in Table 6.5. At 15 seconds, the voltage decreases from 0.65 V down to 0.55 V. Current density levels are respectively 0.3 A m^{-2} and 0.6 A m^{-2}.

Table 6.5: Simulation parameters for transient-state analysis

Variable	Setpoint
H_2 stoichiometry	1.5
O_2 stoichiometry	3
H_2 inlet RH	50 %
O_2 inlet RH	45 %
Back pressure P	1.01 Bar.a

Figure 6.17(a) shows transient results for the hydrogen concentration in mesh segments 1, 6 and 10, which correspond to gas channel inlet segment, middle segment and outlet segment. The different behaviour of the variables is noted. Clearly, the first segment has the higher impact of changes in input variables. In this case, concentration rapidly increases due to the increase in current density. Figure 6.17(b) shows similar results for the concentration of oxygen. Likewise, the step change in current increases the concentration in the different segments of the channel with higher impact on the first segment. It is also important to notice the different response of the system depending on the segment. Changes

in the first segment of the channel are almost immediate, whereas there is a slower time constant further along the channel.

(a) H_2
(b) O_2
(c) H_2
(d) O_2
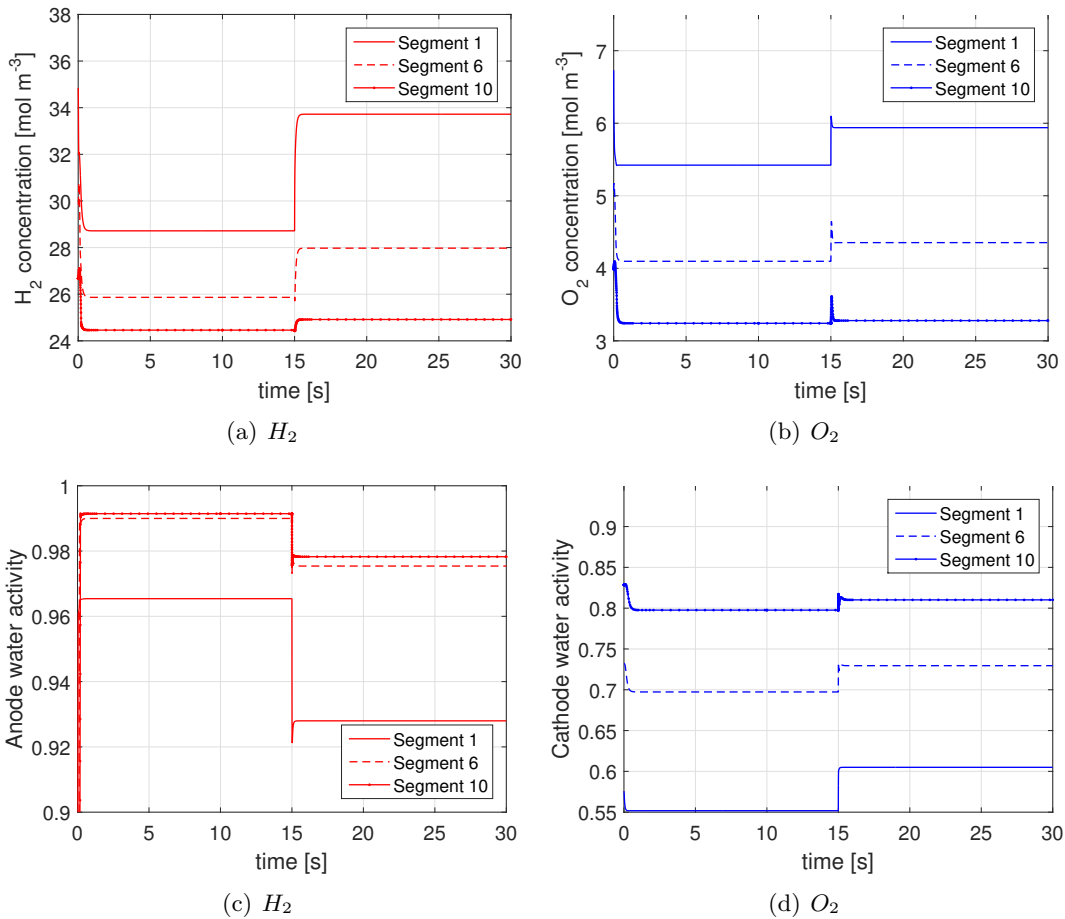
Figure 6.17: Transient-state behaviour variables for different segments along the channel

Figures 6.17(c) and 6.17(c) present the same analysis for the water activity in the anode and cathode catalyst layers. The impact of the electro-osmotic forces, particularly in the first segment, can be seen. This effect has been noticed throughout the different sections of the current chapter and its consequences have been widely discussed. On the cathode side the opposite occurs. The water activity increases in every curve of the figure with major impact on the first segment, due to higher reaction rates in this region of the catalyst layers.

6.6 Conclusions

This chapter has presented a qualitative analysis of the distributed parameter PEM fuel cell model developed in Chapter 5. The results indicate the model gives a good representation of the internal spatial profiles of different cell variables along the direction of the fuel and air streams (z-direction). In addition, the model has been used to analyse scenarios that could lead to drying or flooding in the catalyst layers and starvation of reactants in the gas

channels, three of the most important challenges in the operation of PEM fuel cells. The analyses performed throughout the chapter have demonstrated the importance of spatial variations of variables in the cell for its proper performance and reduction of degradation mechanisms.

The effect of potential control variables has also been evaluated for the different challenges discussed. This study is the first step towards the design of a distributed parameter model-based control strategy of the water activity in the anode and cathode catalyst layers, and the distribution of reactants. This strategy will consider the inlet gas humidification inputs and the reactant stoichiometry inputs as manipulated variables. An optimal combination of these variables can reduce the rate of condensation when possible and avoid starvation of reactants. The knowledge obtained from this analysis will be taken into account in the development of control strategies in the following part of the thesis. The work in this chapter is included in the following contributions:

Journal papers

M.L. Sarmiento-Carnevali, C. Batlle, M. Serra, Analysis of PEM fuel cell operation challenges with a distributed parameter model, to be submitted to the International Journal of Hydrogen Energy in 2017.

M.L. Sarmiento-Carnevali, M. Serra, C. Batlle, Distributed parameter model simulation tool for PEM fuel cells, International Journal of Hydrogen Energy 39, 4044-4052 (2014).

Conference paper

M.L. Sarmiento-Carnevali, M. Serra, C. Batlle, Analysis of conventionally controlled PEMFC based on a distributed parameter model, IV Iberian Symposium on Hydrogen, Fuel Cells and Advanced Batteries (HYCELTEC 2013), June 26-28th, 2013, Estoril, Portugal.

Part III

Control

Chapter 7

Order reduction of a distributed parameter model

In the previous chapters, a non-linear distributed parameter model of a single PEM fuel cell was developed and validated to accurately consider space profiles of variables which are relevant to its performance and durability. The model was discretised in n segments using the central finite differences approach, resulting in a set of ordinary differential equations (ODE) and algebraic equations. Differential algebraic equations (DAE) systems resulting from discretisation of distributed parameter models normally have a large number of equations as appreciated in Chapter 5. The scale of this system not only slows down the numerical simulations, but also increases the complexity of model-based controllers.

It is common practice to neglect spatial variations and consider simplified lumped-parameter models as reference models in control applications, in order to achieve a trade-off between accuracy of the model and computational complexity. However, in this work the spatial profile behaviour is the focus of model-based control strategies that will be presented in Chapter 8. The inclusion of complex DAE models within model-based control schemes requires a previous simplification. Various model order reduction (MOR) techniques are available in the literature to simplify complex models, which consist of reducing the order while preserving the relationship between certain input and output variables determined from the control objectives.

The aim of this chapter is to obtain order reduced models from the anode and cathode submodels of the discretised distributed parameter PEM fuel cell model presented in Chapter 5. These order reduced submodels will be used as reference models in a decentralised distributed parameter model predictive control approach developed in Chapter 8. The resulting order-reduced models are suitable to perform faster numerical simulations and design different control strategies for the original non-linear distributed parameter PEM fuel model.

7.1   Brief review of model order reduction approaches

Model order reduction techniques based on state-space representations involve two major steps [98, 88]. The first step is the transformation of the system to a form that reveals which parts are most important for the input-output behavior, and the second step is the approximation of the model. The basic idea of order reduction invented for linear state space systems, proposed by Moore [68], is to analyse the system and find a linear coordinate change such that the transformed system reveals which coordinate directions are the most important for the input output behaviour. This procedure finds a balanced realisation of the system with diagonal gramians, where the terms in the diagonal are the squared singular values. The reduction is accomplished by removing the states with small singular values.

Scherpen [83] presented an extension of the results for linear state space models to nonlinear state-space models. The major difference is the use of nonlinear variants of the controllability and observability functions. Actual model reduction was made similar to Moore [68], by removing states with small singular value functions. The approach had a drawback because the diffent directions are not really separated from each other. To avoid this drawback Fujimoto and Scherpen [41] proposed an input-normal /output-diagonal form to actually separate directions. Fujimoto and Tsubakino [41] presented results based on power series computations for the standard truncation method.

Krener [88] stated that controllability and observability functions can be written in a so-called input normal form of degree m, which means that the contributions from different coordinate directions are separated up to some desired order. This work presented results based on power series computations, which make them possible to use computationally. In the area of DAE models, Stykel (2004) presented a study of linear DAE Models, including the study of higher index problems. In the case of nonlinear DAE models Hahn and Edgar (2002) and Sun and Hahn (2005) presented works based on covariance measures. More recently, in 2008, Sjoberg [88] presented his thesis work on order reduction and control of nonlinear DAE models.

There are other model order reduction techniques not based on system state-space representations that fall outside the scope of this work. Comprehensive reviews of the variety of these methods can be found in [98, 8, 15].

7.2   Delimitation of the order reduction domain

Figure 7.1 illustrates the distributed parameter model developed in Chapter 5. The z-direction has been discretised in $n = 10$ segments using the central finite differences approach. Most model variables are shown in the scheme. These variables have spatial profiles along the z-direction. Detailed information of the model development, implementation, variables and parameters can be found in Chapter 5.

Non-linear submodels for the anode layers and cathode layers are derived from the non-
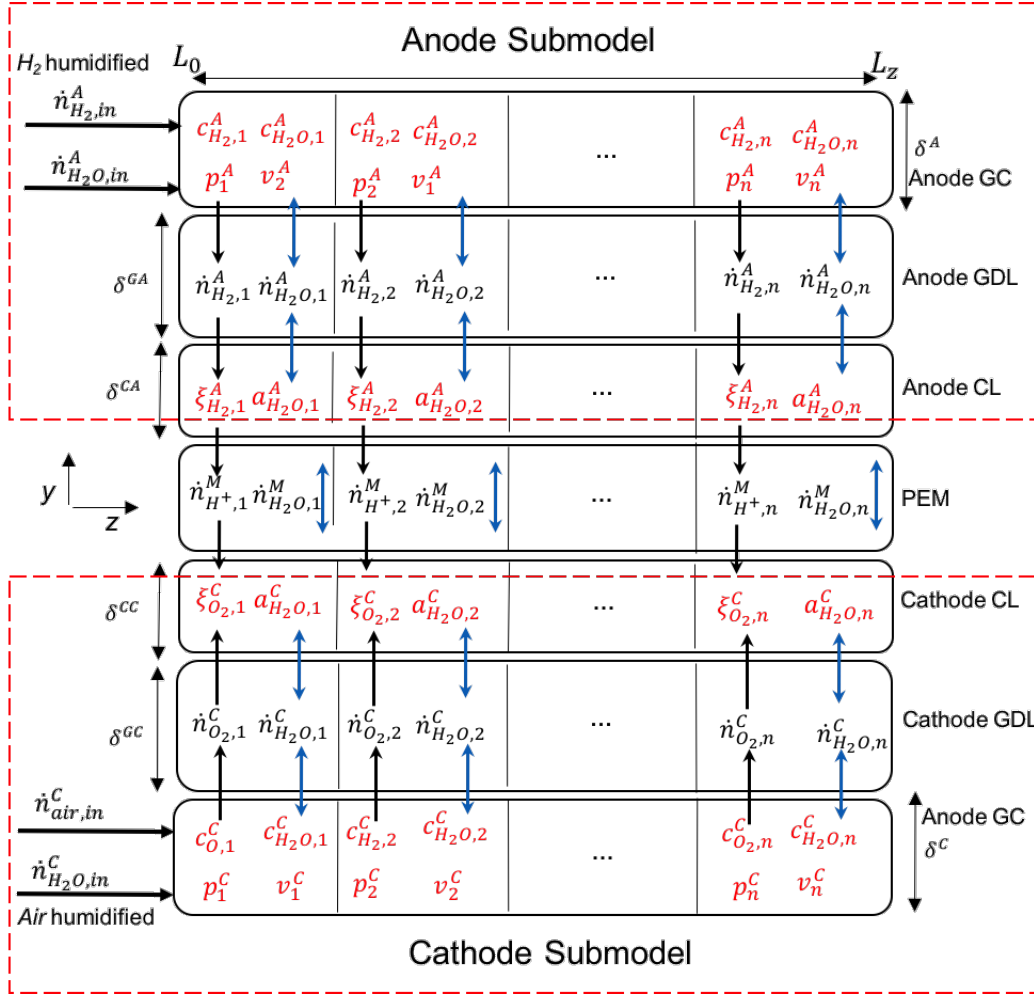
Figure 7.1: Distributed parameter anode and cathode submodels

linear PEM fuel cell distributed parameter model (in red dashed boxes). The submodels are represented by corresponding equations (5.4-5.27), as well as equation 5.40, presented in Chapter 5. Both models consider ordinary differential equations (ODE) and algebraic equations. Variables in red belong to each submodel. The molar density fluxes from the gas channels through the GDL towards the catalyst layers $\dot{n}_{H_2,k}^A$, $\dot{n}_{H_2O,k}^A$, $\dot{n}_{O_2,k}^C$, $\dot{n}_{N_2,k}^C$ and $\dot{n}_{H_2O,k}^C$ ($k = 1..10$) depend on the electrochemical submodel of the catalyst layer and polymer electrolyte membrane submodel. These variables are considered external to the anode and cathode submodels and will be treated as measured disturbances in the following chapter. Corresponding model variables (before order reduction) are:

Anode sub-model

- States (x_1 vector): $c_{H_2,k}^A$ and $c_{H_2O,k}^A$ ($k = 1..10$),

- Algebraic variables (x_2 vector): p_k^A and v_k^A ($k = 1..10$),

- Inputs (u vector): hydrogen inlet $\dot{n}^A_{H_2,in}$ and water inlet $\dot{n}^A_{H_2O,in}$,

- Outputs (y vector): water activity in segments $a^A_{H_2O,1}$, $a^A_{H_2O,6}$, $a^A_{H_2O,10}$ and average water activity level $a^A_{H_2O,avrg}$.

Cathode sub-model

- States (x_1 vector): $c^C_{O_2,k}$, $c^C_{N_2,k}$ and $c^C_{H_2O,k}$ ($k = 1..10$),

- Algebraic variables (x_2 vector): p^C_k and v^C_k ($k = 1..10$),

- Inputs (u vector): air inlet $\dot{n}^C_{O_2,in}$, $\dot{n}^C_{N_2,in}$ and the cathode water inlet $\dot{n}^C_{H_2O,in}$,

- Outputs (y vector): water activity in segments $a^C_{H_2O,1}$, $a^C_{H_2O,6}$, $a^C_{H_2O,10}$ and average water activity level $a^C_{H_2O,avrg}$.

The outputs are defined as values at key points of the water activity profiles of the anode and cathode catalyst layer, i.e. the water activity in the first, middle and last mesh segments. Results shown in Chapter 5 indicate that these three outputs provide enough information to monitor and control the overall water activity profiles. Each DAE system has the form

$$
\begin{aligned}
F_1\left(\dot{x}_1, x_1, x_2, u\right) &= 0, \\
F_2\left(x_1, x_2, u\right) &= 0, \\
y - h\left(x_1, x_2, u\right) &= 0,
\end{aligned}
\tag{7.1}
$$

where $x_1 \in \mathbb{R}^d$ is the state vector, $x_2 \in \mathbb{R}^a$ is the vector of algebraic variables, $u \in \mathbb{R}^r$ is inputs vector, and $y \in \mathbb{R}^q$ is the outputs vector. In addition, the DAE model has an underlying ODE description,

$$
\begin{aligned}
\dot{x}_1 &= \mathcal{L}\left(x_1, x_2, u\right), \\
x_2 &= \mathcal{R}\left(x_1, u\right),
\end{aligned}
\tag{7.2}
$$

therefore, it follows that

$$
\begin{aligned}
\dot{x}_1 &= \mathcal{L}\left(x_1, \mathcal{R}\left(x_1, u\right), u\right), \\
y &= h\left(x_1, \mathcal{R}\left(x_1, u\right), u\right).
\end{aligned}
\tag{7.3}
$$

After both sub-models are completely defined, balanced truncation is used to reduce their order. A brief description of the sequence of steps followed in the order reduction process of each sub-model is given in the following sections. Detailed information of the balanced truncation technique can be found in [8].

7.3   Balanced truncation model order reduction

The first method used to reduce the order of the anode and cathode nonlinear DAE sub-models requires linearising the original DAE model around an equilibrium point of interest, then computing the corresponding controllability and observability functions. The final step is finding an appropriate model realization that reveals which states of the original system can be truncated without considerably affecting the original input-output behaviour [68, 8].

The DAE system is linearised around an equilibrium point of interest that is described in Section 7.3.5. The resulting model in state-space representation is

$$\dot{x}_1 = Ax_1 + Bu, \tag{7.4}$$

$$y = Cx_1. \tag{7.5}$$

7.3.1   Computation of the controllability function

The controllability function $L_c(x_{1,0}))$ measures the minimal amount of energy in the control signal u, required to reach a specific state x. It is defined as the solution to the optimal control problem,

$$L_c(x_{1,0}) = \min_{u(.)} J_c \tag{7.6}$$

s.t.

$$\begin{aligned}
\dot{x}_1 &= \mathcal{L}(x_1, x_2, u) \\
x_2 &= \mathcal{R}(x, u) \\
x_1(0) &= x_{1,0} \in \Omega_x \\
0 &= \lim_{t \to -\infty} x_1(t),
\end{aligned} \tag{7.7}$$

where J_c is a measure of the control signal energy

$$J_c = \frac{1}{2} \int_{-\infty}^{0} u(t)^T u(t) \, dt, \tag{7.8}$$

Due to the original model complexity, a local solution of the controllability function is computed, valid in a neighbourhood of a specific equilibrium point. The result expressed as a convergent power series expansion up to some desired order is

$$L_c(x_1) = \frac{1}{2} x_1^T G_c x_1 + L_{ch}(x_1), \tag{7.9}$$

where G_c is a positive definite matrix, which is the inverse of the controllability Gramian, and $L_{ch}(x_1)$ contains terms of order three or higher. In this case study, $L_{ch}(x_1) = 0$. Therefore, the controllability function is approximated by a quadratic form that corresponds

to a linear approximation of the original nonlinear model around a desired equilibrium point (Table 7.1). The G_c matrix is obtained by solving the Lyapunov equation

$$G_c A + A^T G_c + G_c B B^T G_c = 0, \tag{7.10}$$

where A and B are the resulting state and input matrices of the previously linearised DAE system.

7.3.2 Computation of the observability function

The observability function measures the energy in the output signal for certain initial state conditions. It is defined as

$$L_o\left(x_1\left(0\right)\right) = \frac{1}{2} \int_{-\infty}^{0} y\left(t\right)^T y\left(t\right) dt$$
$$x_1\left(0\right) = x_{1,0} \in \Omega_x \tag{7.11}$$
$$u\left(t\right) = 0, \qquad 0 \leq t < -\infty$$

Considering a DAE model in the form of (7.1), the goal if to find $L_o\left(x_1\right)$ as a convergent power series on some neighborhood of $x_1 = 0$, up to a desired order

$$L_o\left(x_1\right) = \frac{1}{2} x_1^T G_o x_1 + L_{oh}\left(x_1\right), \tag{7.12}$$

where G_o is the observability Gramian (positive definite matrix) computed by solving the following Lyapunov equation

$$G_o A + A^T G_o + C^T C = 0, \tag{7.13}$$

and A and C are the resulting state and output matrices of the linearised DAE system. The observability function is approximated by a quadratic form as well, which corresponds to a linear approximation of the original nonlinear model.

7.3.3 Computation of an appropriate coordinate change

Once the controllability and observability functions are computed up to order two in this case study

$$L_c\left(x_1\right) = \frac{1}{2} x_1^T G_c X_1, \tag{7.14}$$

$$L_o\left(x_1\right) = \frac{1}{2} x_1^T G_o x_1, \tag{7.15}$$

a linear change of coordinates is used to simultaneously diagonalize G_c^{-1} and G_o as

$$\Sigma = G_c^{-1} = G_o = diag\left(\sigma_1, \sigma_2, \ldots, \sigma_n, \right), \tag{7.16}$$

where $\sigma_1 \geq \sigma_2 \geq \cdots \geq \sigma_n > 0$ [4]. These σ_i values $(i = 1, \ldots, n)$ are denoted Hankel singular values and σ_1 is the Hankel norm of the system. A representation where the two Gramians are equal and diagonal is called balanced. A small σ_i means the amount of control energy required to reach the state $z = (0, \ldots, 0, z_i, 0, \ldots, 0)$ is large, while the output energy generated by the same state is small (z being the new set of states). Computing this balanced realization requires performing Cholesky factorizations of the Gramians

$$G_c = XX^T, \quad G_o = YY^T, \tag{7.17}$$

where $X > 0$ and $Y > 0$. Then, the singular value decomposition (SVD) of $Y^T X$ is computed

$$Y^T X = U\Sigma V^T, \tag{7.18}$$

where U and V are orthogonal. Finally

$$\Sigma = diag\left(\sigma_1, \sigma_2, \ldots, \sigma_n\right). \tag{7.19}$$

The balancing transformation is given by

$$T = XV\Sigma^{-1/2}, \quad \text{with} \quad T^{-1} = \Sigma^{-1/2}U^TY^T. \tag{7.20}$$

The balanced realization is given by the linear system

$$\tilde{A} = T^{-1}AT, \quad \tilde{B} = T^{-1}B, \quad \tilde{C} = CT, \tag{7.21}$$

and

$$\Sigma = \tilde{G}_c^{-1} = \tilde{G}_o. \tag{7.22}$$

7.3.4 Truncation

The reduced model is obtained finding a major gap between two Hankel singular values, i.e. if $\sigma_k \gg \sigma_{k+1}$ for some k. In this subsection k indicates the dimension of the new set of states. The last z_{k+1} to z_d states of the balanced realization are left out without considerably affecting the input-output behaviour, compared to the original system. Recalling the original DAE model of (7.3), the balanced realization can be expressed as

$$\dot{z} = \tilde{\mathcal{L}}\left(z_a, z_b, u\right),$$
$$y = \tilde{h}\left(z_a, z_b, u\right), \tag{7.23}$$

where $z = (z_a, z_b)$ is the new set of states divided into two subsets determined by the Hankel singular values. The reduced order model is

$$\dot{z} = \tilde{\mathcal{L}}\left(z_a, 0, u\right),$$
$$y = \tilde{h}\left(z_a, 0, u\right). \tag{7.24}$$

The resulting reference models of the anode and cathode are linear time-invariant models of the form

$$\dot{z}_a = A_{red}z_a + B_{red}u,$$
$$y = C_{red}z_a, \tag{7.25}$$

where $z_a \in \mathbb{R}^k$ is the state vector, $u \in \mathbb{R}^r$ are the control inputs, and $y \in \mathbb{R}^q$ are the outputs. Note that the new set z_a of states has no physical meaning since it is a linear combination of the full order set of states. The inputs and outputs remain the same and, ideally, the internal dynamics of the reduced order model preserve the input-output relation of the original DAE.

7.3.5   Model order reduction results

The set of equations presented in the previous section was implemented in MATLAB to obtain the reference models. In order to test the accuracy of the reduced-order models, step responses from the anode and cathode full order non-linear models, along with responses from reduced models with different number of states were simulated and compared. Table 7.1 shows fixed simulation parameters before step change. Figure 7.2 presents the results of order-reduced models with different number of states, along with the response of the original full order non-linear model. This study is focused on the average water activity of anode and cathode catalyst layers since these are key variables in the control design and implementation chapter. In addition, the average water activity allows to confirm the approximation of the concentration of gases by the order-reduced models.

Table 7.1: Operating conditions to analyse order-reduced models

Variable	Setpoint
H_2 stoichiometry	1.5
O_2 stoichiometry	3
H_2 inlet RH	50 %
O_2 inlet RH	45 %
T Cell temperature	344 K
Back pressure P	1.01 Bar.a

Figure 7.2(a) shows the response of the average water activity in the anode catalyst layer $(a_{H_2O}^A)$ upon a step change in voltage from 0.65 V down to 0.55 V at time $= 15$ seconds. As
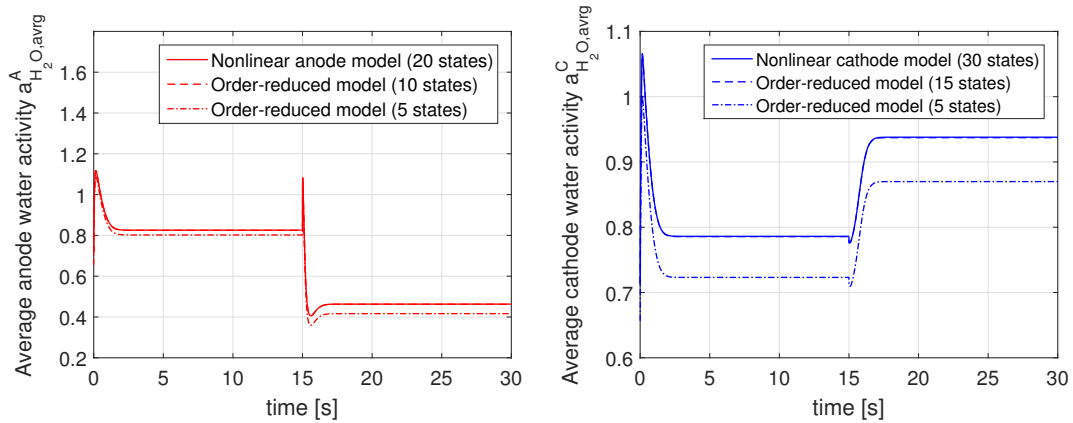
(a) Anode order-reduced models vs. Full order model

(b) Cathode order-reduced models vs. Full order model
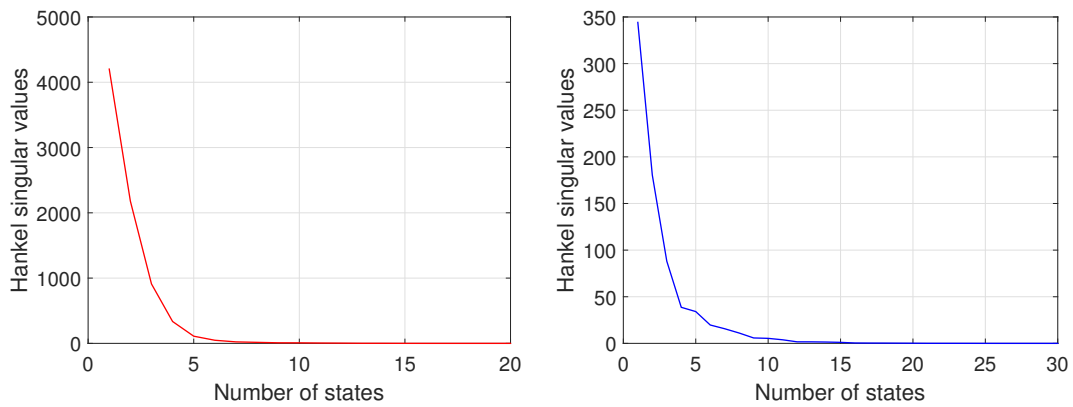
(c) Hankel Singular Values for anode model order reduction

(d) Hankel Singular Values for cathode model order reduction

Figure 7.2: Outputs of reference models obtained with different number of states vs. corresponding nonlinear fuel cell model outputs. Comparative under a voltage step change.

expected, under increasing current density scenarios, the average water activity drops due to the electro-osmotic drag effect. Notice how the order-reduced model with half the number of original states is able to approximate the behaviour of the full order model correctly during the entire simulation period. The order-reduced model with 5 states presents a certain offset. The definite reduced model for control purposes is then the 10-state model. Figure 7.2(b) shows the Hankel Sigular Values of the order reduction process for the anode submodel. This graph is important in order to decide how many states will be left out to reduce the order of the original model. The result confirms the behaviour of the different order-reduced models, indicating between 10 to 15 states of the balanced realization could be truncated without affecting the input-output behaviour of this submodel.

Likewise, Figure 7.2(c) shows the response of the average water activity in the cathode catalyst layer $(a_{H_2O}^C)$ upon a step change in voltage from 0.65 V down to 0.55 V at time = 15 seconds. As expected, under increasing current density scenarios, the average water

activity rapidly increases due to water generated by the electrochemical reaction. Notice, again, how the order-reduced model with half the number of original states is able to approximate the behaviour of the full order model correctly during the entire simulation period. The order-reduced model with 5 states presents a certain offset. In this case, the definite reduced model for control purposes is the 15-state model. Figure 7.2(d) shows the Hankel Sigular Values of the order reduction process for the cathode submodel. Similarly, the result confirms the behaviour of the different order-reduced models, indicating between 15 to 20 states of the balanced realization could be truncated without affecting the input-output behaviour of this submodel. Corresponding matrices of the different order-reduced models can be found in Appendix C.

7.4   Parameter-dependent model order reduction

A variation of the balanced truncation technique is also used in this work to increase the accuracy of the linear reference models. This work was recently published by Batlle and Roqueiro [14]. The result of this technique is an order-reduced model that incorporates the effects of changes in important external variables. Applying this method, the modified reference models consider a parameter m that accounts for temperature deviations from the equilibrium operating point. This parameter is considered as a measured disturbance to MPC controllers in Chapter 8,

$$
\begin{aligned}
\dot{z}_a &= A_{red}\left(m\right) z_a + B_{red}\left(m\right) u, \\
y &= C_{red}\left(m\right) z_a.
\end{aligned}
\tag{7.26}
$$

This section presents a summary of the equations from [14] implemented in MATLAB to obtain the parameter-dependent order-reduced models of the form (7.26) in this thesis. Extended details of the parameter-dependent model order reduction technique are presented in the reference work. The procedure is similar to the sequence of steps followed to obtain the model (7.25). Consider the linear system

$$
\begin{aligned}
\dot{x} &= A(m)x + B(m)u, \tag{7.27} \\
y &= C(m)x, \tag{7.28}
\end{aligned}
$$

where m a symbolic parameter. The controllability Gramian also depends on m, and is given by the solution $W^c(m)$ to the Lyapunov equation

$$
A(m)W^c(m) + W^c(m)A^T(m) + B(m)B^T(m) = 0.
\tag{7.29}
$$

Assuming that $A(m)$, $B(m)$ and $C(m)$ are analytic in m,

$$A(m) = \sum_{k=0}^{\infty} A_k m^k, \tag{7.30}$$

$$B(m) = \sum_{k=0}^{\infty} B_k m^k, \tag{7.31}$$

$$C(m) = \sum_{k=0}^{\infty} C_k m^k, \tag{7.32}$$

solutions of the form

$$W^c(m) = \sum_{k=0}^{\infty} W_k^c m^k, \tag{7.33}$$

are found considering equations equivalent to the set of Lyapunov equations

$$A_0 W_0^c + W_0^c A_0^T + B_0 B_0^T = 0, \tag{7.34}$$

$$A_0 W_r^c + W_r^c A_0^T + P_r = 0, \ r = 1, 2, \ldots, \tag{7.35}$$

with

$$P_r = B_0 B_r^T + \sum_{s=0}^{r-1} \left(A_{r-s} W_s^c + W_s^c A_{r-s}^T + B_{r-s} B_s^T \right), \quad r = 1, 2, \ldots \tag{7.36}$$

These equations can be solved recursively to the desired order, starting with the zeroth order Lyapunov equation (7.34). The internal dynamics is always given by A_0, and only the effective control term P_r changes with the order.

Similarly, the observability Gramian $W^o(m)$ satisfies

$$A^T(m)W^o(m) + W^o(m)A(m) + C^T(m)C(m) = 0, \tag{7.37}$$

and its power series solution

$$W^o(m) = \sum_{k=0}^{\infty} W_k^o m^k, \tag{7.38}$$

can be obtained recursively from

$$A_0^T W_0^o + W_0^o A_0 + C_0^T C_0 = 0, \tag{7.39}$$

$$A_0^T W_r^o + W_r^o A_0 + Q_r = 0, \ r = 1, 2, \ldots, \tag{7.40}$$

with

$$Q_r = C_0^T C_r + \sum_{s=0}^{r-1} \left(A_{r-s}^T W_s^o + W_s^o A_{r-s} + C_{r-s}^T C_s \right), \quad r = 1, 2, \ldots \tag{7.41}$$

After computing $W^c(m)$ and $W^o(m)$ at the desired order, the next step in the balancing transformation procedure is to compute their "square roots", $X(m)$ and $Y(m)$, such that

$$W^c(m) = X(m)X^T(m), \tag{7.42}$$

$$W^o(m) = Y(m)Y^T(m). \tag{7.43}$$

Considering

$$X(m) = \sum_{k=0}^{\infty} X_k m^k, \tag{7.44}$$

then

$$W_k^c = \sum_{s=0}^{k} X_{k-s} X_s^T, \tag{7.45}$$

which, again, are equations solved recursively as

$$X_0 X_0^T = W_0^c, \tag{7.46}$$

$$X_k X_0^T + X_0 X_k^T = W_k^c - \sum_{s=1}^{k-1} X_{k-s} X_s^T. \tag{7.47}$$

Similarly, for

$$Y(m) = \sum_{k=0}^{\infty} Y_k m^k, \tag{7.48}$$

then

$$Y_0 Y_0^T = W_0^o, \tag{7.49}$$

$$Y_k Y_0^T + Y_0 Y_k^T = W_k^o - \sum_{s=1}^{k-1} Y_{k-s} Y_s^T. \tag{7.50}$$

Equations (7.46) and (7.49) are standard Cholesky equations, but (7.47) and (7.50) are not Lyapunov (or Sylvester) equations for X_k or Y_k because of the presence of X_k^T and Y_k^T, respectively. Considering a series of assumptions presented in [14], these equations obey

$$S_k X_0^T + X_0 S_k = W_k^c - \sum_{s=1}^{k-1} X_{k-s} X_s^T, \tag{7.51}$$

$$T_k X_0^T + X_0 T_k = 0. \tag{7.52}$$

Equations (7.51) and (7.52) are Lyapunov equations, and in fact the generic solution to (7.52) is $T_k = 0$. The solution to (7.47) is given by

$$X_k = S_k, \tag{7.53}$$

with S_k the solution to the Lyapunov equation (7.51), and an analogous reasoning applies to the solution of (7.50).

The last nontrivial step in the balancing algorithm is the singular value decomposition (SVD) of the product $Y^T(m)X(m)$,

$$Y^T(m)X(m) = U(m)\Sigma(m)V^T(m), \tag{7.54}$$

where

$$\Sigma(m) = \mathrm{diag}(\sigma_1(m) \geq \sigma_2(m) \geq \ldots \geq \sigma_n(m) > 0), \tag{7.55}$$

and $U(m)$ and $V(m)$ are $N \times N$ orthogonal matrices, depending also on the parameter m. The R_k coefficients of the power series of $Y^T(m)X(m)$ are given by

$$Y^T(m)X(m) = \sum_{k=0}^{\infty} R_k m^k, \tag{7.56}$$

with

$$R_k = \sum_{s=0}^{k} Y_{k-s}^T X_s = \sum_{s=0}^{k} Y_s^T X_{k-s}. \tag{7.57}$$

Let also

$$U(m) = \sum_{k=0}^{\infty} U_k m^k, \tag{7.58}$$

$$V(m) = \sum_{k=0}^{\infty} V_k m^k, \tag{7.59}$$

$$\Sigma(m) = \sum_{k=0}^{\infty} \Sigma_k m^k. \tag{7.60}$$

Denoting $u_j^{(k)}$ as the jth column vector of U_k, $v_j^{(k)}$ as the jth column vector of V_k and $\sigma_j^{(k)}$ as the jth element of the diagonal matrix Σ_k, finally, the first-order correction to the singular values is given by

$$\sigma_i^{(1)} = \left\langle u_i^{(0)} \middle| R_1 v_i^{(0)} \right\rangle = \left\langle v_i^{(0)} \middle| R_1^T u_i^{(0)} \right\rangle, \tag{7.61}$$

where each $u_i^{(1)}$ can be uniquely computed as the solution to the system

$$\begin{pmatrix} R_0 R_0^T - (\sigma_i^{(0)})^2 \mathbb{I} \\ (u_i^{(0)})^T \end{pmatrix} u_i^{(1)} = \begin{pmatrix} Q_i^{(1)} \\ 0 \end{pmatrix}, \tag{7.62}$$

with

$$Q_i^{(1)} = 2\sigma_i^{(0)} \sigma_i^{(1)} u_i^{(0)} - R_0 R_1^T u_i^{(0)} - \sigma_i^{(0)} R_1 v_i^{(0)}. \tag{7.63}$$

Similarly, for $v_i^{(1)}$

$$\begin{pmatrix} R_0^T R_0 - (\sigma_i^{(0)})^2 \mathbb{I} \\ (v_i^{(0)})^T \end{pmatrix} v_i^{(1)} = \begin{pmatrix} P_i^{(1)} \\ 0 \end{pmatrix}, \tag{7.64}$$

with

$$P_i^{(1)} = 2\sigma_i^{(0)} \sigma_i^{(1)} v_i^{(0)} - R_0^T R_1 v_i^{(0)} - \sigma_i^{(0)} R_1^T u_i^{(0)}. \tag{7.65}$$

The second order correction to the singular values is given by

$$\sigma_i^{(2)} = \frac{1}{2} \sigma_i^{(0)} \left(||u_i^{(1)}||^2 - ||v_i^{(1)}||^2 \right) + \left\langle u_i^{(0)} \middle| R_1 v_i^{(1)} + R_2 v_i^{(0)} \right\rangle. \tag{7.66}$$

Notice that the right-hand side depends only on data from the zeroth and first order approximations, plus the second order perturbation R_2.

Under the same conditions as for the first order correction, the $u_i^{(2)}$ are then the unique solution to

$$\begin{pmatrix} R_0 R_0^T - (\sigma_i^{(0)})^2 \mathbb{I} \\ (u_i^{(0)})^T \end{pmatrix} u_i^{(2)} = \begin{pmatrix} Q_i^{(2)} \\ -\frac{1}{2} ||u_i^{(1)}||^2 \end{pmatrix}, \tag{7.67}$$

with

$$\begin{aligned} Q_i^{(2)} &= -R_0 R_1^T u_i^{(1)} - R_0 R_2^T u_i^{(0)} + \sigma_i^{(0)} \sigma_i^{(1)} u_i^{(1)} \\ &+ \sigma_i^{(1)} R_0 v_i^{(1)} + 2\sigma_i^{(0)} \sigma_i^{(2)} u_i^{(0)} - \sigma_i^{(0)} R_1 v_i^{(1)} - \sigma_i^{(0)} R_2 v_i^{(0)}. \end{aligned} \tag{7.68}$$

Similarly, the $v_i^{(2)}$ are given by the solution to

$$\begin{pmatrix} R_0^T R_0 - (\sigma_i^{(0)})^2 \mathbb{I} \\ (v_i^{(0)})^T \end{pmatrix} v_i^{(2)} = \begin{pmatrix} P_i^{(2)} \\ -\frac{1}{2} ||v_i^{(1)}||^2 \end{pmatrix}, \tag{7.69}$$

with

$$\begin{aligned} P_i^{(2)} &= -R_0^T R_1 v_i^{(1)} - R_0^T R_2 v_i^{(0)} + \sigma_i^{(0)} \sigma_i^{(1)} v_i^{(1)} \\ &+ \sigma_i^{(1)} R_0^T u_i^{(1)} + 2\sigma_i^{(0)} \sigma_i^{(2)} v_i^{(0)} - \sigma_i^{(0)} R_1^T u_i^{(1)} - \sigma_i^{(0)} R_2^T u_i^{(0)}. \end{aligned} \tag{7.70}$$

Notice that the matrices appearing on the left hand-sides of (7.67) and (7.69) are the same than the ones in (7.62) and (7.64), respectively, and therefore the solutions are unique. This procedure can be repeated to obtain higher order corrections in m. In this work, corrections up to the second order are considered.

Since the matrix $\Sigma(m)$ is diagonal, $\Sigma(m)^{-1/2}$ is defined diagonal-wise. Up to order m^2, for each entry $\sigma_i(m)$

$$\begin{aligned} (\sigma_i(m))^{-1/2} &= (\sigma_i^{(0)} + m\sigma_i^{(1)} + m^2\sigma_i^{(2)})^{-1/2} \\ &= \frac{1}{(\sigma_i^{(0)})^{1/2}} - m\frac{\sigma_i^{(1)}}{2(\sigma_i^{(0)})^{3/2}} \\ &+ m^2\left(-\frac{\sigma_i^{(2)}}{2(\sigma_i^{(0)})^{3/2}} + \frac{3(\sigma_i^{(1)})^2}{8(\sigma_i^{(0)})^{5/2}} \right) + O(m^3) \tag{7.71} \\ &\equiv s_i^{(0)} + m s_i^{(1)} + m^2 s_i^{(2)} + O(m^3). \tag{7.72} \end{aligned}$$

Hence,

$$\Sigma(m)^{-1/2} = S_0 + m S_1 + m^2 S_2, \tag{7.73}$$

with

$$S_a = \text{diag}(s_i^{(a)}), \quad a = 0, 1, 2. \tag{7.74}$$

Up to order m^2, the matrix $T(m)$ for the transformation from the original x coordinates to the balanced ones z, $x = Tz$, and its inverse $T^{-1}(m)$, are given by $T(m) = T_2(m) + O(m^3)$ and $T^{-1}(m) = T_2^{-1}(m) + O(m^3)$, with

$$
\begin{aligned}
T_2(m) &= X_0 V_0 S_0 + m(X_0 V_0 S_1 + X_0 V_1 S_0 + X_1 V_0 S_0) \\
&+ m^2(X_0 V_0 S_2 + X_2 V_0 S_0 + X_0 V_2 S_0 \\
&\quad + X_0 V_1 S_1 + X_1 V_0 S_1 + X_1 V_1 S_0) & (7.75) \\
&\equiv T_0 + m T_1 + m^2 T_2, & (7.76) \\
T_2^{-1}(m) &= S_0 U_0^T Y_0^T + m(S_0 U_1^T Y_0^T + S_0 U_0^T Y_1^T + S_1 U_0^T Y_0^T) \\
&+ m^2(S_0 U_0^T Y_2^T + S_0 U_2^T Y_0^T + S_2 U_0^T Y_0^T \\
&\quad + S_1 U_1^T Y_0^T + S_1 U_0^T Y_1^T + S_0 U_1^T Y_1^T) & (7.77) \\
&\equiv \hat{T}_0 + m \hat{T}_1 + m^2 \hat{T}_2, & (7.78)
\end{aligned}
$$

From these, the approximation of the balanced realization, up to the second order in m, is given by

$$
\begin{aligned}
\tilde{A}_2(m) &= \hat{T}_0 A_0 T_0 + m(\hat{T}_0 A_1 T_0 + \hat{T}_0 A_0 T_1 + \hat{T}_1 A_0 T_0) \\
&+ m^2(\hat{T}_0 A_0 T_2 + \hat{T}_0 A_2 T_0 + \hat{T}_2 A_0 T_0 \\
&\quad + \hat{T}_0 A_1 T_1 + \hat{T}_1 A_0 T_1 + \hat{T}_1 A_1 T_0), & (7.79) \\
\tilde{B}_2(m) &= \hat{T}_0 B_0 + m(\hat{T}_0 B_1 + \hat{T}_1 B_0) + m^2(\hat{T}_0 B_2 + \hat{T}_2 B_0 + \hat{T}_1 B_1), & (7.80) \\
\tilde{C}_2(m) &= C_0 T_0 + m(C_0 T_1 + C_1 T_0) + m^2(C_0 T_2 + C_2 T_0 + C_1 T_1). & (7.81)
\end{aligned}
$$

Matrices (7.79)—(7.81) define a balanced realization of the original system which is exact for $m = 0$ and approximate to order m^2 for $m \neq 0$. As in the classic balanced truncation technique, a reduced system of order r is obtained by truncating this realization so that only the first r states are kept. For $m = 0$ the error comes from the truncation associated to the number of states.

For $m \neq 0$ errors introduced by the Taylor truncations in the steps of the procedure are present. As stated before, the model has the form of 7.26. Corresponding model inputs and outputs after order reduction are:

Anode parameter-dependent order-reduced model

- Inputs (u vector): hydrogen inlet flux $\dot{n}_{H_2,in}^A$ and anode water inlet flux $\dot{n}_{H_2O,in}^A$.

- Disturbances: temperature deviations given by changes in parameter m (in parameter-dependent matrices).

- Outputs (y vector): water activity in segments $a_{H_2O,1}^A$, $a_{H_2O,6}^A$, $a_{H_2O,10}^A$ and average water activity level $a_{H_2O,avrg}^A$.

Cathode parameter-dependent order-reduced model

- Inputs (u vector): air inlet flux $\dot{n}^C_{O_2,in}$, $\dot{n}^C_{N_2,in}$ and cathode water inlet flux $\dot{n}^C_{H_2O,in}$.

- Disturbances: temperature deviations given by changes in parameter m (in parameter-dependent matrices).

- Outputs (y vector): water activity in segments $a^C_{H_2O,1}$, $a^C_{H_2O,6}$, $a^C_{H_2O,10}$ and average water activity level $a^C_{H_2O,avrg}$.

Matrices of the models can be found in Appendix C.

7.5 Comparative analysis

A final study is performed to compared order-reduced models obtained using the classic balance truncation technique with those obtained with the parameter-dependent technique, in the presence of temperature deviations from the equilibrium point (70°C) used in the linearisation step. Table 7.2 shows the fixed simulation parameters. Figure 7.3 depicts the results of two options of reference model for anode and cathode. The anode full order nonlinear model has 20 states and the cathode full order nonlinear model has 30 states. For anode and cathode, both kinds of reference models are designed around an equilibrium point of 70°C. At time $= 15$ s, a step change in temperature from 70°C to 80°C is considered to test the accuracy of the different reference models. Simulations are in open loop.

Table 7.2: Operating conditions to analyse order-reduced models

Variable	Setpoint
H_2 stoichiometry	1.5
O_2 stoichiometry	3
H_2 inlet RH	50 %
O_2 inlet RH	45 %
I Cell current	1.4545 A
U Cell voltage	0.65 V
Back pressure P	1.01 Bar.a

During the first 15 seconds both models show low to zero error in the approximation of the original nonlinear model. In this time frame all the models have the same output. After the step change, the anode parameter-dependent reference model (5 states) and the cathode parameter-dependent reference model (10 states) clearly register the change in temperature an remain accurate, as temperature deviations from the design setpoint 70° are taken into account. The reference models obtained through classic balance truncation techniques present a certain offset, as expected, even though they are designed to have a higher order (15 states in the anode reference model and 20 in the cathode reference model), in order to cope with temperature variations.

(a) Anode   (b) Cathode
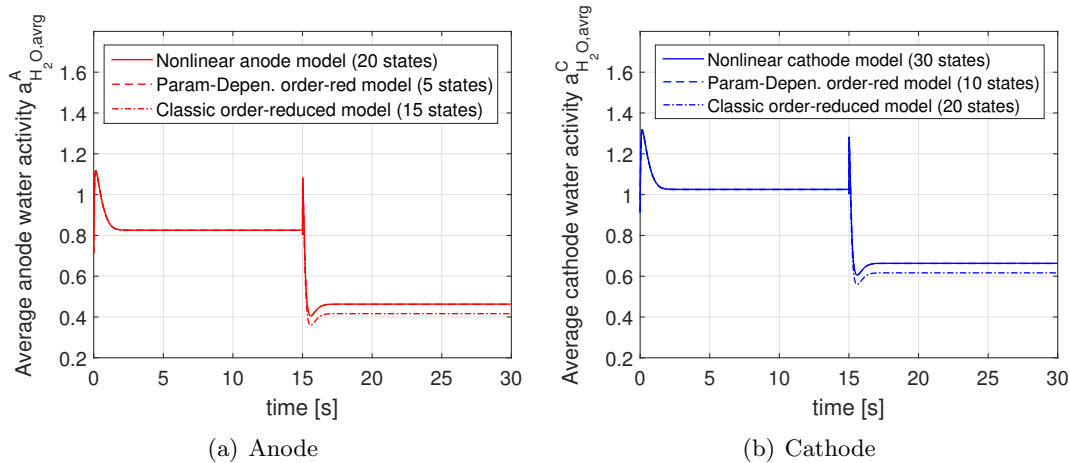
Figure 7.3: Outputs of reference models obtained with different order-reduction techniques vs. corresponding nonlinear fuel cell model outputs. Comparative under a temperature step change.

7.6   Conclusions

Satisfactory results have been found by applying two order reduction techniques to complex distributed parameter models of the anode and cathode. Classic balance truncation consists of finding the controllability and observability functions of the original nonlinear model, computing a change of coordinates to obtain a balanced realization that reveals the important states, and truncating less important states to approximate the original model.

A variation of the balance truncation technique from the recent literature has also been used. This technique is an algorithm to obtain a reduced order model which incorporates a symbolical parameter through a polynomial of arbitrary degree. In this procedure, each step of the balanced realization technique is solved in powers of the symbolical parameter. For the last step, which involves a singular value decomposition (SVD), only explicit expressions up to second order corrections are provided. In summary, results have shown that reducing the order of the distributed parameter submodels of the anode and cathode, from 20 and 30 states down to 5 and 10 states respectively, gives a very good approximation. The work in this chapter generated the following contributions:

Journal papers

- M.L. Sarmiento-Carnevali, M. Serra, C. Batlle, Decentralised distributed parameter model predictive control of water activity for performance and durability enhancement of a PEM fuel cell, submitted to the Journal of Power Sources, May 2017.

National and international conference papers

- M.L. Sarmiento-Carnevali, C. Batlle, M. Serra, I. Massana, Distributed parameter PEMFC model order reduction, Libro de Comunicaciones del Congreso Iberoamer-

icano de Hidrogeno y Pilas de Combustible (Iberconappice 2014), October 15-17th, 2014, Bellaterra, Catalonia.

- M.L. Sarmiento-Carnevali, C. Batlle, I. Massana, M. Serra, Order reduction of a distributed parameter PEM fuel cell anode gas channel model, Proceedings of the European Hydrogen Energy Conference (EHEC 2014), March 12-14th, 2014, Seville, Spain.

The following chapter uses the results obtained in this work to develop novel decentralised distributed parameter model predictive control strategies of water activity and concentration of reactants, for performance and durability enhancement of a PEM fuel cell.

Chapter 8

Distributed parameter control of PEM fuel cells

Water management is still a key challenge for optimal performance and durability of polymer electrolyte membrane (PEM) fuel cells. Water levels along the channel in a PEM fuel cell present important spatial variations that should be taken into account to avoid both local flooding and local drying. The purpose of this chapter is to design and implement a decentralised water activity control strategy based on two distributed parameter model predictive controllers. One of the controllers focuses on the anode side and the other focuses on the cathode side.

The aim of the strategy is to monitor and control observed water spatial profiles on both sides of the membrane to appropriate levels. These target values are carefully chosen to combine proper membrane, catalyst layer and gas diffusion layer humidification, whilst the rate of accumulation of excess liquid water is reduced. The key objective of this approach is to decrease the frequency of water removal actions that cause disruption in the power supplied by the cell, increased parasitic losses and reduction of cell efficiency [84]. A variation of this water activity control strategy, which includes the control of spatial distribution of reactants in the fuel and air channels, is also presented and analysed.

The first sections of the chapter present a compact literature review of control approaches in the PEM fuel cell field and a brief introduction to model predictive control. Section 8.3 describes in detail the proposed decentralised control schemes. Section 8.6 shows control results for different variables in challenging test scenarios for water management. In this section, the proposed spatial control scheme is compared to a traditional feed-forward inlet gas humidification strategy. The different variations of the control strategy are also analysed. Finally, section 8.7 presents concluding remarks.

8.1 Brief review of PEM fuel cell control approaches

In the last two decades, most of the control approaches presented have been linear and nonlinear controllers for lumped parameter models. Considerable progress has been made in order to avoid starvation and overheating of the fuel cell, regulate power output and manage temperature control [97, 7, 11, 37, 112, 78, 104, 100]. The understanding and the control of the water transport are more difficult, especially if the parallel presence of liquid water and water vapour inside the cell is considered.

In the area of water management control, most of the approaches presented are also based on lumped parameter models. Manipulation of the operating conditions is a very common strategy to mitigate flooding. These approaches include: increasing cathode gas flow rate well above stoichiometric levels to remove water through evaporation and advection [64, 99, 70], flushing the cathode periodically with momentarily high air flow rate [53, 70], increasing gas temperature [32], creating a coolant temperature gradient [9], and employing reactant gas counter-flow operation [38]. This class of strategies often cause significant parasitic losses that are directly linked to pressure, volume flow rate and pressure drop, or a increased system complexity.

In addition, the controllers for temperature and humidity are not integrated with current water management control designs. Moreover, it has not been studied how to operate the fuel cell to enhance performance and mitigate mechanisms of degradation. In summary, the proposed controllers do not take advantage of the complexity of the PEM fuel cell and all degrees of freedom that it offers. The main reason is the complexity of the controllers also increases by using single cell 1-D, 2-D or 3-D distributed parameter models.

There are very few works that can be found in the literature regarding distributed parameter model-based control. In 2007, Methekar et al. presented a dynamic analysis and linear control strategies for proton exchange membrane fuel cell using a distributed parameter model [66]. In this case, a linear ratio control strategy and a MIMO control strategy were presented. The control objectives were the average power density and the solid temperature. This work showed that, by choosing the proper manipulated variables, the PEM fuel cell did not exhibit sign change in gain and hence could be controlled by a linear controller. Both control strategies developed were able to deal with oxygen starvation. However, the control targets still did not exploited the capabilities of the model.

In the recent years, a few studies on nonlinear control of PEM fuel cells have been conducted. Nonlinear controllers present several advantages for fuel cell systems, given the intrinsic nonlinearities of the system under study. Moreover, these kind of controllers can guarantee stability of the closed-loop system over a wide range of operation conditions. Strategies such as nonlinear model predictive control, sliding mode control and passivity based control have been applied to fuel cell systems. Very few of this strategies have been designed for distributed parameter models.

In 2010, an sliding mode controller for the air supply system of a PEM fuel cell was

developed by Garcia-Gabin et al. [107] on a medium size PEM fuel cell showing successful performance. The objective required a fast response of the control scheme in order to avoid oxygen starvation during load changes and this controller showed the ability to deal with load changes rapidly for all the operation range. The sliding mode structure gives the possibility of swiftly tracking different loads without increasing the computational effort.

In the same year, Mangold [63] published one important work in the field of distributed parameter control. In this work a passive controller was presented that was able to keep the water content and the temperature of a PEM fuel cell on constant levels under changes of the electrical load. The controller was tested in simulations and compared with conventional linear control approaches such as a linear LQ optimal controller that was developed for comparison purposes. This controller showed to be able to handle fast load changes. However, the control target was not clearly established to target PEM fuel cell challenges like flooding or proper membrane humidification. Moreover, it was not studied how to operate the fuel cell to enhance performance and mitigate mechanisms of degradation (integrated control of different targets).

Despite several authors having demonstrated the importance of spatial variations of certain variables in PEM fuel cells, not many works available in the literature target the control of spatial profiles. Most control-oriented designs use lumped-parameter models because of their simplicity and convenience for controller performance. Throughout the rest of this chapter, novel decentralised distributed parameter model predictive control strategies of water activity and concentration of reactants, for performance and durability enhancement of a PEM fuel cell are designed, implemented and analysed.

8.2   Introduction to model predictive control

Model predictive control (MPC) is part of the family of the optimisation-based control methods that use on-line optimisation for future control steps. An MPC controller uses a reference model to predict system response. It can therefore be used to estimate future states and set the actuators accordingly, improving convergence time and avoiding oscillations in controlled and manipulated signals [19]. Clearly, there is a trade-off between the accuracy of the reference model and the computational complexity of the controller.

The optimiser predicts the effect of past inputs on future outputs. The number of predicted output steps is called the prediction horizon. The overall objective of this process is to compute a sequence of future control moves that minimises a certain cost function, which includes penalties on the trajectory of predicted tracking error. The number of steps in the sequence of future control moves is the control horizon. Once estimated, the first step of the sequence is applied and the entire optimisation is repeated from the next step onwards. The size of the steps is known as sampling time of the controller.

Output feedback is used to ensure convergence of the controller and to account for po-

tential reference model inaccuracies. The optimisation can be constrained or unconstrained according to the characteristics of the plant to be controlled and the hardware requirements of the manipulated variables. Extended details on the MPC control approach can be found in Appendix B and a comprehensive formal review of this topic is available in [19]. The use of MPC in this work, being a classic model-based approach, allows the consideration of spatial variations of water activity and other variables by using distributed parameter models as reference models.

8.3   Decentralised control of water activity spatial profiles

Figure 8.1 depicts the proposed decentralised control scheme. The decentralised feature consists of two distributed parameter model predictive controllers. One of the controllers focuses on the anode side and the other focuses on the cathode side. Each controller uses an order-reduced reference model derived from the non-linear PEM fuel cell model previously developed. Two model order reduction techniques are considered to decrease the complexity of the non-linear submodels of anode and cathode. The resulting order-reduced reference models are linear with adaptive features.

The system to be controlled is the single PEM fuel cell inside the dashed box, represented by the non-linear distributed parameter model described in Chapter 5. There are 6 inputs to the cell: the voltage U, according to a certain duty cycle, the cooling temperature input that is assumed to be taken care of by a dedicated temperature control loop outside the scope of this control scheme, the hydrogen inlet flux $\dot{n}_{H_2,in}^A$ and the anode water inlet flux $\dot{n}_{H_2O,in}^A$, which are manipulated variables of the anode MPC, the oxygen/nitrogen inlet flux $\dot{n}_{air,in}^C$ and the cathode water inlet flux $\dot{n}_{H_2O,in}^C$, which are manipulated variables of the cathode MPC.

The model measured outputs are the cell current I and temperature T. The observed outputs are the water activity profiles on the catalyst layers of the anode $a_{H_2O,k}^A$ and the cathode $a_{H_2O,k}^C$. These are the controlled variables (red-coloured in Figure 8.1). The gas fluxes through the cell are also estimated: $\dot{n}_{H_2,k}^A$, $\dot{n}_{H_2O,k}^A$, $\dot{n}_{air,k}^C$ and $\dot{n}_{H_2O,k}^C$, as these profiles are required by the MPC controllers.

The overall control targets of the strategy are (1) to supply the required inlet gas flow according to defined system stoichiometry, (2) to reduce the rate of accumulation of liquid water on the catalyst and other backing layers, and (3) to prevent local drying on the membrane or catalyst layers of the anode and cathode, in order to ensure proper membrane protonic conductivity and adequate conditions for the electrochemical reactions to occur. Note that the fuel cell stoichiometry is not actively controlled, but it is hard-coded in the controllers as a constraint of the manipulated variables related to reactants inlet, according to current drawn from the cell.
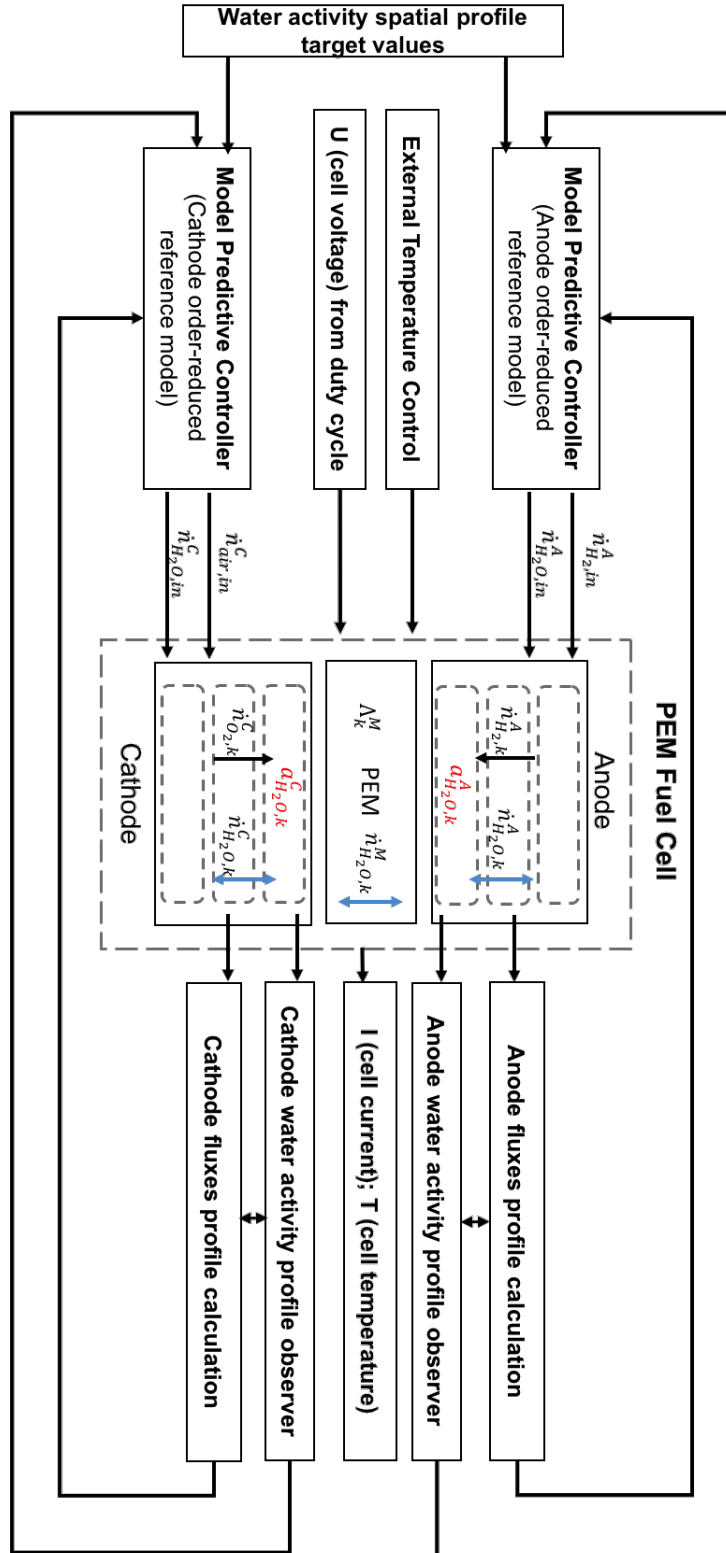
Figure 8.1: Decentralised distributed parameter model predictive control of water activity

The following sub-sections describe the design and implementation process of this control scheme.

8.3.1   Design of reference models for the predictive controllers

The first step in designing the MPC controllers for the current scheme is to define the reference models for the anode and cathode. Non-linear sub-models for the anode layers and cathode layers were derived from the discretised non-linear model introduced in Chapter 5. The sub-models are represented by corresponding equations (5.4-5.27) and (5.40). Both models consider ordinary differential equations (ODE) and algebraic equations. Differential algebraic equations (DAE) systems resulting from discretisation of distributed parameter models normally have a large number of equations as appreciated in Chapter 5. As indicated in previous chapters, the z-direction of the model has been discretised in 10 segments using the central finite differences approach.

Usually spatial variations are neglected and simplified lumped-parameter models are considered as reference models in control applications, in order to achieve a trade-off between accuracy of the model and computational complexity. However, the spatial profile behaviour is the focus of the control strategies in this work, therefore order-reduced models are used as simplified reference models of the anode and cathode. Chapter 7 presented the details of the model order reduction algorithms applied to decrease the complexity of the non-linear sub-models. Two techniques are considered, namely classic balance truncation and a variation of this approach recently available in the literature, which includes adaptive features in the resulting reduced model. Corresponding model variables (before order reduction) are:

<u>Anode sub-model</u>

- States (x_1 vector): $c_{H_2,k}^A$ and $c_{H_2O,k}^A$ ($k = 1..10$),

- Algebraic variables (x_2 vector): p_k^A and v_k^A ($k = 1..10$),

- Inputs (u vector): hydrogen inlet flux $\dot{n}_{H_2,in}^A$ and water inlet flux $\dot{n}_{H_2O,in}^A$,

- Outputs (y vector): water activity in segments $a_{H_2O,1}^A$, $a_{H_2O,6}^A$, $a_{H_2O,10}^A$ and average water activity level $a_{H_2O,avrg}^A$ of the profile along the z-direction.

<u>Cathode sub-model</u>

- States (x_1 vector): $c_{O_2,k}^C$, $c_{N_2,k}^C$ and $c_{H_2O,k}^C$ ($k = 1..10$),

- Algebraic variables (x_2 vector): p_k^C and v_k^C ($k = 1..10$),

- Inputs (u vector): air inlet flux $\dot{n}_{O_2,in}^C$, $\dot{n}_{N_2,in}^C$ and the cathode water inlet flux $\dot{n}_{H_2O,in}^C$,

- Outputs (y vector): water activity in segments $a_{H_2O,1}^C$, $a_{H_2O,6}^C$, $a_{H_2O,10}^C$ and average water activity level $a_{H_2O,avrg}^C$ of the profile along the z-direction.

The outputs are defined as key variables of the water activity profiles of the anode and cathode catalyst layer, i.e. the water activity in the first, middle and last mesh segments. Results shown in Section 8.6 indicate that these three outputs provide enough information to monitor and control the overall water activity profiles. The model has the form

$$
\begin{aligned}
F_1\left(\dot{x}_1, x_1, x_2, u\right) &= 0, \\
F_2\left(x_1, x_2, u\right) &= 0, \\
y - h\left(x_1, x_2, u\right) &= 0,
\end{aligned}
\tag{8.1}
$$

where $x_1 \in \mathbb{R}^d$ is the state vector, $x_2 \in \mathbb{R}^a$ is the vector of algebraic variables, $u \in \mathbb{R}^r$ is inputs vector, and $y \in \mathbb{R}^q$ is the outputs vector. In addition, the DAE model has an underlying ODE description,

$$
\begin{aligned}
\dot{x}_1 &= \mathcal{L}\left(x_1, x_2, u\right), \\
x_2 &= \mathcal{R}\left(x_1, u\right),
\end{aligned}
\tag{8.2}
$$

therefore, it follows that

$$
\begin{aligned}
\dot{x}_1 &= \mathcal{L}\left(x_1, \mathcal{R}\left(x_1, u\right), u\right), \\
y &= h\left(x_1, \mathcal{R}\left(x_1, u\right), u\right).
\end{aligned}
\tag{8.3}
$$

After both sub-models are completely defined, balanced truncation is used to reduce their order. The resulting reference models of the anode and cathode after the application of this method are linear time-invariant models of the form

$$
\begin{aligned}
\dot{z}_a &= A_{red} z_a + B_{red} u, \\
y &= C_{red} z_a,
\end{aligned}
\tag{8.4}
$$

where $z_a \in \mathbb{R}^k$ is the state vector, $u \in \mathbb{R}^r$ are the control inputs and $y \in \mathbb{R}^q$ are the outputs. Note that the new set z_a of states has no physical meaning since it is a linear combination of the full order set of states. The inputs and outputs remain the same and, ideally, the internal dynamics of the reduced order model preserves the input-output relation of the original DAE. Corresponding model inputs and outputs after order reduction are:

<u>Anode order-reduced model</u>

- Inputs (u vector): hydrogen inlet flux $\dot{n}_{H_2,in}^A$ and anode water inlet flux $\dot{n}_{H_2O,in}^A$.

- Outputs (y vector): water activity in segments $a_{H_2O,1}^A$, $a_{H_2O,6}^A$, $a_{H_2O,10}^A$ and average water activity level $a_{H_2O,avrg}^A$.

<u>Cathode order-reduced model</u>

- Inputs (u vector): air inlet flux $\dot{n}_{O_2,in}^C$, $\dot{n}_{N_2,in}^C$ and cathode water inlet flux $\dot{n}_{H_2O,in}^C$.

- Outputs (y vector): water activity in segments $a^C_{H_2O,1}$, $a^C_{H_2O,6}$, $a^C_{H_2O,10}$ and average water activity level $a^C_{H_2O,avrg}$.

8.3.2   Parameter-dependent reference models

It is well known that linear model-based controllers present some deficiencies. The non-linearities of the controlled systems reduce the performance of controllers under certain operating conditions, and similarly, performance optimisation is only effective under certain operating conditions. In this work, a variation of the balanced truncation technique is also used to increase the accuracy of the linear reference models. This method has been published recently [14] and the procedure is similar to the sequence of steps followed to obtain the model (8.4).

The result of this technique is an order-reduced model that incorporates the effects of changes in important external variables. Applying this method, the modified reference models consider a parameter m that accounts for temperature deviations from the equilibrium operating point used in the linearisation step. This parameter is considered as a measured disturbance to the MPC controllers. The reduced models have the form

$$
\begin{aligned}
\dot{z}_a &= A_{red}\left(m\right) z_a + B_{red}\left(m\right) u, \\
y &= C_{red}\left(m\right) z_a.
\end{aligned}
\tag{8.5}
$$

Corresponding model inputs and outputs after order reduction are:

Anode parameter-dependent order-reduced model

- Inputs (u vector): hydrogen inlet flux $\dot{n}^A_{H_2,in}$ and anode water inlet flux $\dot{n}^A_{H_2O,in}$.

- Disturbances: temperature deviations given by changes in parameter m (in parameter-dependent matrices).

- Outputs (y vector): water activity in segments $a^A_{H_2O,1}$, $a^A_{H_2O,6}$, $a^A_{H_2O,10}$ and average water activity level $a^A_{H_2O,avrg}$.

Cathode parameter-dependent order-reduced model

- Inputs (u vector): air inlet flux $\dot{n}^C_{O_2,in}$, $\dot{n}^C_{N_2,in}$ and cathode water inlet flux $\dot{n}^C_{H_2O,in}$.

- Disturbances: temperature deviations given by changes in parameter m (in parameter-dependent matrices).

- Outputs (y vector): water activity in segments $a^C_{H_2O,1}$, $a^C_{H_2O,6}$, $a^C_{H_2O,10}$ and average water activity level $a^C_{H_2O,avrg}$.

Details of the resulting reference models and a comparison study of the two model order reduction techniques used in the design of proposed control strategies were presented in Chapter 7. Figure 8.2 shows the decentralised strategy considering parameter-dependent reference models.

8.3.3 Setting up the MPC optimisation problem

Once the reference models are established, the next step in the design of the MPC controllers is to define the cost function and corresponding constraints. The objective function for the MPC controller is the minimisation of the sum of squared errors between the desired set point and the actual trajectory of system output, with an additional penalty imposed on rapid changes in the manipulated variables,

$$
f\left(u\right) = \int_0^{t_h} \left[W\left(y\left(u,t\right) - y_{set}\left(t\right)\right)^2 \sum_i S_i \left(\frac{\partial u_i}{\partial t}\right)^2 \right] dt. \tag{8.6}
$$

The weight functions, W and S, are used to increase the importance of specific control objectives. The function is discretised over time, obtaining the following algebraic function

$$
f\left(u\right) = \left(y\left(u\right) - y_{set}\right)^T W \left(y\left(u\right) - y_{set}\right) + \sum_i du_i^T S_i du_i. \tag{8.7}
$$

The vector $y\left(u\right)$ is the value of the outputs at the different time steps in the prediction horizon, while element i of vector du is the value of u at time step i minus its value at time step $i-1$. Note that the actual variables in the optimisation are the changes in values from each time step to the next. This means that the value u at time step i is simply the initial value of u plus all the values of du up to time step i. The constraints depend on the upper and lower level values of the manipulated variables, as well as the physical limitations imposed by model assumptions. In this subsection the sub-index i is used to account for time steps.

Design of the cost function

Each MPC has two targets: (i) to provide the correct amount of reactant gases and (2) to maintain proper membrane protonic conductivity and adequate conditions for the electrochemical reactions to occur, whilst reducing the rate of formation and accumulation of liquid water using the knowledge from observed water activity spatial profile results. The overall idea of the MPC controller in this strategy is to efficiently manage the inlet water humidification on both anode and cathode, taking full advantage of the drag and back diffusion fluxes.

Membrane hydration levels are controlled through the water activity setpoints. These setpoints are defined using a previous analysis of the polymer behaviour presented in [85]. This approach is:
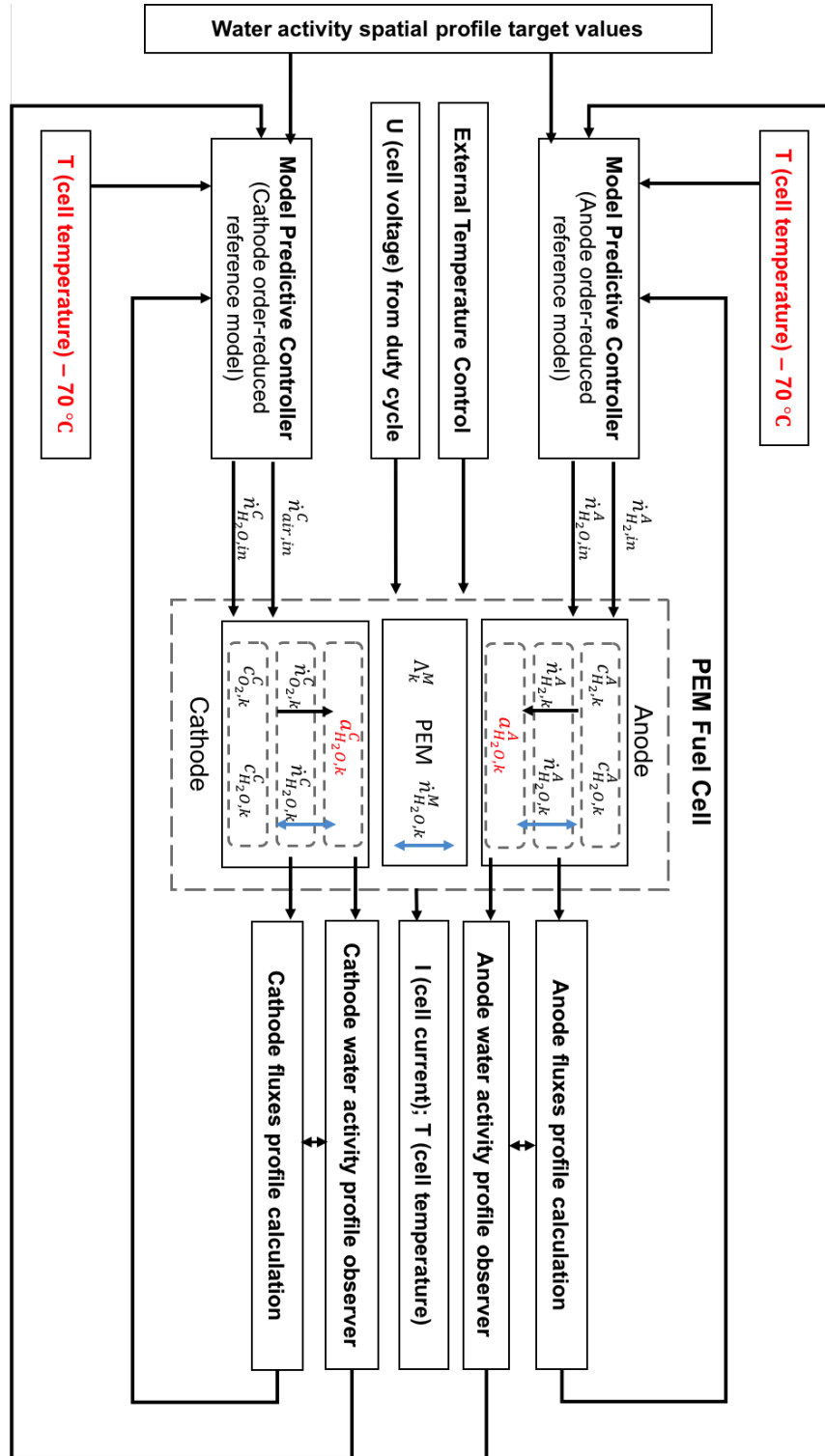
Figure 8.2: Decentralised distributed parameter model predictive control of water activity with parameter-dependent reference models in the MPC controllers

- Upon high current levels ($\geqslant 0.5$ A cm^{-2}), anode and cathode catalyst layer water activity setpoints are increased closer to condensation values (0.8. to 1). Using these values the membrane water content is kept within 14 to 22.

- During lower current levels (< 0.5 A cm^{-2}), anode and cathode catalyst layer water activity setpoints are set to vapour water region values (0.6. to 0.79). Using these values the membrane water content is kept within 8 to 14.

The objective of this setpoint selection approach is to avoid condensation when it is possible to keep the water activity in the vapour region, without affecting the membrane protonic conductivity at different current levels. Table 8.1 presents the different elements in the cost function of each MPC controller.

Prediction and control horizons for each MPC are 2 and 0.6 seconds respectively. Sampling time is 0.2 seconds. The controller tunning method is described in [19]. Several approaches presented in this reference were tested to guarantee best performance.

8.3.4 Design of observers

An MPC requires measured output feedback to ensure convergence towards target setpoints. However, some of the chosen outputs are very difficult to measure, such as internal values of the water activity profile on each side of the membrane. In fact, spatial variations of water activity and most internal profiles of fuel cell variables are almost impossible to measure by sensors and, if possible, the increase in cost is not desirable given the technology challenges.

In order to address this issue, state observers are designed for both the anode and cathode models to estimate the water activity profile. As the water activity profile is part of the set of algebraic variables, the first step to estimate this profile is to observe the concentration of species on both the anode and cathode channels (5.4). After estimating these states, the water activity profiles are computed using algebraic equations (5.11) and (5.40). In this work only linear observers are designed and implemented. This decision is based on the desire to keep the control system as simple as possible maintaining the main control objectives.

A state observer estimates the state variables based on measured outputs and control variables. Observers can be derived if and only if the system is observable. A system is said to be completely observable if state $x(t_0)$ is determined from $y(t)$ during a finite time frame, $t_0 <= t <= t_1$. Therefore, the system is completely observable if all state transitions eventually affect all the elements of the output vector. Detailed information on observers and the observability concept can be found in [72].

Consider the system given by equation (8.4). An observer is a linear system itself. The mathematical model of an observer is almost the same as the model of the system under study, except for an additional term that accounts for the estimation error to compensate inaccuracies of matrices A and B and the lack of initial error. The estimation error or

Table 8.1: Anode and Cathode MPC design

Anode MPC		
Var.	Description	Comments
$\dot{n}_{H_2,in}^A$	Manipulated variable. Range of H_2 stoichiometry values from 1.5 to 2	Corresponding weight is 10, which accounts for high penalisation upon changes from 1.5. Changes are only allowed in low temperature conditions to increase anode pressure.
$\dot{n}_{H_2O,in}^A$	Manipulated variable. Range of %RH values from 10 to 85	Corresponding weight is 0, which indicates no penalisation upon changes.
$a_{H_2O,k}^A$	Controlled variable	Three segments are considered $k = 1$, 6 and 10. Restricted from 0.2 to 1 with 0.3 weight value indicating flexible setpoint
$a_{H_2O,avrg}^A$	Controlled variable	Restricted from 0.65 to 1 with weight value 1 indicating high priority to meet setpoint defined by current level
$\dot{n}_{H_2,k}^A$	Estimated disturbance	The complete 10-element profile is consider a known disturbance as it is computed from the anode observer results
$\dot{n}_{H_2O,k}^A$	Estimated disturbance	The complete 10-element profile is consider a known disturbance as it is computed from the anode observer results
Cathode MPC		
$\dot{n}_{air,in}^C$	Manipulated variable. Range of O_2 stoichiometry values from 2 to 3	Corresponding weight is 10, which accounts for high penalisation upon changes from 2. Changes are only allowed in low temperature conditions to increase cathode pressure.
$\dot{n}_{H_2O,in}^C$	Manipulated variable. Range of %RH values from 10 to 85	Corresponding weight is 0, which indicates no penalisation upon changes.
$a_{H_2O,k}^C$	Controlled variable	Three segments are considered $k = 1$, 6 and 10. Restricted from 0.2 to 1 with 0.3 weight value indicating flexible setpoint
$a_{H_2O,avrg}^C$	Controlled variable	Restricted from 0.65 to 1 with weight value 1 indicating high priority to meet setpoint defined by current level
$\dot{n}_{O_2,k}^C$	Estimated disturbance	The complete 10-element profile is consider a known disturbance as it is computed from the anode observer results
$\dot{n}_{H_2O,k}^C$	Estimated disturbance	The complete 10-element profile is consider a known disturbance as it is computed from the anode observer results

observation error is the difference between the measured output and the estimated output. The initial error is the difference between the initial state and the initial estimated state. The mathematical model of the observer design is then

$$\tilde{x}_1 = A\tilde{x}_1 + Bu + K_e(y - C\tilde{x}_1) \tag{8.8}$$

$$= (A - K_e C)\tilde{x}_1 + Bu + K_e y \tag{8.9}$$

where $\tilde{x}_1$ is the estimated state and $C\tilde{x}$ is the estimated output. The inputs of the observer are the system output y and the system control inputs u (manipulated variables). The matrix K_e, known as the *observer gain matrix*, is a weight matrix for the correction term that involves the difference between the measured output and the observed output $C\tilde{x}$. This term continually corrects the observer output improving its behaviour.

Figure 8.3 shows the performance of both anode and cathode observers. For simplicity, only the average water activity is presented. Step changes in voltage, from 0.65 V to 0.55 V at 0.1 s and from 0.55 V to 0.75 V at 0.3 s, are used to test observer robustness. It can be seen that the observer error converges to zero shortly before 0.1 seconds, which is half the sampling time of the MPC controllers. This condition is desirable to ensure the observer is faster than the controller and accurate predictions are fed into the optimisers.
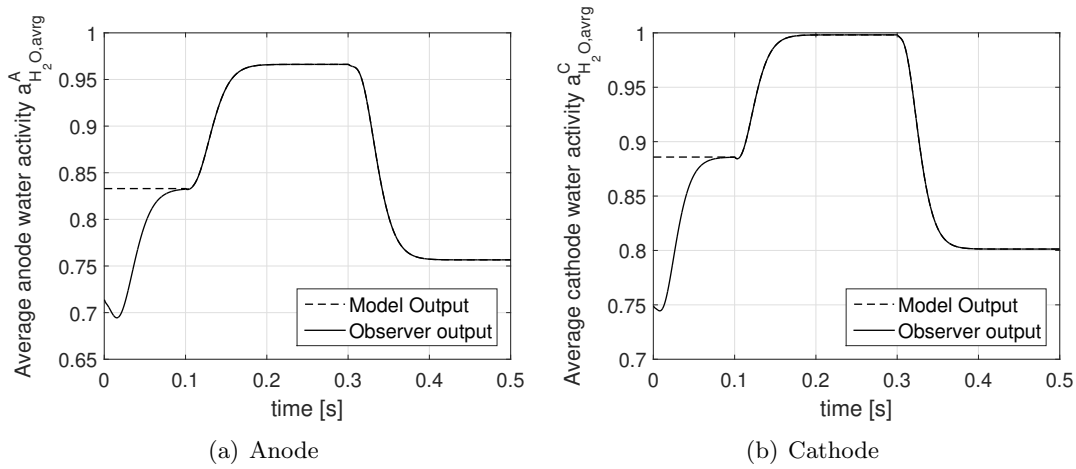
(a) Anode

(b) Cathode

Figure 8.3: Anode (a) and cathode (b) observer outputs vs. corresponding nonlinear fuel cell model outputs under voltage step changes

It is also necessary to estimate the variables $\dot{n}^A_{H_2,k}$, $\dot{n}^A_{H_2O,k}$, $\dot{n}^C_{O_2,k}$, $\dot{n}^C_{N_2,k}$ and $\dot{n}^C_{H_2O,k}$ ($k = 1..10$). The same approach is used for this estimation. Once the state observation is accomplished, algebraic equations (5.34-5.38) are used to calculate corresponding variables.

8.4   Decentralised control of reactants concentration spatial profiles

The main objective of this control approach is to avoid starvation of reactants in both anode and cathode catalyst layers. This is achieved by controlling the concentration of reactants in the outlet end of the gas channels. The control target is to prevent zero or negative concentration values. Higher levels of reaction rate occur towards the gas inlet end of the channels where reactants partial pressure is higher. Therefore, the last segments along the z-direction are more vulnerable to starvation. However, starvation could occur anywhere along the flow direction due to the presence of liquid water or degradation issues, which

makes a spatial control approach the proper to prevent such problems. Figure 8.4 shows the scheme of this control strategy highlighting control design variations.

In this study, only concentrations in the last mesh segment (number 10) of the anode and cathode gas channels are controlled. This target is achieved by including a constraint in the MPC optimisation process to prevent concentration variables from reaching zero values. Table 8.2 shows the variations included in the previous design of both controllers in order to implement this strategy. The same approach could be implemented for the control of the concentrations in any other segment or various segments along the gas channels.

Table 8.2: MPC design variation to implement control of gas concentrations

Anode MPC design changes		
Var.	Description	Comments
$\dot{n}_{H_2,in}^A$	Manipulated variable. Range of stoichiometry values from 1.5 to 2	Corresponding weight is 10, which accounts for high penalisation upon changes from 1.5. Changes are only allowed in low temperature conditions to increase anode pressure or to meet hydrogen concentration setpoint target towards channel outlet.
$c_{H_2,10}^A$	Controlled variable	Channel outlet hydrogen concentration restricted to have positive values only
Cathode MPC design changes		
$\dot{n}_{air,in}^C$	Manipulated variable. Range of stoichiometry values from 2 to 3	Corresponding weight is 10, which accounts for high penalisation upon changes from 2. Changes are only allowed in low temperature conditions to increase cathode pressure or to meet oxygen concentration setpoint target towards channel outlet.
$c_{O_2,10}^C$	Controlled variable	Channel outlet oxygen concentration restricted to have positive values only

8.5   Definition of control strategies

Three different decentralised distributed parameter model predictive control (DPMPC) strategies were implemented considering the steps presented in section 8.3. Summary and most relevant features are:

- **DPMPC-1**: this strategy is focused on the control of observed water activity profiles along the z-direction of the anode and cathode catalyst layers, as well as hydrogen and oxygen stoichiometry levels. The MPC controllers have parameter-dependent reference models presented in section 8.3.2. Spatial control of observed reactant concentrations is not included.

- **DPMPC-2**: this strategy is focused on the spatial control of water activity profiles along the z-direction of the anode and cathode catalyst layers, as well as spatial control of observed reactant concentrations in the last mesh segment. The MPC controllers have parameter-dependent reference models presented in section 8.3.2.
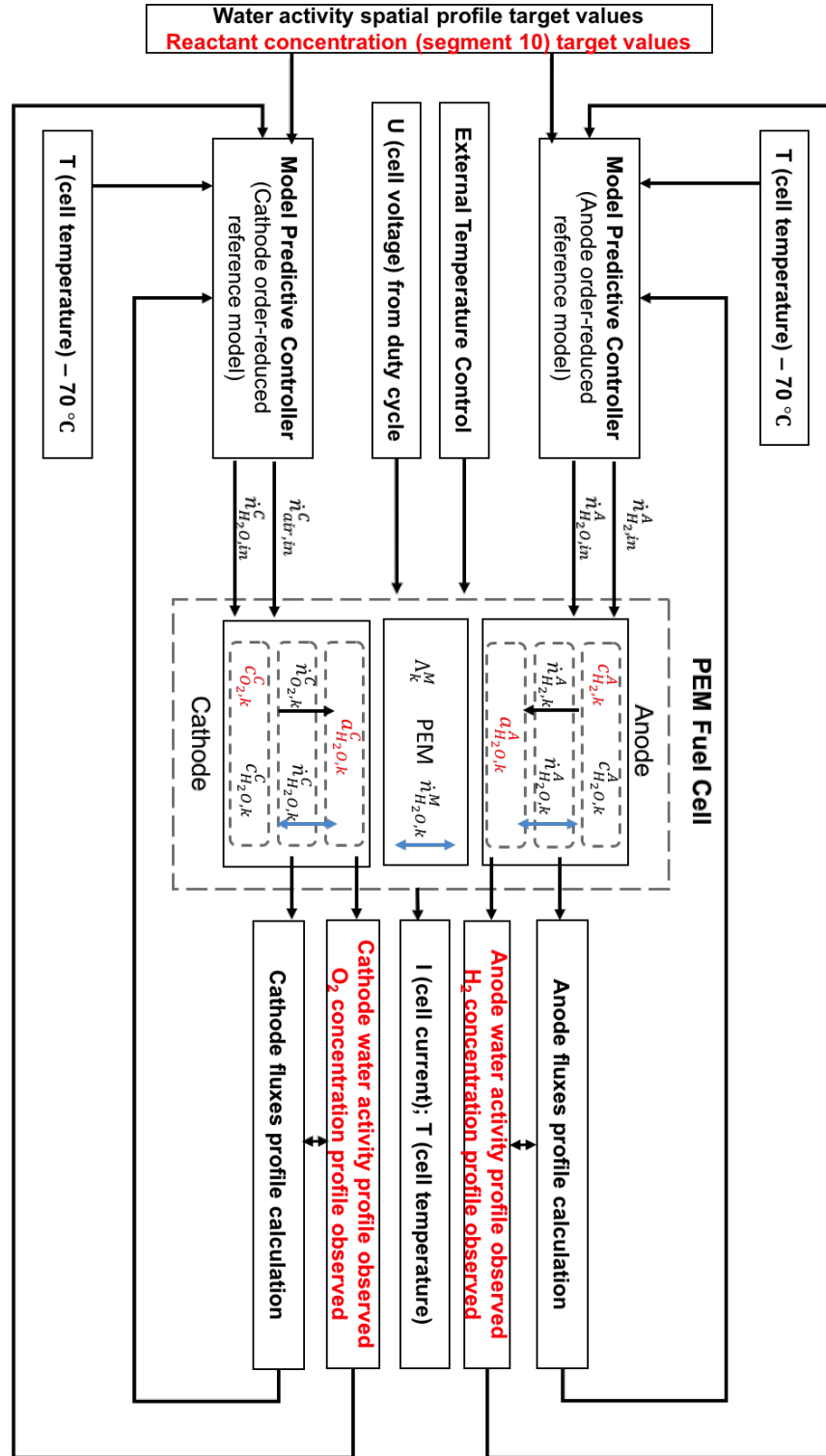
Figure 8.4: Decentralised distributed parameter model predictive control of water activity and concentration of reactants at channel outlet

- **DPMPC-3**: this strategy is focused on the spatial control of observed water activity profiles along the z-direction of the anode and cathode catalyst layers, as well as hydrogen and oxygen stoichiometry levels. The difference in comparison to DPMPC-1 is the use of classic balance truncation to design the reference models of the MPC controllers. Spatial control of observed reactant concentrations is not included.

8.6   Simulation results and discussion

The non-linear PEM fuel cell model and the three different control strategies presented in section 8.5 are analysed via simulation environment in MATLAB Simulink. Three tests have been designed. The first test focuses on the control of water activity profiles along the z-direction of the anode and cathode catalyst layers. The objective of this test is to compare DPMPC-1 to a classic inlet gas humidification strategy.

The second test focuses on the control of the concentration of reactants along the z-direction of the gas channels. The objective of this test is to compare DPMPC-1 vs. DPMPC-2. Finally, the third test aims at comparing the effect of parameter-dependent reference models in the performance of the overall control strategy. The objective of this test is then to compare DPMPC-1 vs. DPMPC-3.

8.6.1   Analysis of DPMPC-1 vs. classic inlet gas humidification control

This test compares the performance of DPMPC-1 to a traditional current-based humidification approach that fixes the anode inlet gas relative humidity to 50%, and the cathode inlet gas relative humidity to 30% for the different steps in a duty cycle. In this approach humidification increases or decreases with current according to the fixed stoichiometry. Such approach is the baseline humidification control strategy.

Transient-state results

A voltage cycle is designed including three different operating regions to test and analyse the performance of DPMPC-1. Figures 8.5, 8.6 and 8.7 show different results of this test. Figure 8.5(a) presents the voltage cycle under analysis. Voltage levels considered range from 0.55 V to 0.75 V, which correspond to 43.9% up to 59.9% low hydrogen heating value (LHV) fuel cell efficiency.

A square wave is chosen to assess the control performance upon step changes. Voltage value is updated every 5 seconds. This time frame is similar to average time for changes in duty cycles of applications like automotive (WLTP driving cycle, for example) [96], and allows the evaluation of control convergence. First operating point corresponds to $U = 0.65$ V, which is the average cell operating point (equilibrium point for MPC controllers design). Operating points $U = 0.55$ V and $U = 0.75$ V represent high and low currents respectively. Overall cell temperature is assumed to be kept around 70°C during the simulation. Total

cell current is shown in Figure 8.5(b). Table 8.3 shows the simulation parameters considered for this study.
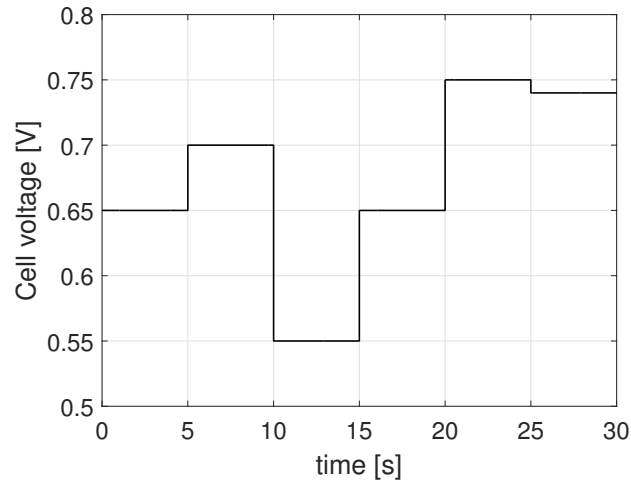
(a) Voltage cycle
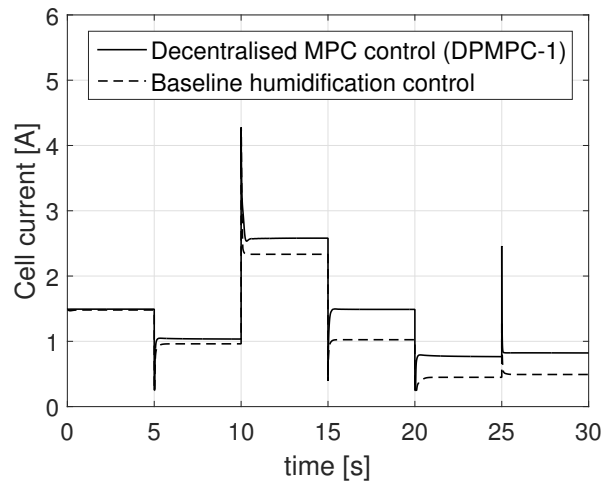
(b) Total current

Figure 8.5: Voltage cycle and total cell current - DPMPC-1 vs. Baseline humidification control strategy

Figures 8.6(a) and 8.6(b) indicate the average water activity level on anode and cathode sides of the membrane ($a^A_{H_2O,avrg}$ and $a^C_{H_2O,avrg}$), which are the controlled variables with highest weight in the optimisation process of each MPC controller. The impact of the proposed control strategy is appreciated in these two figures. Notice how the rate of condensation is delayed by DPMPC-1 in comparison to the baseline strategy at time = 10 s, by focusing on the observed water activity profile instead of maintaining a constant humidification level. The importance of observing the behaviour of the spatial profile of water is highlighted in this result.
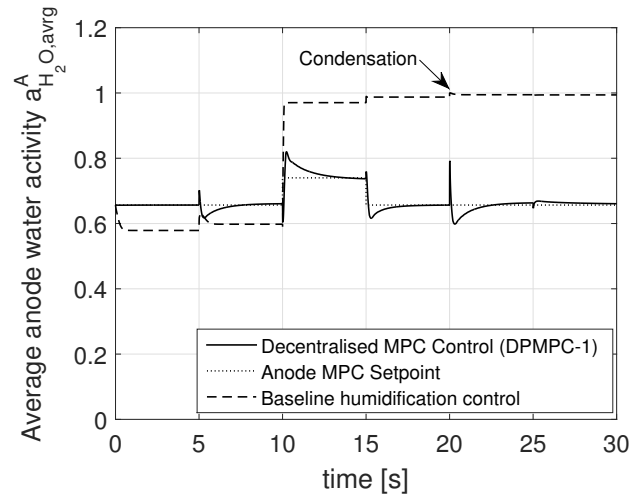
(a) Anode $a^A_{H_2O,avrg}$ (controlled var.)
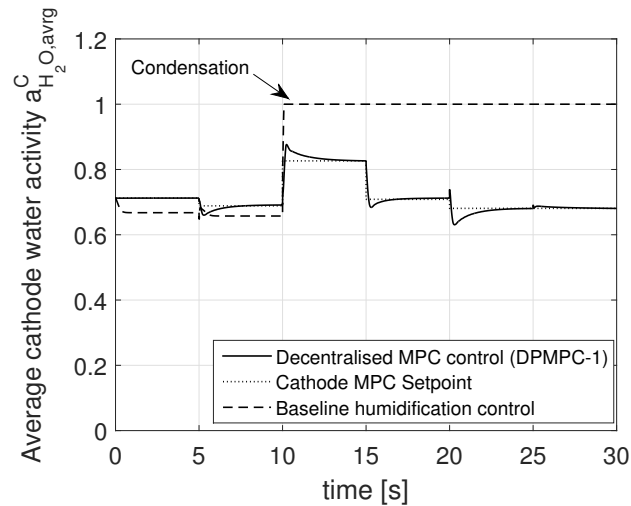
(b) Cathode $a^C_{H_2O,avrg}$ (controlled var.)

Figure 8.6: Controlled variables with priority in the optimisation process - Voltage Cycle - DPMPC-1 vs. Baseline humidification control strategy

Figures 8.7(a) and 8.7(b) show the behaviour of inlet fluxes of water in both anode and cathode explaining the difference in the humidification approach. During the first 10 seconds of the simulation, voltage steps 0.65 V and 0.7 V, both strategies behave similarly regarding cell performance. However, the baseline control strategy always inputs a certain amount of water to maintain a humidification level proportional to the current. Therefore, at this voltage levels the average water activity can even be less than DPMPC-1 setpoint. This action seems intuitively correct in the presence of normal to low current levels (around 0.3 A cm^{-2}), but it is also very likely that in these conditions local drying in the anode occurs if back diffusion levels along the z-direction are not sufficient to compensate water leaving the anode due to the electro-osmotic drag effect.
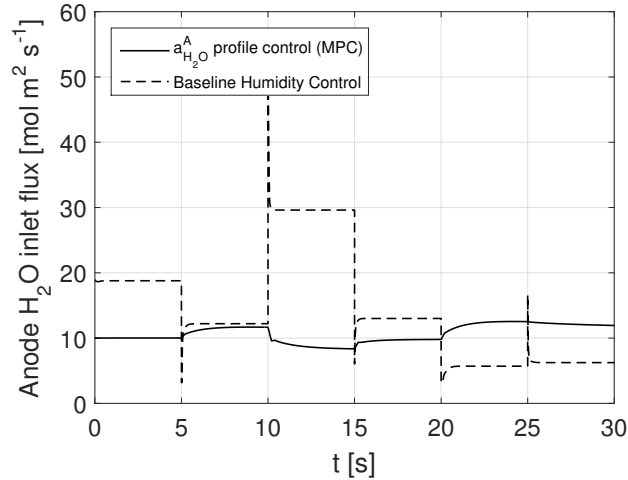
(a) Anode $a_{H_2O,in}^A$ (manipulated var.)
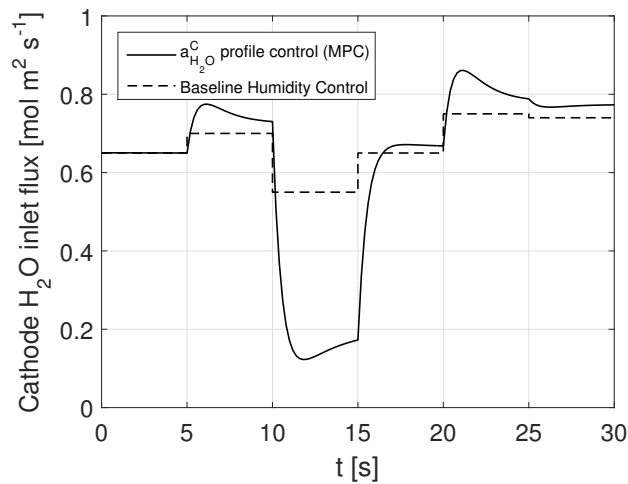
(b) Cathode $a_{H_2O,in}^C$ (manipulated var.)

Figure 8.7: Manipulated variables - Voltage Cycle - DPMPC-1 vs. Baseline humidification control strategy

Upon the step voltage 0.55 V at time = 10 s, the cell operates at high current levels (around 0.7 A cm^{-2}). Clearly, the rate of water generation on the cathode side is very high. In this scenario, DPMPC-1 is able to reduce the accumulation of liquid water by controlling the average water activity to take advantage of generated water, and the back diffusion effect, to properly humidify both the cathode and the anode. During these 5 seconds at high current level, the average water activity setpoints are adjusted to account for major increase in water generation and allow higher membrane humidification levels (as explained is Section 8.3.3).

This high current level scenario represents the most challenging task in water management. Excess of accumulated liquid water on the catalyst layers reduces access of reactants to the active platinum reaction sites (ECSA), and consequently reduces the cell perfor-

mance, in the worst case causing cell flooding, a major reason of cell failure. Several control systems consider different approaches for liquid water removal, however, the majority of these actions cause either a disruption in the power supplied by the cell, increased parasitic losses or reduction of cell efficiency [84]. The strategy DPMPC-1 reduces the rate of accumulated water on the catalyst layer decreasing the frequency of removal actions and mitigating cell flooding.

Figures 8.7(a) and 8.7(b) also show the behaviour of the manipulated variables during high current levels (time = 10 to 15 s). Both manipulated variables have around 5 seconds of settling time. The design parameters of each MPC defined in Section 8.3 prove to be adequate in order to ensure stability. The difference in each approach is clear from these figures. The baseline strategy changes the rate of inlet water flux on the anode and cathode gas channel inlet according to the current level, which is again intuitively a correct action as the electro-osmotic forces may cause dryness in the anode if not properly humidified. On the cathode side, this strategy registers the effect of generated water depending on current level. However, the baseline strategy aims to maintain a certain humidification level of the inlet gases that results in higher amount of inlet water than necessary leading to condensation on both sides of the membrane. Under low ambient temperature conditions, a traditional current-based humidification approach could increase the chances of local or total flooding, particularly on the anode side.

Notice how DPMPC-1 control action is able to maintain the average water activity level under 1 (Figures 8.6(a) and 8.6(b)), indicating less liquid water formation and reducing the effect of liquid water accumulation. Following the high current level scenario (beyond 15 s), the impact of DPMCP-1 on the performance of the fuel cell is clearly appreciated (Figure 8.5(b)). Decreased current levels due to the presence of liquid water are seen with the baseline strategy in comparison to DPMPC-1. At this point, most control strategies would trigger a liquid water removal action, like a blowdown or a purge to regain cell performance. Some of these strategies are triggered more or less frequently depending on the amount of current drawn from the cell [67]. The key result of Figure 8.5(b) is that the frequency of those strategies would be reduced with DPMPC-1. This is desirable since such water removal strategies cause disruption in the power supplied by the cell, increased parasitic losses and reduction of cell efficiency.

Steady-state results

The behaviour of controlled variables with less weight in the optimisation process ($a_{H_2O,1}^A$, $a_{H_2O,6}^A$, $a_{H_2O,10}^A$, and $a_{H_2O,1}^C$, $a_{H_2O,6}^C$, $a_{H_2O,10}^C$) is appreciated in Figures 8.8, 8.9 and 8.10. Figures 8.8(a) and 8.8(b) show-steady state values of the entire water activity spatial profile for both anode and cathode upon high current scenarios (time = 14 s). Liquid water formation is prevented in the anode and considerably decreased in the cathode with DPMPC-1. Condensation is observed at the gas outlet end of the z-direction where it is more chal-

Table 8.3: Simulation parameters

Symbol	Value
C^A	8.25 x 10^6 F m^{-3}
C^C	8.25 x 10^6 F m^{-3}
$CCSA$	$8.75.10^{-7}$ m^2
D_{H_2,H_2O}^{eff}	10^{-6} m^2 s
D_{O_2,H_2O}^{eff}	3 x 10^{-6} m^2 s
D_{O_2,N_2}^{eff}	2 x 10^{-6} m^2 s
D_{H_2O,N_2}^{eff}	2.5 x 10^{-6} m^2 s
δ^A	0.7×10^{-3} m
δ^{AC}	4×10^{-5} m
δ^C	0.7×10^{-3} m
δ^{GA}	0.34×10^{-3} m
δ^{GC}	0.34×10^{-3} m
δ^{CC}	1.1×10^{-4} m
δ^M	1.75×10^{-4} m
$ECSA$	0.0005 m^2
K^A	10^{-5} m^2 s^{-1} Pa^{-1}
K^C	10^{-4} m^2 s^{-1} Pa^{-1}
L_x	0.00125 m
L_z	0.4 m
p^{amb}	101325 Pa

lenging to control, as the partial pressure of water tends to be higher due to less reactants concentrations.

(a) High current density scenario t = 14 s   (b) High current density scenario t = 14 s

Figure 8.8: Steady-state results - Average water activity profiles - High current density scenario - DPMPC-1 vs. Baseline humidification control

In the presence of high current densities, sometimes it is also possible to see anode local drying due to increased electro-osmotic drag [84, 92]. The possibilities of this scenario are reduced by DPMPC-1 as it aims to maintain a healthy water activity level at the inlet

throughout the duty cycle. This preventive behaviour decreases the possibility of membrane drying and its degradation consequences.

Figures 8.9(a) and 8.9(b) correspond to water activity steady state results at low current levels along the z-direction (time $= 9$ s) for anode and cathode respectively. Notice how the anode water activity shows a tendency towards dryness in the first part of the catalyst layer. This condition occurs because current density is typically higher at channel inlet [43, 74], due to higher reactant partial pressure that results in larger electro-osmotic drag from the anode. Conversely, towards the end of the channel hydrogen partial pressure decreases and there is increased back diffusion of the water that has built up on the cathode. This impact is reduced by DPMPC-1 as it aims to maintain a healthier water activity level at the inlet, reducing the possibility of membrane drying and its degradation consequences.

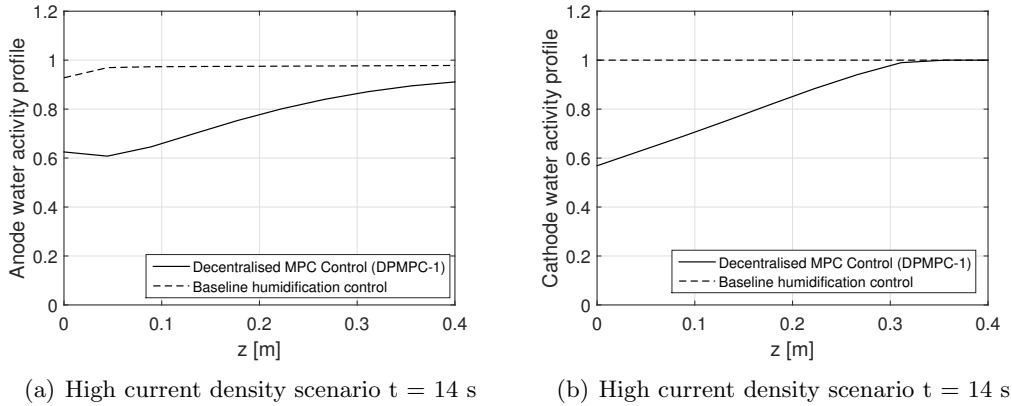(a) Low current density scenario t $= 9$ s   (b) Low current density scenario t $= 9$ s
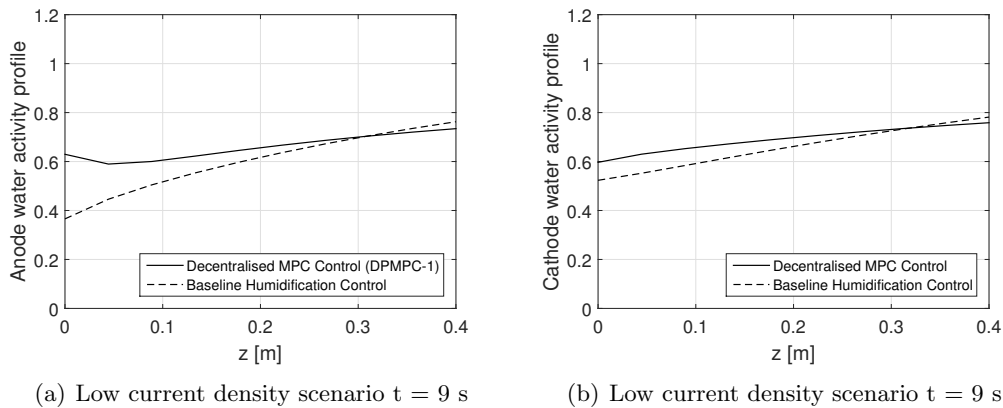
Figure 8.9: Steady-state results - Average water activity profiles - High current density scenario - DPMPC-1 vs. Baseline humidification control

Finally, Figures 8.10(a) and 8.10(b) show the membrane hydration levels for both high and low current densities scenarios (t $= 14$ s and t $= 9$ s respectively). It can be seen how the baseline humidification control approach keeps the membrane fully hydrated at high current density scenarios due the increased rate of liquid water production. However, during periods of low current densities, unless the fuel cell has been running at higher current densities to generate a certain amount of water, membrane behaviour towards dryness is observed.

Overall, the approach DPMPC-1 has low computational complexity, i.e. 30% CPU capacity in a 2.7 GHz Intel Core i5 processor, which allows for very fast simulation times. It is expected that this approach implemented in a device with high computational capabilities, such as a vehicle electronic control unit (ECU), will have very high performance.

8.6.2   Analysis of DPMPC-1 vs. DPMPC-2

In the previous section, water activity spatial profiles on both anode and cathode sides of the membrane were controlled to reduce the accumulation of liquid water on the catalyst and other backing layers (DPMPC-1). The hydrogen and oxygen stoichiometries were fixed

(a) Low current density scenario t = 9 s   (b) High current density scenario t = 14 s
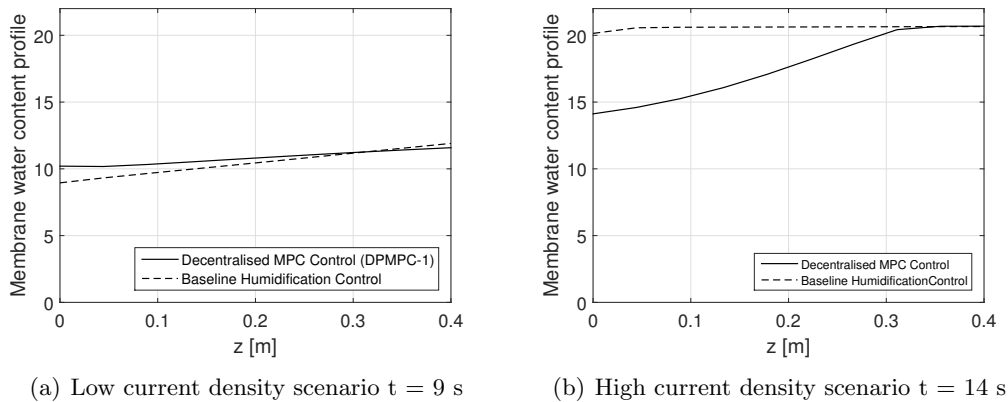
Figure 8.10: Steady-state results - Membrane water content profiles - DPMPC-1 vs. Baseline humidification control

to 1.5 and 3 respectively. This strategy was achieved by restricting the inlet H_2 and O_2 manipulated variables in each MPC to supply only this amount of reactants in proportion to current demanded. In this section, new spatial control targets are considered in order to exploit the benefits of decentralised distributed parameter control (DPMPC-2). The details of the design for this strategy are presented in Section 8.4.

Figure 8.11 shows steady-state results of the hydrogen and oxygen concentration profiles along the z-direction for DPMPC-1 vs. DPMPC-2 under the operating point $U = 0.55$ V. The results not only confirm the preventive effect of the control actions on the gas concentrations in the last segment of the channel, but also demonstrate the overall impact of the strategy along the concentration spatial profiles.

8.6.3   Analysis of DPMPC-1 vs. DPMPC-3

Changes in voltage and temperature are the most important external disturbances to the controlled PEM fuel cell under study. A test is designed to specifically assess the robustness of the proposed control strategies DPMPC-1 vs. DPMCP-3 under different temperature conditions. As seen in Section 8.5 there are two different types of reference models in these strategies. The strategy DPMPC-1 uses linear reference models with adaptive features, derived from a variation of the classic balance truncation technique. The strategy DPMPC-3 uses simpler anode and cathode linear reference models derived using traditional balanced truncation.

Figures 8.12, 8.13 and 8.14 show the results of the two versions of DPMPC under a temperature cycle (Figure 8.12(a)). Temperature is a key variable to demonstrate control robustness, as the linear reference models depend on a fix equilibrium point (70°C) when created (Section 8.3). However, DPMPC-1 considers the deviation of temperature from the original equilibrium point as a measured disturbance. DPMPC-3 does not hold this characteristic in order to make it a much faster controller. This advantage allows the
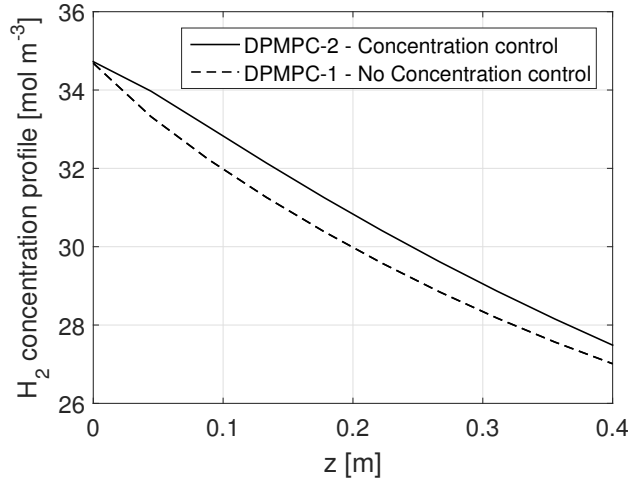
(a) Anode gas channel
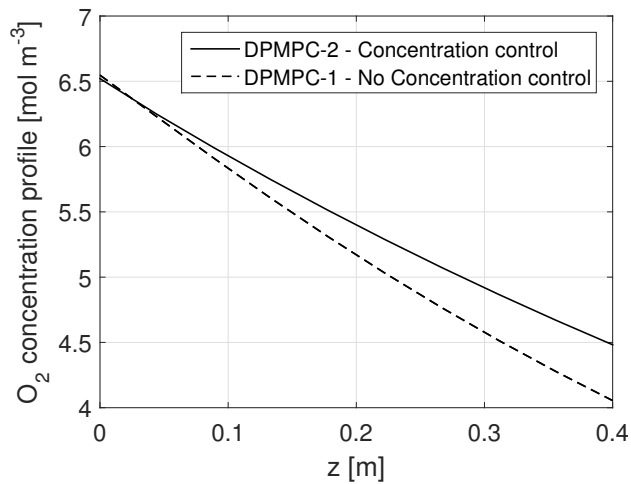
(b) Cathode gas channel

Figure 8.11: Steady-state results - High current scenario - Control of reactants concentration in the last segment along the z-direction

reference models in DPMPC-1 to remain accurate under different temperature conditions. Both DPMPC-1 and DPMPC-3 are quite robust against voltage variations. This figure clearly shows the better performance of DPMPC-1 for temperature fluctuations.

Temperature has a clear impact on pressure, affecting both current (Figure 8.12(b)) and the water activity profile. Model inaccuracies of DPMPC-3 are observed during this temperature cycle. The changes in pressure appreciated through temperature changes are not understood by the corresponding reference models in DPMPC-3. The control strategy is not able to achieve the average water activity target for both MPC controllers, although it manages to take actions to delay liquid water formation as much as possible (Figures 8.13(a) and 8.13(b)).

DPMPC-1 on the other hand is able to achieve the target in water activity during the

(a) Temperature cycle
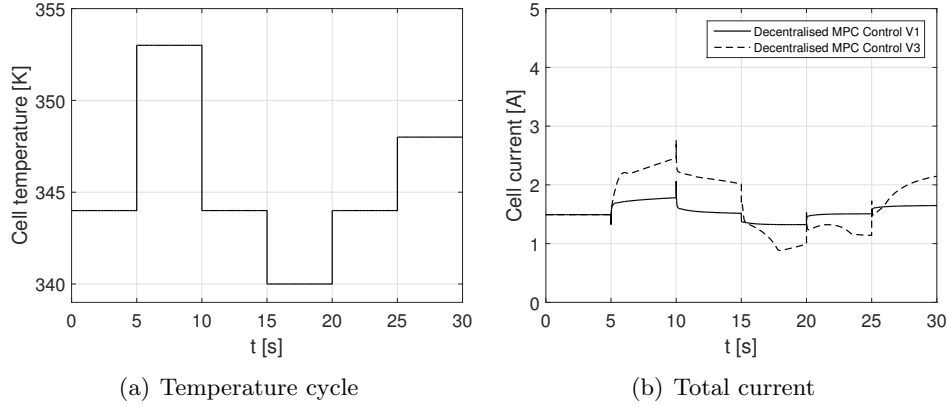
(b) Total current

Figure 8.12: Temperature cycle and total current - DPMPC-1 vs. DPMPC-3

(a) Anode $a_{H_2O,avrg}^A$ (controlled var.)

(b) Cathode $a_{H_2O,avrg}^C$ (controlled var.)
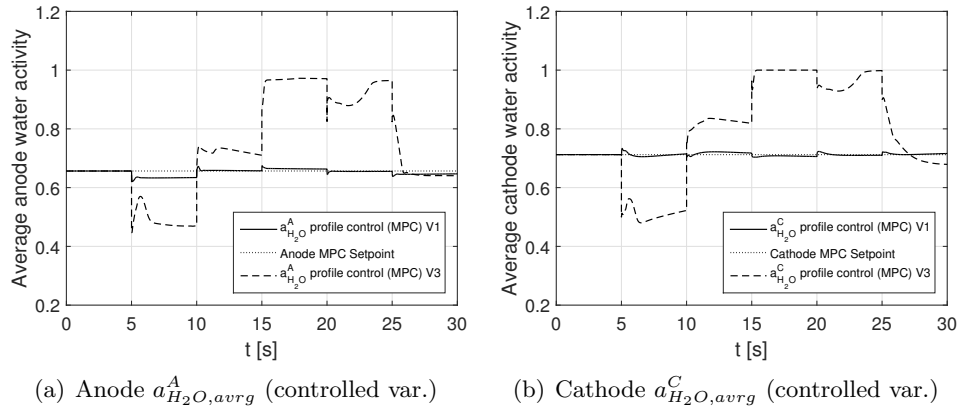
Figure 8.13: Manipulated variables with priority in the optimisation procedure - DPMPC-1 vs. DPMPC-3

simulation time except for 5 seconds where the temperature increases up to 80°C and there is a certain offset in the anode average water activity setpoint. In this case back diffusion is not enough to maintain the desired target and there should be higher control effort from the manipulated variables according to the temperature level. This is one of the most challenging scenarios for water management.

Notice that under extreme external operating conditions (ambient temperature, ambient relative humidity) or extreme duty cycles, inlet gas humidification control strategies, as well as thermal management strategies, might struggle to meet desired control setpoints. This situation will require the action of a master fuel cell system control in order to bring the different variables of the fuel cell back to acceptable operating conditions. The actions by the master system control could include: (i) changes in anode and cathode pressure levels, maintaining a trade-off between system efficiency and reliability to supply required power, (ii) redistribution of the load if other power sources, such as batteries, are available. This action could help to increase or decrease the temperature of the fuel cell. Under low ambient temperature conditions, increasing the load of the fuel cell, if possible, is a feasible strategy

to evaporate excess liquid water in the cell. However, this topic on master control falls outside the scope of this work and dedicated literature review is recommended.

DPMPC-3 causes major fluctuation levels in the concentrations of the gases affecting stability of the fuel cell. DPMCP-1 remains stable although fluctuations in current level due to changes in temperature are observed (Figure 8.12(b)). Steady-state results during increased temperature operating conditions (t = 9 s) and decreased temperature conditions (t = 19 s) are analysed in Figures 8.14(a) and 8.14(b).

(a) Membrane water content (high temp.)　　(b) Membrane water content (low temp.)
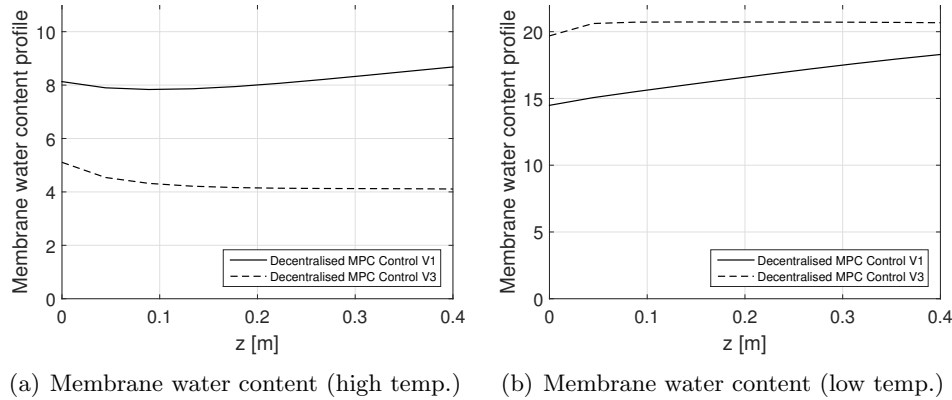
Figure 8.14: Steady-state results - Membrane water content profile - DPMPC-1 vs. DPMPC-3

The advantage of DPMPC-1 over DPMPC-3 is clear. Figure 8.14(a) indicates that DPMPC-3 is not able to cope with a positive deviation of temperature levels from the equilibrium point used in corresponding reference models design. Tendency to dryness in the membrane is noticed. The opposite situation occurs upon temperature decrease. Negative deviations from the equilibrium point result in excess liquid water formation keeping the membrane under high water content levels along the z-direction. In summary, the DPMPC-3 approach leads to faster simulations, however control robustness is compromised. DPMPC-1 is then used as the preferred version of the DPMPC strategy.

8.7　Conclusions

A novel decentralised distributed parameter model predictive control strategy has been designed, implemented and analysed in this work via simulation environment. The control targets focus on supplying the required humidified inlet gas flow whilst reducing the rate of accumulation of liquid water on the catalyst and other backing layers, as well as preventing local drying on the membrane or catalyst layers of the anode and cathode. Spatial control of the concentration of gases is also considered to avoid reactant starvation. The main features of this strategy are:

(1) The use of two separate model predictive controllers (MPC) based on order-reduced

models of the anode and cathode to maintain the water activity on both sides of the membrane at appropriate levels, in order to avoid local excess of liquid water or drying. This decentralised condition allows for simpler and faster controllers given the decreased complexity of the reference model in each controller.

(2) The use of distributed parameter models as reference models within the MPC controllers. This allows consideration of water activity and reactants concentration spatial profiles along the z-direction, which are the control targets of this work.

(3) The use of parameter-dependent order-reduced reference models. This allows for more accurate reference models that can adapt to disturbances, increasing the overall control strategy robustness whilst maintaining the simplicity of linear reference models.

(4) The use of observers to estimate the spatial profiles of the different variables of interest and feed these profiles to the MPC controllers. This task is very important for future experimental work since the inclusion of sensors to obtain spatial profiles measures would increase the complexity and cost of both the system and the controller. Currently, observer design techniques are quite attractive in the analysis of sensorless applications with cost reduction purposes.

Results show an important improvement in cell performance due to reduced liquid water formation rates. The MPC controllers manage to take advantage of the water transport processes within the PEM fuel cell, namely, water generation on the cathode side, electro-osmotic drag due to proton flux through the membrane and back diffusion caused by gradients in water concentration. This feature allows for efficient use of external humidification variables. In addition, proper setpoints chosen to control water activity levels on both anode and cathode catalyst layers result in appropriate membrane humidification levels. Overall, the strategy decreases the loss of performance due to liquid water coverage, as well as the chances for starvation of reactants. The key objective of this approach is to decrease the frequency of water removal actions that cause disruption in the power supplied by the cell, increased parasitic losses and reduction of cell efficiency.

Currently, other possibilities of water activity diagnosis in the fuel cell and different control techniques for the decentralised scheme, as well as a centralised variation, are active tasks in this framework. Future work also includes experimental testing of this concept in order to evolve the approach to higher technology readiness levels. The work in this chapter generated the following contribution:

Journal paper

- M.L. Sarmiento-Carnevali, M. Serra, C. Batlle, Decentralised distributed parameter model predictive control of water activity for performance and durability enhancement of a PEM fuel cell, submitted to the Journal of Power Sources, May 2017.

Part IV

Concluding Remarks

Chapter 9

Conclusions

This thesis focused on the modelling and control of PEM fuel cells. A distributed parameter model of a single-channel single PEM fuel cell was designed, implemented and validated in order to account for spatial variations of key cell performance variables. The model is nonlinear with 1+1D dimensions. The 1D dimension (z-direction) was discretised using finite differences.

Governing first principles and empirical equations for the processes that occur within the gas channels and the MEA were considered. Mass and energy balances for the gas channels and MEA were calculated. Well-known electrochemical equations were used to describe the consumption of reactants and generation of products as well as the cell current and voltage. Empirical equations were used to describe the water transport processes through the membrane.

The model was validated following a quantitative analysis using polarisation curves and a qualitative analysis of spatial profiles from different cell variables. The results show that the distributed parameter model gives a good representation of an experimental Pragma Industries single PEM fuel cell across a range of steady-state operating points.

A comprehensive analysis of PEM fuel cell challenges in water management and supply of reactants was performed using the developed distributed parameter model. Results demonstrated the importance of spatial variations of variables in the cell that affected performance and could lead to degradation mechanisms.

In the control part of the thesis, decentralised distributed parameter model predictive control schemes were designed to maintain the water activity on both anode and cathode sides of the PEM at appropriate levels. The proposed strategies tackle the accumulation of liquid water on the surface of the catalyst layers, and the possibility of local drying, by controlling observed water activity spatial profiles. Classic PEM fuel cell issues like reactant starvation were also considered.

The decentralised feature of the control schemes, combined with the use of order-reduced models within the model predictive controllers, has important impact on the overall control performance. The strategies were applied to the validated PEM fuel cell model. State

observers were also designed and implemented to estimate the internal states of the non-linear model from measures of its inputs and outputs.

Results show increased cell power density in comparison to non-spatial water control strategies. Liquid water formation rates were reduced. The MPC controllers manage to take advantage of the water transport processes within the PEM fuel cell, in order to properly humidify the catalyst layers. This feature allows for efficient use of external humidification variables.

In addition, proper setpoints chosen to control water activity levels on both anode and cathode catalyst layers result in appropriate membrane humidification levels. Overall, the proposed strategies diminish the loss of performance due to liquid water coverage, as well as the chances for starvation of reactants and the resulting cell degradation. Membrane dryness is also prevented. The key objective of these approaches is to decrease the frequency of water removal actions that cause disruption in the power supplied by the cell, increased parasitic losses and reduction of cell efficiency.

9.1   Thesis contributions and novel work

In summary, the main contributions to the PEM fuel cell field presented in this thesis are:

- Development and implementation of control-oriented non-linear PEM fuel cell distributed parameter models, suitable to both analyse spatial variations of important variables in the cell and design model-based controllers. State-of-the-art fuel cell technology challenges involve cell variables that present important spatial variations, which should be taken into account for problem understanding. Most degradation mechanisms in the different components of the PEM fuel cells have local impact. This thesis presented novel contributions to the PEM fuel cell literature regarding the development of distributed parameter control-oriented models, following simplification approaches with solid mathematic background like model order reduction techniques.

- Analysis of certain PEM fuel cell state-of-the-art technology challenges using PEM fuel cell distributed parameter models, focusing on improving the understanding of spatial profile variations of relevant variables and corresponding implications.

- Use of model order reduction techniques in order to simplify complex distributed parameter models, and allow for accurate reference models in distributed parameter model-based control strategies of PEM fuel cells. No works have been found in the literature with this purpose.

- Use of observers to estimate the spatial profiles of the different variables of interest and feed these profiles to the model-based controllers. This task is very important for future experimental work, since the inclusion of sensors to obtain spatial profiles

measures would increase the complexity and cost of both the system and the controller. Currently, observer design techniques are quite attractive in the analysis of sensorless applications with cost reduction purposes.

- Development and implementation of PEM fuel cell model predictive controllers and model-based control strategies, which target spatial profile behaviours desired to enhance the cell performance and consequently reduce degradation. The proposed strategies tackle the rate of accumulation of liquid water on the surface of the catalyst layers, and the possibility of local drying, by controlling observed water activity spatial profiles. Classic PEM fuel cell issues like reactants starvation are also considered. Moreover, certain features of the control scheme have important impact on the overall control performance due to the use of order-reduced models within the model predictive controllers. The proposed controllers are innovative solutions with respect to the controllers described in the literature.

9.2 Scope of opportunities for future work

The results presented in this thesis open a window of opportunities for improvement of the PEM fuel cell technology. First, future work could aim at improving the distributed parameter model. In reality, a fuel cell is not a stand-alone device, but part of a larger system that comprises the hydrogen supply subsystem, the air supply subsystem, the cooling subsystem and the humidification subsystem, storages for heat and electrical energy, as well as elements to condition the electrical power generated. The combination of these elements poses more challenges to PEM fuel cell control. Therefore, the modelling and control approaches proposed in this thesis are considered a first step in the direction of distributed parameter model-based control of PEM fuel cell systems.

In addition, various possibilities of water activity diagnosis in the fuel cell, such as online electrochemical impedance spectroscopy (EIS), could be explored and combined with the proposed decentralised control strategies. Furthermore, different control techniques for the decentralised scheme, namely sliding mode control, adaptive control or non-linear MPC control, could be implemented and analysed to assess computational complexity against control performance. An optimised centralised variation of the scheme could also be implemented to analyse integrated control actions.

The important aspect of these potential improved strategies is to keep the essence of the concepts presented in this thesis, which is the development of low computational complexity control strategies for PEM fuel cells, which consider spatial profiles of relevant variables. In this work, such objective was achieved by reducing the order of large-scale distributed parameter models, in order to make them suitable for a model predictive control strategy. Finally, future work also includes experimental testing of this concept in order to evolve the approach to higher technology readiness levels.

Appendices

Appendix A

Model parameters

Table A.1: Model parameters [13, 63] and Pragma Ind.

Symbol	Value
α_1	100 W m^{-2} K^{-1}
α_2	100 W m^{-2} K^{-1}
ΔG_0	7.3 x10^4 J mol^{-1}
δ^A	0.7x10^{-3} m
δ^{AC}	4x10^{-5} m
δ^C	0.7x10^{-3} m
δ^{GA}	0.34x10^{-3} m
δ^{GC}	0.34x10^{-3} m
δ^{CC}	1.1x10^{-4} m
δ^M	1.75x10^{-4} m
λ^A	0.1917 W m^{-1} K^{-1}
λ^C	0.2799 W m^{-1} K^{-1}
λ^S	0.43 W m^{-1} K^{-1}
C^A	8.25 x 10^6 F m^{-3}
C^C	8.25 x 10^6 F m^{-3}
$CCSA$	8.75.10^{-7} m^2
$D^{eff}_{H_2,H_2O}$	10^{-6} m^2 s
$D^{eff}_{O_2,H_2O}$	3 x 10^{-6} m^2 s
$D^{eff}_{O_2,N_2}$	2 x 10^{-6} m^2 s
$D^{eff}_{H_2O,N_2}$	2.5 x 10^{-6} m^2 s
$ECSA$	0.0005 m^2
f_v	60
i_{A0}	100 A m^{-2}
i_{C0}	0.187 x 10^{-3} A m^{-2}
K^A	10^{-5} m^2 s^{-1} Pa^{-1}
K^C	10^{-4} m^2 s^{-1} Pa^{-1}
L_x	0.00125 m
L_z	0.4 m
Pt loading An	0.3 mg cm^{-2}
Pt loading Ca	0.6 mg cm^{-2}
p^{amb}	101325 Pa

Appendix B

Model predictive control basics

The basic MPC concept can be summarised as follows. Suppose that it is necessary to control a multiple-input, multiple-output process whilst satisfying inequality constraints on the input and output variables. If a reasonably accurate dynamic model of the process is available, model and measurements at a given time can be used to predict future values of the outputs. The appropriate changes in the input variables can then be calculated based on both predictions and measurements.

In essence, the changes in the individual input variables are coordinated after considering the input-output relationships represented by the system model. In MPC applications, the output variables are also referred to as controlled variables or CVs, whilst the input variables are also called manipulated variables or MVs. Measured disturbance variables are called DVs or feedforward variables. The system model used by an MPC controller to make predictions is the so-called reference model.

Model predictive control offers several important advantages: (i) the system model captures the dynamic and static interactions between input, output, and disturbance variables, (ii) constraints on inputs and outputs are considered in a systematic manner, (ii) the control calculations can be coordinated with the calculation of optimum set points, and (iv) accurate model predictions can provide early warnings of potential problems. Clearly, the success of MPC (or any other model-based approach) depends on the accuracy of the reference model. Inaccurate predictions can lead to poor control actions that might endanger the integrity of the system and its environment.

B.1 Model predictive control approaches

First-generation MPC systems were developed independently in the 1970s by two pioneering industrial research groups. Dynamic Matrix Control (DMC), devised by Shell Oil, and a related approach developed by ADERSA have quite similar capabilities. An adaptive MPC technique called Generalised Predictive Control (GPC) has also received considerable attention. Model predictive control has had a major impact on industrial practice, particularly in

oil refineries and electrochemical plants. In these industries, MPC has become the method of choice for difficult multivariable control problems that include inequality constraints. In view of its remarkable success, MPC has been a popular subject for academic and industrial research. Major extensions of the early MPC methodology have been developed, and theoretical analysis has provided insight into the strengths and weaknesses of MPC. Informative reviews of MPC theory and practice are available in [19].

B.2   Overview of model predictive control

The overall objectives of an MPC controller are [79]:

1. To prevent violations of input and output constraints.

2. To drive some output variables to their optimal setpoints, whilst maintaining other outputs within specified ranges.

3. To prevent excessive movement of the input variables (oscillations).

4. To control as many process variables as possible.

A block diagram of a model predictive control system is shown in Figure B.1.
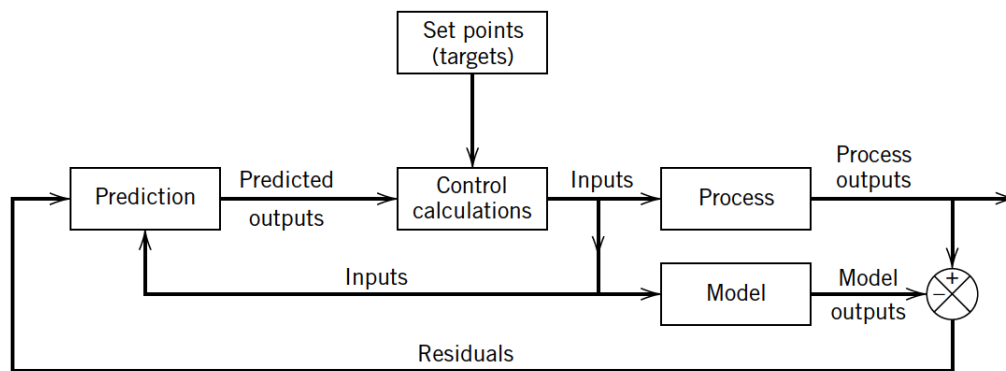
Figure B.1: Block diagram for model predictive control [19]

A reference model of the controlled process is used to predict the current values of the output variables. The residuals, the differences between the actual and predicted outputs, serve as the feedback signal to a Prediction block. The predictions are used in two types of MPC calculations that are performed at each sampling instant: setpoint calculations and control calculations. Inequality constraints on the input and output variables, such as upper and lower limits, can be included in either type of calculation. Note that the model acts in parallel with the process and the residual serves as a feedback signal. However, the coordination of the control and setpoint calculations is a unique feature of MPC. Furthermore, MPC is suitable for constrained Multi-input Multi-Output (MIMO) control problems.

The setpoints for the control calculations are target values of system variables. Within the Control calculations block, an on-line optimisation process occurs (as explained in Chapter 8). The MPC calculations are based on current measurements and predictions of the future values of the outputs. The objective of the MPC control calculations is to determine a sequence of control moves (that is, manipulated input changes) so that the predicted response moves to the setpoint in an optimal manner. The actual output y, predicted output and manipulated input u for SISO control are shown in Figure B.2.

At the current sampling instant, denoted by k in this appendix, the MPC strategy calculates a set of M values of the input $u(k+i-1), i = 1, 2, ..., M$. The set consists of the current input $u(k)$ and $M-1$ future inputs. The input is held constant after the M control moves. The inputs are calculated so that a set of P predicted outputs $y(k+i), i = 1, 2, ..., P$ reaches the setpoint in an optimal manner. The control calculations are based on optimising an objective function (Chapter 8). The number of predictions P is referred to as the prediction horizon whilst the number of control moves M is called the control horizon.
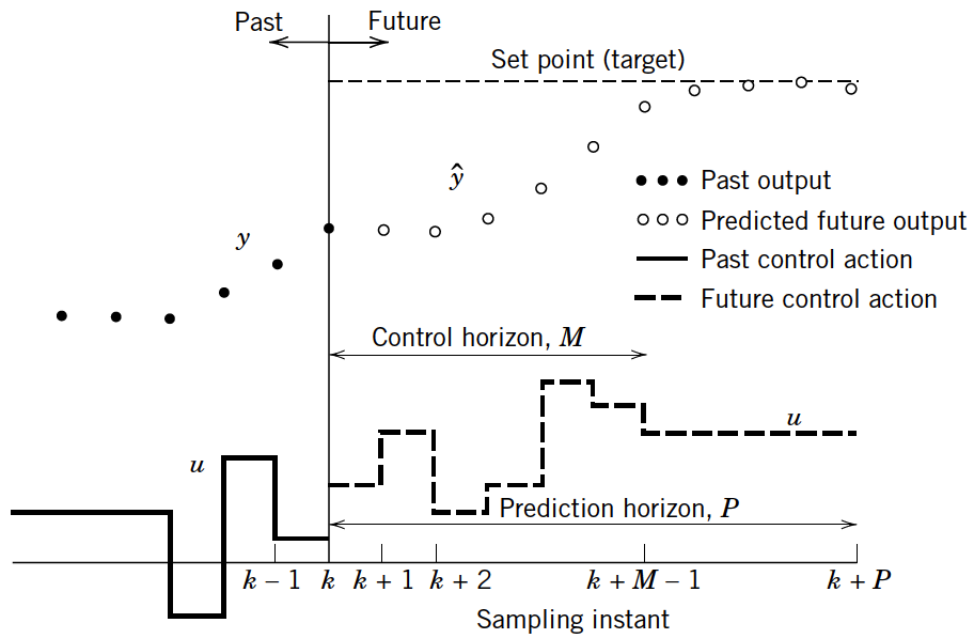
Figure B.2: Block diagram for model predictive control [79]

A distinguishing feature of MPC is its receding horizon approach. Although a sequence of M control moves is calculated at each sampling instant, only the first move is actually implemented. Then a new sequence is calculated at the next sampling instant, after new measurements become available; again only the first input move is implemented. This procedure is repeated at each sampling instant. For extended information on the MPC

approach refer to [19].

Appendix C

Additional results

This appendix presents the list of matrices used in the simulations for the DPMPC-1, DPMPC-2 and DPMPC-3 approaches, including reference models and observers. The implementation of the control schemes is different since both the MPC and NMPC MATLAB functions were used. The function NMPC was only considered due to its flexibility to allow symbolic parameters in the reference models. This feature was quite convenient in the implementation of DPMPC-1. Due to space limitations, reference to electronic files containing data of the matrices are indicated. If required, these files can be obtained by contacting the author of the thesis work (msarmiento@iri.upc.edu, marialaurasc@gmail.com).

C.1   Matrices of the DPMPC-1 approach

In the following sections, matrices of corresponding reference models and observers are presented. Dred is the zero matrix.
<u>Anode reference model</u>

Ared (m=10°C)
    See file RefModAnodeADPMPC1.csv
Bred (m=10°C)
    See file RefModAnodeBDPMPC1.csv
Cred (m=10°C)
    See file RefModAnodeCDPMPC1.csv

<u>Cathode reference model</u>

Ared (m=10°C)
    See file RefModCathodeADPMPC1.csv
Bred (m=10°C)
    See file RefModCathodeBDPMPC1.csv
Cred (m=10°C)

See file RefModCathodeCDPMPC1.csv

Anode observer

$\hat{A}$

See file ObsAnodeAhatDPMPC.csv

$\hat{B}$

See file ObsAnodeBhatDPMPC.csv

$\hat{C}$

See file ObsAnodeChatDPMPC.csv

Cathode observer

$\hat{A}$

See file ObsCathodeAhatDPMPC.csv

$\hat{B}$

See file ObsCathodeBhatDPMPC.csv

$\hat{C}$

See file ObsCathodeChatDPMPC.csv

C.2 Matrices of the DPMPC-2 approach

In the following sections, matrices of corresponding reference models are presented. Observer matrices are the same used in DPMPC-1. Dred is the zero matrix.

Anode reference model

Ared (m=10°C)

See file RefModAnodeADPMPC2.csv

Bred (m=10°C)

See file RefModAnodeBDPMPC2.csv

Cred (m=10°C)

See file RefModAnodeCDPMPC2.csv

Cathode reference model

Ared (m=10°C)

See file RefModCathodeADPMPC2.csv

Bred (m=10°C)

See file RefModCathodeBDPMPC2.csv

Cred (m=10°C)

See file RefModCathodeCDPMPC2.csv

C.3   Matrices of the DPMPC-3 approach

In the following sections, matrices of corresponding reference models are presented. Observer matrices are the same used in DPMPC-1. Dred is the zero matrix.

<u>Anode reference model</u>

Ared
    See file RefModAnodeADPMPC3.csv
Bred
    See file RefModAnodeBDPMPC3.csv
Cred
    See file RefModAnodeCDPMPC3.csv

<u>Cathode reference model</u>

Ared
    See file RefModCathodeADPMPC3.csv
Bred
    See file RefModCathodeBDPMPC3.csv
Cred
    See file RefModCathodeCDPMPC3.csv

C.4   Closed-loop diagram implementation

A version of the closed-loop system implementation (DPMPC-2) is presented in Figure C.1.

Figure C.1: Decentralised distributed parameter model predictive control MATLAB scheme

Bibliography

[1] International Energy Agency. *Prospects for hydrogen and fuel cells. Energy Technology Analysis.* 2005.

[2] International Energy Agency. *Energy Technology Essentials - Fuel Cells.* 2007.

[3] International Energy Agency. *Energy Technology Perspectives.* 2016.

[4] International Energy Agency. *Key World Energy Statistics 2016.* 2016.

[5] International Energy Agency. *Medium-Term Coal Market Report.* 2016.

[6] International Energy Agency. *World Energy Outlook 2016.* 2016.

[7] J.W. Ahn and S.Y. Choe. Coolant controls of a PEM fuel cell system. *Journal of Power Sources*, 179(1):252 – 264, 2008.

[8] A.C. Antoulas. Lectures on the approximation of large-scale dynamical systems. In *SIAM Press*, 2002.

[9] A.J. Appleby and S. Gamburzev. Electroconductive fuel cell component with directly bonded layers and method for making same, August 16 2001. WO Patent App. PCT/US2001/004,485.

[10] R. Baker and J. Zhang. Proton exchange membrane PEM fuel cells - electrochemistry encyclopedia, 2011.

[11] B. Balasubramanian, F. Barbir, and J. Neutzler. Optimal operating temperature and pressure of PEM fuel cell systems in automotive applications. *Energy Partners, L.C. New Orleans*, (Paper 0977).

[12] C. Bao, M. Ouyang, and B. Yi. Modeling and control of air stream and hydrogen flow with recirculation in a PEM fuel cell system—i. control-oriented modeling. *International Journal of Hydrogen Energy*, 31(13):1879–1896, 2006.

[13] Frano Barbir. *PEM Fuel Cells: Theory and Practice.* Academic Press, 2005.

[14] C. Batlle and N. Roqueiro. Balanced model order reduction for systems depending on a parameter. *CoRR*, abs/1604.08086:1–14, 2016.

[15] P. Benner, S. Gugercin, and K. Willcox. A survey of projection-based model reduction methods for parametric dynamical systems. *SIAM Review*, 57(4):483–531, 2015.

[16] P. Berg, K. Promislow, J. St. Pierre, J. Stumper, and B. Wetton. Water management in PEM fuel cells. *Journal of The Electrochemical Society*, 151(3):A341–A353, 2004.

[17] D.M. Bernardi and M.W. Verbrugge. Mathematical model of a gas diffusion electrode bonded to polymer electrolyte. *AIChE*, 37(8), 1991.

[18] A.D.P. Bosco and M.H. Fronk. Fuel cell flooding detection and correction, August 15 2000. US Patent 6,103,409.

[19] E.F. Camacho and C. Bordons. *Model Predictive Control*. Springer, 2012.

[20] Andrew Hamnett Carl H Hammann and Wolf Vielstich. *Electrochemestry*. Wiley-VCH, 2007.

[21] M. Casciola, G. Alberti, M. Sganappa, and R. Narducci. On the decay of nafion proton conductivity at high temperature and relative humidity. *Journal of Power Sources*, 162(1):141 – 145, 2006.

[22] M. Ciureanu. Effects of nafion dehydration in pem fuel cells. *Journal of Applied Electrochemistry*, 34(7):705–714, 2004.

[23] S. Cruz-Manzo, R. Chen, and P. Rama. Study of current distribution and oxygen diffusion in the fuel cell cathode catalyst layer through electrochemical impedance spectroscopy. *International Journal of Hydrogen Energy*, 38(3):1702 – 1713, 2013.

[24] F.A. de Bruijn, V.A.T. Dam, and G.J.M. Janssen. Review: Durability and degradation issues of PEM fuel cell components. *Fuel Cells*, 8:3 – 22, 2008.

[25] S. de Lira, V. Puig, J. Quevedo, and A. Husar. LPV observer design for PEM fuel cell system: Application to fault detection. *Journal of Power Sources*, 196(9):4298 – 4305, 2011.

[26] S. Dutta, S. Shimpalee, and J.W. Van Zee. Three-dimensional numerical simulation of straight channel pem fuel cells. *Journal of Applied Electrochemistry*, 30(2):135–146, 2000.

[27] A.G. Ivanova et al. Structure and proton conductivity of a hydrated nafion-115 membrane. *Glass Physics and Chemistry*, 42(6):637–639, 2016.

[28] B. Wu et al. The degradation study of nafion/ptfe composite membrane in PEM fuel cell under accelerated stress tests. *International Journal of Hydrogen Energy*, 39(26):14381 – 14390, 2014.

[29] F.I. Sempurna et al. Effect of start-stop cycles and hydrogen temperature on the performance of proton exchange membrane fuel cell (PEMFC). In *2014 International Conference on Electrical Engineering and Computer Science (ICEECS)*, pages 27–29, Nov 2014.

[30] G. Karimi et al. Along-channel flooding prediction of polymer electrolyte membrane fuel cells. *International Journal of Energy Research*, 35(10):883–896, 2011.

[31] H. Li et al. A review of water flooding issues in the proton exchange membrane fuel cell. *Journal of Power Sources*, 178(1):103 – 117, 2008.

[32] J. St-Pierre et al. PEM fuel cells. In *Proceedings of the Second International Symposium on New Materials for Fuel Cell and Modern Battery Systems*, 1997.

[33] L. Sung et al. The influence of air-bleeding on co-poisoning of pem fuel cell. In *ASME International Conference on Fuel Cell Science, Engineering and Technology*, 2004.

[34] R. Borup et al. Scientific aspects of polymer electrolyte fuel cell durability and degradation. *CHEMICAL REVIEWS*, 107(10):3904–3951, Oct 2007.

[35] R. Halseid et al. Effect of ammonia on the performance of polymer electrolyte membrane fuel cells. *Journal of Power Sources*, 154:343–350, 2006.

[36] V. Gurau et al. Two-dimensional model for proton exchange membrane fuel cells. *AIChE Journal*, 44(11):2410– 2422, 1998.

[37] D. Feroldi, M. Serra, and J. Riera. Performance improvement of a PEMFC system controlling the cathode outlet air flow. *Journal of Power Sources*, 169(1):205 – 212, 2007.

[38] N.J. Fletcher, C.Y. Chow, E.G. Pow, B.M. Wozniczka, H.H. Voss, and G. Hornburg. Electrochemical fuel cell stack with concurrently flowing coolant and oxidant streams, August 20 1996. US Patent 5,547,776.

[39] A. Fly. *Thermal and water management of evaporatively cooled fuel cell vehicles*. PhD thesis, Loughborough University, UK, 2015.

[40] T.J.P. Freire and E.R. Gonzalez. Effect of membrane characteristics and humidification conditions on the impedance response of polymer electrolyte fuel cells. *Journal of Electroanalytical Chemistry*, 503(1?2):57 – 68, 2001.

[41] K. Fujimoto and D. Tsubakino. Computation of nonlinear balanced realization and model reduction based on taylor series expansion. *Systems & Control Letters*, 57(4):283–289, 2008.

[42] P. Futerko and I. Hsing. Two-dimensional finite-element method study of the resistance of membranes in polymer electrolyte fuel cells. *Electrochimica Acta*, 45(11):1741 – 1751, 2000.

[43] S. Ge and C. Wang. Cyclic voltammetry study of ice formation in the pefc catalyst layer during cold start. 154(12):B1399–B1406, 2007.

[44] R.B. Gupta. *Hydrogen Fuel Production, Transport and Storage*. CRC Press, 2008.

[45] W. He, G. Lin, and T. Van Nguyen. Diagnostic tool to detect electrode flooding in proton-exchange-membrane fuel cells. *AIChE Journal*, 49(12).

[46] O.E. Herrera, D.P. Wilkinson, and W. Mérida. Anode and cathode overpotentials and temperature profiles in a PEMFC. *Journal of Power Sources*, 198:132 – 142, 2012.

[47] European Hydrogen and Fuel Cell Technology Platform. *Research Overview*. 2016.

[48] Iberdrola. *Innovation Report*. 2010.

[49] H. Donald Brooke Jenkins. *Chemical Thermodynamics at a Glance*. Blackwell Publishing, 2008.

[50] J.W., X.Z. Yuan, J.J. Martin, H. Wang, J. Zhang, J. Shen, S. Wu, and W. Merida. A review of PEM fuel cell durability: Degradation mechanisms and mitigation strategies. *Journal of Power Sources*, 184(1):104–119, 2008.

[51] I.H. Kazmi, A.I. Bhatti, and S. Iqbal. A nonlinear observer for pem fuel cell system. *Multitopic Conference, 2009. INMIC 2009. IEEE 13th International*, pages 1–6, 2009.

[52] Y.B. Kim. Study on the effect of humidity and stoichiometry on the water saturation of pem fuel cells. *International Journal of Energy Research*, 36(4):509–522, 2012.

[53] M.W. Knobbe, W. He, P.Y. Chong, and T.V. Nguyen. Active gas management for PEM fuel cell stacks. *Journal of Power Sources*, 138(1?2):94 – 100, 2004.

[54] P. Koski, L.C. Pérez, and J. Ihonen. Comparing anode gas recirculation with hydrogen purge and bleed in a novel PEMFC laboratory test cell configuration. *Fuel Cells*, 15(3):494–504, 2015.

[55] M. Krasij and P.R. Watson. Proton exchange membrane fuel cell support plate and an assembly including the same, 1993.

[56] Pijush K. Kundu and Ira M. Cohen. *Fluid Mechanics*. Academic Press, 1990.

[57] J. Larminie and A. Dicks. *Fuel Cell Systems Explained*. J. Wiley, 2003.

[58] J. Le Canut, R. M. Abouatallah, and D. A. Harrington. Detection of membrane drying, fuel cell flooding, and anode catalyst poisoning on pemfc stacks by electrochemical impedance spectroscopy. 153(5):A857–A864, 2006.

[59] G. Li and P. G. Pickup. Ionic conductivity of pemfc electrodes: Effect of nafion loading. 150(11):C745–C752, 2003.

[60] S. Litster and G. McLean. PEM fuel cell electrodes. *Journal of Power Sources*, 130(1?2):61 – 76, 2004.

[61] J. Liu, W. Lin, F. Alsaadi, and T. Hayat. Nonlinear observer design for PEM fuel cell power systems via second order sliding mode technique. *Neurocomputing*, 168:145 – 151, 2015.

[62] D.J. Ludlow, C.M. Calebrese, S.H. Yu, C.S. Dannehy, D.L. Jacobson, D.S. Hussey, M. Arif, M.K. Jensen, and G.A. Eisman. PEM fuel cell membrane hydration measurement by neutron imaging. *Journal of Power Sources*, 162(1):271 – 278, 2006.

[63] M Mangold, A Bück, and R Hanke-Rauschenbach. Passivity based control of a distributed pem fuel cell model. *Journal of Process Control*, 20(3):292–313, 2010.

[64] T.J. Mason, J. Millichamp, T.P. Neville, P.R. Shearing, S. Simons, and D.J.L. Brett. A study of the effect of water management and electrode flooding on the dimensional change of polymer electrolyte fuel cells. *Journal of Power Sources*, 242:70 – 77, 2013.

[65] D.A. McKay, W.T. Ott, and A.G. Stefanopoulou. Modeling, parameter identification, and validation of reactant and water dynamics for a fuel cell stack. In *Proceedings of 2005 ASME International Mechanical Engineering Congress & Exposition*, volume 2005, pages 1177–1186. ASME, Nov 2005.

[66] R.N. Methekar, V. Prasad, and R.D. Gudi. Dynamic analysis and linear control strategies for proton exchange membrane fuel cell using a distributed parameter model. *Journal of Power Sources*, 165(1):152–170, 2007.

[67] F. Migliardini, T.M. Di Palma, M.F. Gaele, and P. Corbo. Hydrogen purge and reactant feeding strategies in self-humidified PEM fuel cell systems. *International Journal of Hydrogen Energy*, 42(3):1758 – 1765, 2017.

[68] B. Moore. Principal component analysis in linear systems: Controllability, observability, and model reduction. *Automatic Control, IEEE Transactions on*, 26(1):17–32, 1981.

[69] M. H. Nehrir and C. Wang. *Modeling and Control of Fuel Cells: Distributed Generation Applications*. Wiley-IEEE Press, 2009.

[70] T.V. Nguyen and M.W. Knobbe. A liquid water management strategy for {PEM} fuel cell stacks. *Journal of Power Sources*, 114(1):70 – 79, 2003.

[71] U.S. Department of Energy. Hydrogen Data Book, 2017. Accessed on March 17th, 2017.

[72] K. Ogata. *Modern Control Engineering*. Pearson, 2005.

[73] Inc. Science Applications International Corporation Parsons. *Fuel Cell Handbook*. U.S. Department of Energy, 2000.

[74] U. Pasaogullari and C. Wang. Two-phase modeling and flooding prediction of polymer electrolyte fuel cells. *Journal of The Electrochemical Society*, 152(2):A380–A390, 2005.

[75] Intelligent Energy Holdings plc. *Intelligent Energy has signed a stationary power deal with US-based Luxfer-GTM Technologies as part of a growing strategic relationship in the development of a line of integrated fuel cell products.* 2017.

[76] K. Promislow and B. Wetton. Pem fuel cells: a mathematical overview. *SIAM J. Appl. Math*, 70(2):369–409, 2009.

[77] J.T. Pukrushpan, H. Peng, and A.G. Stefanopoulou. Control-oriented modeling and analysis for automotive fuel cell systems. *Journal of Dynamic Systems, Measurement, and Control*, 126:14, 2004.

[78] J.T. Pukrushpan, A.G. Stefanopoulou, and H. Peng. Modeling and control for PEM fuel cell stack system. In *Proceedings of the American Control Conference*, volume 4, pages 3117–3122, 2002.

[79] S.J. Qin and T.A. Badgwell. A survey of industrial model predictive control technology. *Control Engineering Practice*, 11(7):733 – 764, 2003.

[80] P. Rama, R. Chen, and J. Andrews. A review of performance degradation and failure modes for hydrogen-fuelled polymer electrolyte fuel cells. *Proceedings of the Institution of Mechanical Engineers, Part A: Journal of Power and Energy*, 222(5):421 – 441, 2008.

[81] A. Rowe and X. Li. Mathematical modeling of proton exchange membrane fuel cells. *Journal of Power Sources*, 102(1):82–96, 2001.

[82] R. Satija, D.L. Jacobson, M. Arif, and S.A. Werner. In situ neutron imaging technique for evaluation of water management systems in operating PEM fuel cells. *Journal of Power Sources*, 129(2):238 – 245, 2004.

[83] J.M.A. Scherpen. Balancing for nonlinear systems. *Systems & Control Letters*, 21:143–153, 1993.

[84] W. Schmittinger and A. Vahidi. A review of the main parameters influencing long-term performance and durability of PEM fuel cells. *Journal of Power Sources*, 180(1):1 – 14, 2008.

[85] J.M. Sergi and S.G. Kandlikar. Quantification and characterization of water coverage in pemfc gas channels using simultaneous anode and cathode visualization and image processing. *International Journal of Hydrogen Energy*, 36(19):12381–12392, 2011.

[86] Y. Shao, G. Yin, and Y. Gao. Understanding and approaches for the durability issues of pt-based catalysts for PEM fuel cell. *Journal of Power Sources*, 171(2):558 – 566, 2007.

[87] C Siegel. Review of computational heat and mass transfer modeling in polymer-electrolyte-membrane (pem) fuel cells. *Energy*, 33(9):1331–1352, 2008.

[88] J. Sjöberg. *Optimal control and model reduction of nonlinear DAE models*. PhD thesis, Linköping University, Sweden, 2008.

[89] Y. Sone, P. Ekdunge, and D. Simonsson. Proton conductivity of nafion 117 as measured by a four?electrode ac impedance method. 143(4):1254–1259, 1996.

[90] C. Spiegel. *PEM Fuel Cell Modeling and Simulation Using Matlab*. Academic Press, 2011.

[91] T.E. Springer, T.A. Zawodzinski, and S. Gottesfeld. Polymer electrolyte fuel cell model. 138(8):2334–2342, 1991.

[92] A. Su, F. Weng, C. Hsu, and Y. Chen. Studies on flooding in PEM fuel cell cathode channels. *International Journal of Hydrogen Energy*, 31(8):1031 – 1039, 2006. Fuel CellsFuel Cells.

[93] K.W. Suh and A.G Stefanopoulou. Coordination of converter and fuel cell controllers. *Intelligent Control, 2005. Proceedings of the 2005 IEEE International Symposium on, Mediterrean Conference on Control and Automation DOI - 10.1109/.2005.1467076*, pages 563–568, 2005.

[94] W.Q. Tao, C.H. Min, X.L. Liu, Y.L. He, B.H. Yin, and W. Jiang. Parameter sensitivity examination and discussion of PEM fuel cell simulation model validation: Part i. current status of modeling research and model development. *Journal of Power Sources*, 160(1):359–373, 2006.

[95] C.E. Thomas. Fuel cell and battery electric vehicles compared. *International Journal of Hydrogen Energy*, 34(15):6005 – 6020, 2009.

[96] Vauxhall, United Kingdom. WLTP driving cycle, 2017.

[97] A.P. Vega-Leal, F. Rogelio-Palomo, F. Barragán, C. García, and J.J. Brey. Design of control systems for portable PEM fuel cells. *Journal of Power Sources*, 169(1):194 – 197, 2007.

[98] E. Verriest. Time variant balancing and nonlinear balanced realizations. In Wilhelmus H. A. Schilders, Henk A. van der Vorst, and Joost Rommes, editors, *Model order reduction. Theory, research aspects and applications*. Springer, 2008.

[99] H.H. Voss, D.P. Wilkinson, P.G. Pickup, M.C. Johnson, and V. Basura. Anode water removal: A water management and diagnostic technique for solid polymer fuel cells. *Electrochimica Acta*, 40(3):321 – 328, 1995.

[100] C. Wang, H. Nehrir, and H. Gao. Control of PEM fuel cell distributed generation systems. In *2006 IEEE Power Engineering Society General Meeting*, pages 1 pp.–, 2006.

[101] Z.H. Wang, C.Y. Wang, and K.S. Chen. Two-phase flow and transport in the air cathode of proton exchange membrane fuel cells. *Journal of Power Sources*, 94(1):40 – 50, 2001.

[102] Z.H. Wang, C.Y. Wang, and K.S. Chen. Two-phase flow and transport in the air cathode of proton exchange membrane fuel cells. *Journal of Power Sources*, 94(1):40– 50, 2001.

[103] J. Wee, K. Lee, and S. Kim. Fabrication methods for low-pt-loading electrocatalysts in proton exchange membrane fuel cell systems. *Journal of Power Sources*, 165(2):667 – 677, 2007.

[104] C.H. Woo and J.B. Benziger. PEM fuel cell current regulation by fuel feed control. *Chemical Engineering Science*, 62(4):957 – 968, 2007.

[105] M. Wöhr. *Instationäres, thermodynamisches Verhalten der Polymermembra-Brennstoffzelle*. VDI-Verlag, 1999.

[106] C. Xu and T.S. Zhao. A new flow field design for polymer electrolyte-based fuel cells. *Electrochemistry Communications*, 9(3):497 – 503, 2007.

[107] X. Xue, J. Tang, A. Smirnova, R. England, and N. Sammes. System level lumped-parameter dynamic modeling of pem fuel cell. *Journal of Power Sources*, 133(2):188– 204, 2004.

[108] K.Z. Yao, K. Karan, K.B. McAuley, P. Oosthuizen, B. Peppley, and T. Xie. A review of mathematical models for hydrogen and direct methanol polymer electrolyte membrane fuel cells. *Fuel Cells*, 4(1-2):3–29, 2004.

[109] N. Yousfi-Steiner, Ph. Mocoteguy, D. Candusso, and D. Hissel. A review on polymer electrolyte membrane fuel cell catalyst degradation and starvation issues: Causes, consequences and diagnostic for mitigation. *Journal of Power Sources*, 194(1):130 – 145, 2009. 11th Polish Conference on Fast Ionic Conductors 2008.

[110] X. Riny Yuan, C. Song, H. Wang, and J. Zhang. *Electrochemical Impedance Spectroscopy in PEM Fuel Cells*. Springer-Verlag London, 2010.

[111] T.A. Zawodzinski, C. Derouin, S. Radzinski, R.J. Sherman, V.T. Smith, T.E. Springer, and S. Gottesfeld. Water uptake by and transport through nafion® 117 membranes. 140(4):1041–1047, 1993.

[112] F. Zenith and S. Skogestad. Control of fuel cell power output. *Journal of Process Control*, 17(4):333 – 347, 2007.

[113] S. Zhang, X. Yuan, H. Wang, W. Mérida, H. Zhu, J. Shen, S. Wu, and J. Zhang. A review of accelerated stress tests of MEA durability in PEM fuel cells. *International Journal of Hydrogen Energy*, 34(1):388 – 404, 2009.

[114] S. Zhang, X.Z. Yuan, J.N.C. Hin, H. Wang, K.A. Friedrich, and M. Schulze. A review of platinum-based catalyst layer degradation in proton exchange membrane fuel cells. *Journal of Power Sources*, 194(2):588 – 600, 2009.